U.S. DEPARTMENT OF ENERGY

PNNL-19736

Prepared for the U.S. Department of Energy
under Contract DE-AC05-76RL01830

Integrated Disposal Facility FY2010 Glass Testing Summary Report

EM Pierce
DH Bacon
SN Kerisit
CF Windisch
KJ Cantrell
MM Valenta
SD Burton
RJ Serne
SV Mattigod

September 2010

Pacific Northwest
NATIONAL LABORATORY

Proudly Operated by Battelle Since 1965

DISCLAIMER

PACIFIC NORTHWEST NATIONAL LABORATORY
operated by
BATTELLE
for the
UNITED STATES DEPARTMENT OF ENERGY
under Contract DE-AC05-76RL01830

Printed in the United States of America

Available to DOE and DOE contractors from the
Office of Scientific and Technical Information,
P.O. Box 62, Oak Ridge, TN 37831-0062;
ph: (865) 576-8401
fax: (865) 576-5728
email: reports@adonis.osti.gov

Available to the public from the National Technical Information Service,
U.S. Department of Commerce, 5285 Port Royal Rd., Springfield, VA 22161
ph: (800) 553-6847
fax: (703) 605-6900
email: orders@ntis.fedworld.gov
online ordering: http://www.ntis.gov/ordering.htm

This document was printed on recycled paper.
(9/2003)

PNNL-19736

Integrated Disposal Facility Glass Testing FY2010 Summary Report

EM Pierce
DH Bacon
SN Kerisit
CF Windisch
KJ Cantrell
MM Valenta
SD Burton
RJ Serne
SV Mattigod

September 2010

Prepared for
the U.S. Department of Energy
under Contract DE-AC05-76RL01830

Pacific Northwest National Laboratory
Richland, Washington 99352

Executive Summary

Pacific Northwest National Laboratory was contracted by Washington River Protection *Solutions*, LLC to provide the technical basis for estimating radionuclide release from the engineered portion of the disposal facility (e.g., source term). Vitrifying the low-activity waste at Hanford is expected to generate over 1.6×10^5 m^3 of glass (Puigh 1999). The volume of immobilized low-activity waste (ILAW) at Hanford is the largest in the DOE complex and is one of the largest inventories (approximately 0.89×10^{18} Bq total activity) of long-lived radionuclides, principally ^{99}Tc ($t_{1/2} = 2.1 \times 10^5$), planned for disposal in a low-level waste (LLW) facility. Before the ILAW can be disposed, DOE must conduct a performance assessement (PA) for the Integrated Disposal Facility (IDF) that describes the long-term impacts of the disposal facility on public health and environmental resources. As part of the ILAW glass testing program PNNL is implementing a strategy, consisting of experimentation and modeling, in order to provide the technical basis for estimating radionuclide release from the glass waste form in support of future IDF PAs. The purpose of this report is to summarize the progress made in fiscal year (FY) 2010 toward implementing the strategy with the goal of developing an understanding of the long-term corrosion behavior of low-activity waste glasses.

The emphasis in FY2010 was the completing an evaluation of the most sensitive kinetic rate law parameters used to predict glass weathering, documented in Bacon and Pierce (2010), and transitioning from the use of the Subsurface Transport Over Reactive Multi-phases to Subsurface Transport Over Multiple Phases computer code for near-field calculations. The FY2010 activities also consisted of developing a Monte Carlo and Geochemical Modeling framework that links glass composition to alteration phase formation by 1) determining the structure of unreacted and reacted glasses for use as input information into Monte Carlo calculations, 2) compiling the solution data and alteration phases identified from accelerated weathering tests conducted with ILAW glass by PNNL and Viteous State Laboratory/Catholic University of America as well as other literature sources for use in geochemical modeling calculations, and 3) conducting several initial calculations on glasses that contain the four major components of ILAW-Al_2O_3, B_2O_3, Na_2O, and SiO_2.

Acronyms and Abbreviations

1-D	one-dimensional
2-D	two-dimensional
ANSI	American National Standards Institute
AREST-CT	Analyzer for RadionuclidE Source-Term with Chemical Transport (AREST-CT)
BBO	Beta Barium Borate
DIW	deionized water
DOE	U.S. Department of Energy
EDS	energy dispersive spectroscopy
EM	Office of Environmental Management (DOE)
HDI	"How do I…?" (PNNL's standards based management system)
HLW	high-level waste
HR	high resolution
IDF	Integrated Disposal Facility
ILAW	immobilized low-activity waste
JY	Jobin Yvon
LabRAM	Laboratory Raman System
LAW	low-activity waste
LLW	low-level waste
MAS-NMR	magic-angle spinning nuclear magnetic resonance
MC	Monte Carlo
NBO	non-bridging oxygen
NQA	nuclear quality assurance
ORP	Office of River Protection
PA	performance assessment
PCT	Product Consistency Test
PNNL	Pacific Northwest National Laboratory
$Pt_{10}Rh_{90}$	10% platinum-90% rhodium crucible
PUF	Pressurized Unsaturated Flow Test
Q^n	SiO_4 tetrahedra with *n* non-bridging oxygen sites
QA	quality assurance
QC	quality control
RH	relative humidity
SEM	scanning electron microscopy
SGH	
SiO_4	structural representation of the silicate tetrahedral in the glass
SPFT	single-pass flow-through

STOMP	Subsurface Transport Over Multiple Phases
STORM	Subsurface Transport Over Reactive Multiphases (computer code)
S/V	solution-to-volume ratio
TEM	transmission electron microscopy
TST	transition state theory
UV	Ultra Violet
UK	United Kingdom
VHT	Vapor Hydration Test
WTP	Hanford Tank Waste Treatment and Immobilization Plant
XRD	X-ray diffraction

Units of Measure

°C	temperature in degrees Celsius [T(°C) = T(K) – 273.15]
cm	centimeter
g	gram
µ	micro (prefix, 10^{-6})
µm	micrometer
mW	milliwatt
m	meter
M	molarity, mole/Liter
mL	milliliter
mol	mole
nm	nanometers
s	second
R^2	r-squared – statistical measure of how well a data fit analysis approximates actual data points
wt%	weight percent

Contents

Figures

Tables

1.0 Introduction

The federal facilities located on the Hanford Site in southeastern Washington State have been used extensively by the U.S. government to produce nuclear materials for the U.S. strategic defense arsenal. Currently, the Hanford Site is under the stewardship of the U.S. Department of Energy (DOE) Office of Environmental Management (EM). A large inventory of radioactive and mixed waste, resulting from the production of nuclear materials, has accumulated, mainly in 177 underground single- and double-shell tanks located in the central plateau of the Hanford Site (Mann et al. 2001). The DOE EM Office of River Protection (ORP) is proceeding with plans to immobilize and permanently dispose of the low-activity waste (LAW) fraction onsite in a shallow subsurface disposal facility (Integrated Disposal Facility [IDF]). Pacific Northwest National Laboratory (PNNL) was contracted to provide the technical basis for estimating radionuclide release from the engineered portion of the IDF (source term) as part of an immobilized low-activity waste (ILAW) glass testing program to support future IDF performance assessments (PAs).

1.1 Overview—LAW Glass Disposal at Hanford

Currently, DOE plans to dispose of the glasses made from nuclear waste stored in underground tanks at Hanford at two U.S. locations: 1) the LAW glass will be stored onsite at the IDF and 2) the high-level waste (HLW) glass will be disposed of at a geologic repository (previously Yucca Mountain, Nevada). The solid and liquid waste recovered from the tanks will be pretreated to separate the low-activity fraction from the high-level and transuranic waste fractions. The LAW and HLW fractions will be immobilized into a vitrified matrix (i.e., glass). Vitrifying the LAW is expected to generate over 1.6×10^5 m^3 of glass (Puigh 1999). The volume of ILAW at Hanford is the largest in the DOE complex and is one of the largest inventories (approximately 0.89×10^{18} Bq total activity) of long-lived radionuclides, principally ^{99}Tc ($t_{1/2} = 2.1 \times 10^5$), planned for disposal in a low-level waste (LLW) facility.

Before the ILAW can be disposed of, DOE must conduct a PA for the IDF that describes the long-term impacts of the disposal facility on public health and environmental resources. One of the inputs to the PA is estimates of radionuclide release rates from the engineered portion of the disposal facility (source term). These estimates are expected to be based on chemical reactions that occur in the near-field and are controlled by the dissolution of the vitrified matrix. Therefore, to provide credible estimates, a mechanistic understanding of the basic physical and geochemical processes that control glass dissolution and hence, radionuclide release, must be understood and incorporated into models to effectively simulate the glass-water reaction over the period of regulatory concern (approximately 10 000 years). Apart from glass composition, the dissolution rate is a function of temperature, pH, and solution composition of the fluid contacting the glass. The temperature of the IDF is a known constant, 15°C. However, both pH and composition of the fluid contacting the glass are variables that are affected by flow rate, reactions with other engineered materials, gas-water equilibria, secondary phase precipitation, alkali-ion exchange, and dissolution of the glass itself. Consequently, glass dissolution rates vary both in time and as a function of position in the disposal system. There is no physical constant such as a “leach rate” or radionuclide release rate parameter that can be assigned to the glass waste form in such a dynamic system.

A model based on empirical release behavior of the glass cannot provide feedback regarding the impacts of design options on the disposal-system performance. Therefore, the source-term analysis

requires the use of a reactive chemical transport modeling framework that takes into account the coupled effects of fluid flow and glass-water reactions on the chemistry of fluids percolating through the disposal facility. The fluid chemistry is coupled with kinetic rate equations that describe the response of the glass corrosion rate to changes in fluid composition in the disposal facility or repository, all computed as a function of time and space. These kinetic rate equations assume that 1) the dependence of dissolution and precipitation rates on departure from equilibrium are based on arguments and assumptions of Transition State Theory (TST) and 2) the driving force for the transformation of unstable to stable silicate materials is governed principally by the magnitude of displacement from thermodynamic equilibrium. This technical strategy (McGrail et al. 1998, Mann et al. 2001, McGrail et al. 2001, McGrail et al. 2003) requires the use of a reactive chemical transport code (e.g., Subsurface Transport Over Reactive Multi-phases [STORM]) that integrates the results obtained from bench-scale laboratory test methods and from long-term accelerated weathering tests to simulate and model glass weathering. For the IDF PA program, data collection has been focused on measuring and quantifying the effects of environmentally relevant and sensitive parameters (e.g., effect of pH, temperature, and solution composition) that are needed to simulate and model, with a high level of confidence, the long-term behavior of glass. This methodology is similar to the strategy being used to analyze the Drigg LLW site in the UK (Abraitis et al. 2000, Small et al. 2000).

1.2 Purpose and Report Contents and Organization

The purpose of the PNNL work documented in this report is to summarize the progress made in fiscal year (FY) 2010 toward implementing the strategy with the goal of developing an understanding of the long-term corrosion behavior of low-activity waste glasses.

The ensuing sections of this report provide a brief introduction to the theoretical aspects of glass weathering, modeling the glass-water reaction, and the STORM code (Section 2.0). Section 3.0 discusses and list the oxide composition for each of the glasses discussed in this report. The results from characterization of the glass structure using raman spectroscopy is discussed in Section 4.0. A discussion on the approach used in the geochemical and Monte Carlo modeling calculations are provided in Sections 5.0 and 6.0, respectively. Section 7.0 discusses the progress that has been made in transitioning from the use of STORM to STOMP for the near-field modeling calculations. Section 8.0 provides a compiled list of alteration phases that have been identified in accelerated weathering experiments. Finally, a brief summary of the information contained in this report is provided in Section 9.0.

2.0 Theoretical Considerations for Glass

This section briefly discusses the stages of glass dissolution, the application of a kinetic rate equation to model the glass-water reaction, how rate-law parameters vary with composition, and the numerical computer code used to simulate the glass weathering process over geologic time-scales. We also discuss the technical basis for several of the assumptions used to define the base-case simulations.

2.1 Stages of Glass Dissolution

A large amount of information on the glass–water reaction collected over the past 25 years has been summarized in the ‘‘glass compendium” (Cunnane et al. 1994a, 1994b) and numerous reviews (Barkatt et al. 1986, Hench et al. 1986, Bunker et al. 1988, Casey and Bunker 1990, Werme et al. 1990, Bourcier 1991, Vernaz and Dussossoy 1992, Bourcier 1994, McGrail et al. 1997, Strachan and Croak 2000, Vernaz et al. 2001, Icenhower et al. 2004, Van Iseghem et al. 2007). Based on these reviews, the glass dissolution reaction can be divided into five regimes or stages (Figure 2.1) that occur as the reaction proceeds (e.g., Stage I, II, III, IV, and V).

- Stage I—Initial diffusion or interdiffusion
- Stage II—Initial or forward rate, r_0
- Stage III—Decreasing rate, r(t)
- Stage IV—Residual rate, r_r
- Stage V—Alteration renewal.

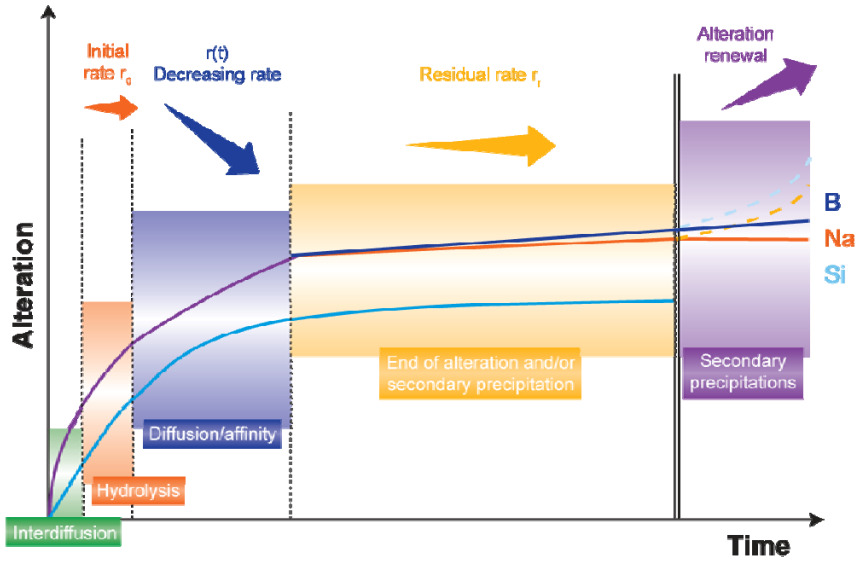

Figure 2.1. General Schematic of the Stages of Glass-Water Reaction

The initial stage (Stage I) of glass weathering begins when network-modifying cations and protons in solution are exchanged, a process referred to as interdiffusion. This mechanism has been identified experimentally during the leaching of numerous glasses, especially in acidic media (Doremus 1975). The process of interdiffusion is followed by two simultaneous reactions: hydration and dissolution of the glass network, commonly referred to as the initial or forward rate (Stage II). In dilute solutions, the TST-based model successfully accounts for silicate dissolution in terms of temperature, pH, and reactive surface area. Stage III is reached as the concentration of dissolved components increases and the build-up of these components approaches the formation of a thermodynamically unstable phase (hydrated surface layer).

During Stage III, the matrix dissolution rate becomes dependent on the solution saturation state (concentration of elements in solution). Therefore, the process of ion exchange reaches a relatively constant rate in accordance with a diffusion-controlled process as a hydrated surface layer (e.g., gel layer) develops on the surface of the glass over time. The hydrated surface layer forms when relatively insoluble glass components (i.e., Al, Fe, and Si) accumulate in the bulk solution and condense at the glass-water interface. Unlike the rate of ion-exchange, the dissolution rate of the glass network decreases because of the common ion effect (i.e., as the solution becomes more concentrated in glass components). The difference in chemical potential between the glass and aqueous phase decreases, which decreases the dissolution rate—corresponding to an incongruent release of B, Na, and Si. This decrease in the rate of matrix dissolution is partially caused by the effect H_4SiO_4(aq) has on the dissolution rate and the formation of the hydrated surface layer (Abraitis et al. 2000, Pierce et al. 2004a, Pierce et al. 2008a, Pierce et al. 2008b). In other words, as the activity of H_4SiO_4(aq) increases in the aqueous solution, the rate of glass dissolution decreases. It is important to note that in the case of glass, the dissolution rate cannot become zero because silicate glasses are thermodynamically unstable in water.

During Stage IV, the solution becomes saturated, and secondary minerals begin to form. The alteration phase is often a clay mineral, such as a smectite or chlorite (Pierce et al. 2007). The precipitation kinetics associated with these phases can be complex, but in general, the rate of secondary phase growth increases in response to the increase in magnitude of supersaturation (Nagy and Lasaga 1993, Nagy 2001). Depending on the type of alteration phase, the glass-water reaction can increase from the residual rate and return to a rate consistent with the saturation and pH conditions observed during Stage II (e.g., Stage V—alteration rate renewal). This type of behavior has been observed in accelerated weathering experiments and may be associated with the Al/Fe ratio of the glass formulation (Jantzen 2008).

2.2 Kinetic Rate Equation

A mathematical model that describes glass reactivity is needed to predict the long-term fate of glass in the subsurface over the period of regulatory concern. Over the last few decades, a general rate equation has been fashioned to describe the dissolution of glass (and more ordered materials) into aqueous solution. As described below, the equation is based upon the TST of chemical kinetics in which the overall reaction rate is governed by the slowest elementary reaction. Elementary reactions have simple stoichiometry and can be combined as an overall reaction. In many cases, the elementary reactions can only be inferred. As an example of the elementary reaction, consider the dissolution of SiO_2 polymorphs to form silicic acid:

$$SiO_2(s) + 2H_2O \leftrightarrow SiO_2 \cdot 2H_2O^{\ddagger} \rightarrow H_4SiO_4(aq) \tag{2.1}$$

in which $SiO_2 \bullet 2H_2O^{\ddagger}$ represents an activated complex. Note that a double-headed arrow symbolizing a reversible reaction links the reactants and the activated complex in Equation (2.1). Equation (2.1) also illustrates that the TST formulation assumes that the decay of the activated complex is an irreversible reaction.

Previous studies have established that the corrosion rate of silicate waste glasses is a complex process that depends strongly on temperature, pH, and the chemical composition of the aqueous solution contacting the glass (Cunnane et al. 1994a, 1994b and the references contained therein). When the aqueous solution is dilute, the glass dissolves at a characteristic forward rate that depends only on glass composition, temperature, and solution pH (McGrail et al. 1997). In static systems, or where the rates of mass transport by fluid flow are slow, dissolution releases glass components into the aqueous solution, and the concentrations of these elements in the contacting fluid increase. The buildup of these dissolved components leads to slower glass corrosion rates as the contacting solution becomes more concentrated. As solution concentrations of dissolved elements continue to increase, solubility limits with respect to secondary phase(s) are reached, and these phases may begin to precipitate. Because silicate glasses are meta-stable solids, thermodynamics dictates that the glass will continue to dissolve or transform into more stable alteration phases. The key factor controlling long-term durability of waste glasses is the rate at which this processes proceeds.

The rate law that appears to best describe this overall dissolution behavior developed by Aagaard and Helgeson (1982) and applied to glass by Grambow (1985) is presented as follows:

$$r_i = \vec{k}_o v_i a_{H^+}^{\eta} \exp\left(\frac{E_a}{RT}\right)\left[1-\left(\frac{Q}{K_g}\right)^{\sigma}\right]\prod_j a_j \qquad (2.2)$$

where
r_i = dissolution rate, g m^{-2} d^{-1}
$\vec{k}_0$ = intrinsic rate constant, g m^{-2} d^{-1}
v_i = mass fraction of component *i*, unitless
a_{H^+} = hydrogen ion activity (variable to be calculated by STORM)
E_a = activation energy, kJ/mol
R = gas constant, kJ/(mol·K)
T = temperature, K (assumed constant at 15°C)
Q = ion activity product for Glass (variable to be calculated by STORM)
K_g = pseudo-equilibrium constant
η = pH power law coefficient
σ = Temkin coefficient (σ = 1 assumed).

The chief virtue of Equation (2.2) is that it can be directly input into reaction-transport codes for simulating the dissolution behavior of glass under specific storage conditions. Another benefit of Equation (2.2) is that it is solidly based on the TST of chemical kinetics in which a series of reaction rates are governed by the slowest elementary reaction. Therefore, it is simply necessary to ascertain the "rate limiting" step in dissolution rather than attempt to fully understand all of the possible reactions and kinetic pathways that can occur during the reaction of glass with aqueous solution. Because this rate-limiting step is an "elementary reaction," the stoichiometry of the reaction is typically simple and can be easily defined in a reactive transport model.

In addition, test results with LAW and bulk vitrification glasses (excluding LAWB45) show that it is susceptible to a secondary reaction mechanism, alkali ion exchange. This reaction results in the selective extraction of Na via the reaction:

$$\text{LAWA44-Na} + H^+ \rightarrow \text{LAWA44-H} + Na^+ \tag{2.3}$$

where LAWA44-Na represents the unreacted glass containing Na, and LAWA44-H represents a hydrated glass where the Na has been replaced with an equimolar amount of hydrogen. The rate of this ion-exchange reaction, referred to hereafter as r_{IEX}, has been determined from single-pass flow-through (SPFT) experiments (Pierce et al. 2004a, Pierce et al. 2005). In the STORM code, the ion exchange reaction is taken into account as the amount of hydrated glass is formed via Equation (2.3), and that hydrated glass is allowed to dissolve according to the same kinetic rate law, Equation (2.2), as the parent glass.

3.0 Glass Formulations

The test results presented in the following sections will reference a number of different ILAW glass compositions, one model glass composition (HAN28F), and several chemically simple glass formulation (namely three and four component glasses). These are provided in Table 3.1 for reference. The ILAW glasses span the alkali range (from 21.5 to 7.9 wt%)[1], and the molar ratio of sulfate to sodium (SO_4/Na)[2] (from 0.03 to 0.006) and potassium to sodium (K/Na)[3] (from 0.129 to 0.004) expected for candidate ILAW glasses to be produce by WTP. In addition to the ILAW glasses, a model glass composition, HAN28F, is being used to validate the underlying physical and chemical processes simulated by the STORM code.

The LAW glasses were prepared by mixing measured amounts of dried reagent-grade chemicals (oxides, fluorides, iodides, and sulphides) in an agate mill. The mixtures will be melted in a platinum-rhodium ($Pt_{10}Rh_{90}$) crucible, and the molten glass will be poured onto a cool stainless steel plate. Each glass will then be subjected to heat treatment by placing the glass in a preheated oven at 930ºC and then cooled at 21ºC per hour. This cooling rate is consistent with a computed thermal profile for a 1.2m × 1.2m × 1m container that was the design being considered for LAW. The container design has since been modified to a cylinder of 1.2m diameter × 2.3m tall.

The HAN28F model glass was designed to corrode relatively rapidly and to provide a strong signal for the release of I, Re, and Se, which have been incorporated in the glass as non-radioactive analogs for ^{129}I, ^{99}Tc, and ^{79}Se, respectively. The concentration of these components in HAN28F glass has also been significantly increased over their expected concentration in a typical radioactive ILAW glass to further enhance the detection of these elements in the surrounding soil under burial conditions.

The chemically simple glasses were prepared by mixing reagent grade chemicals (Al_2O_3, Na_2CO_3, H_3BO_3, HfO_2, MoO_3, and SiO_2) together in a ceramic ball mill. The mixtures were melted at 1500°C for 1-hour in a $Pt_{10}Rh_{90}$ crucible and then quenched on a steel plate. The resulting glass was then ground and re-melted in a covered $Pt_{10}Rh_{90}$ crucible. After an additional hour at melt temperature, the melt was poured into a mold to yield bars with approximate dimensions of 1.5-cm × 1.5-cm × 3.8-cm. The bars were then annealed for 2 hours in a box furnace at 570°C. Following the annealing stage, the furnace was turned off and the bars were allowed to cool to ambient temperature overnight. These glasses contain the major components of ILAW glasses. Hafnium contained in the Hf-series glasses represents the high-field strength cation zirconium, which is contained in ILAW glasses at 1.0 to 2.0 wt%. Each of the chemically simple glasses discussed below, have been used to provide the structural information needed to analyze Raman spectra and parameterize the Monte Carlo model. It is important to note that several of the advance silicate glass formulations currently being evaluated is expected to contain as much as 6.0 wt% ZrO_2.

[1] Alkali range was calculated from the $Na_2O + 0.66 \times K_2O$.
[2] SO_4/Na molar ratio is calculated from the SO_3/Na_2O ratio by multiplying by 30.99/80.06.
[3] K/Na molar ratio is calculated from K_2O/Na_2O ratio by multiplying by 30.99/47.10.

Table 3.1. Composition (weight%) of Select Low-Activity Waste Glass, a Model Glass (HAN28F), a Reference High-Level Waste Glass, and the Glasses Studied in Pierce et al. 2010.

	Low-Activity Waste Glasses								Model Glass	HLW	Pierce et al. 2010				
Oxide	**LAW A44**	**LAW B45**	**LAW C22**	**A1 C1-1**	**A1-AN105R2**	**LAW E-1A**	**LAW E-95A**	**LAW E-290A**	**HAN 28F**	**SRL 202**	**NeB0**	**NeB1**	**NeB2**	**NeB3**	**NeB4**
Al_2O_3	6.20%	6.13%	6.08%	6.09%	6.10%	6.10%	6.10%	6.10%	10.15%	4.71%	35.88%	29.37%	22.55%	15.40%	7.89%
B_2O_3	8.90%	12.34%	10.06%	9.13%	8.84%	10.00%	10.00%	10.00%	2.00%	6.91%	-	5.02%	10.27%	15.78%	21.57%
CaO	1.99%	6.63%	5.12%	2.74%	1.96%	2.03%	6.94%	5.93%	2.59%	1.10%	-	-	-	-	-
Ce_2O_3	-	-	-	-	-	0.00%	0.01%	0.01%	n.d.	-	-	-	-	-	-
Cl	0.65%	0.01%	0.09%	0.91%	1.17%	0.20%	0.01%	0.14%	0.13%	-	-	-	-	-	-
Cr_2O_3	0.02%	0.07%	0.02%	0.02%	0.02%	0.02%	0.05%	0.03%	0.08%	0.33%	-	-	-	-	-
Cs2O	-	-	-	0.15%	0.15%	-	-	-	-	-	-	-	-	-	-
F	0.01%	0.08%	0.16%	0.09%	0.00%	0.29%	0.10%	0.06%	0.31%	0.36%	-	-	-	-	-
Fe_2O_3	6.98%	5.26%	5.43%	6.50%	6.87%	5.50%	5.50%	5.50%	2.53%	12.40%	-	-	-	-	-
K_2O	0.50%	0.26%	0.10%	0.35%	0.44%	3.73%	0.24%	0.09%	1.96%	1.99%	-	-	-	-	-
Li_2O	-	4.62%	2.51%	0.62%	0.00%	n.d.	4.18%	2.75%	n.d.	4.48%	-	-	-	-	-
MgO	1.99%	2.97%	1.51%	1.85%	1.96%	1.48%	2.60%	1.49%	1.18%	1.49%	-	-	-	-	-
MnO_2	-	0.00%	0.04%	-	-	-	-	-	-	3.23%	-	-	-	-	-
MoO_3	0.01%	-	-	-	-	-	-	-	-	-	-	-	-	-	-
Na_2O	20.00%	6.50%	14.40%	19.17%	20.66%	19.05%	7.75%	14.10%	28.62%	7.82%	21.82%	22.32%	22.86%	23.41%	24.00%
Nd_2O_3	-	-	-	-	-	-	-	-	-	0.35%	-	-	-	-	-
NiO	-	0.00%	0.03%	0.01%	-	0.00%	0.00%	0.02%	-	1.05%	-	-	-	-	-
P_2O_5	0.03%	0.03%	0.17%	0.03%	-	0.12%	0.06%	0.56%	1.90%	-	-	-	-	-	-
PbO	-	0.00%	0.02%	-	-	0.00%	0.00%	0.01%	-	0.16%	-	-	-	-	-
SiO_2	44.55%	47.86%	46.67%	44.48%	43.82%	43.20%	47.90%	44.80%	42.56%	50.92%	42.30%	43.29%	44.32%	45.40%	46.53%
SO_3	0.10%	0.84%	0.34%	0.21%	0.18%	0.38%	0.66%	0.51%	0.30%	-	-	-	-	-	-
Re_2O_7	0.10%	0.01%	0.01%	-	-	-	-	-	-	-	-	-	-	-	-
TiO_2	1.99%	0.00%	1.14%	1.76%	1.96%	1.40%	1.40%	1.40%	0.38%	0.24%	-	-	-	-	-
ZnO	2.96%	3.15%	3.07%	2.95%	2.92%	3.50%	3.50%	3.50%	n.d.	0.09%	-	-	-	-	-
ZrO_2	2.99%	3.15%	3.03%	2.96%	2.94%	3.00%	3.00%	3.00%	5.00%	1.19%	-	-	-	-	-
Total	99.97%	99.91%	99.99%	100.0%	100.0%	100.0%	100.0%	100.0%	100.0%	98.82%	100.0%	100.0%	100.0%	99.99%	99.99%

4.0 Glass Characterization

4.1 Raman Spectroscopy

The objectives of work this year was to collect Raman spectra of unreacted and reacted glasses. These include a combination of chemically simple and complex (e.g., ILAW glass) glass formulations. The purpose of the Raman spectra for the chemical simple glasses was to obtain the appropriate spectral assignments to assist in the interpretation of the spectra obtained from the chemically complex glasses. At this time only the interpretation of the results from a select number of chemically simple glasses had been completed. Additional spectra are included in Appendix A, but the results have not been completely analyzed.

4.1.1 Raman Analysis Method

All Raman spectra were collected using a Horiba JY (Edison, NJ)) LabRAM HR (high resolution) Raman (confocal) microscope system. With a focal length of 0.8 m and dual gratings with groove density of 2400 grooves/mm the instrument can achieve a nominal spectral resolution of about 1 cm^{-1}. Excitation was provided by the 244-nm line of a Lexel (Fremont, CA) Model 85-SHG frequency-doubled a ion laser equipped with a non-linear BBO (beta barium borate) crystal. Laser power was 25 mW at the source and approximately 2 mW at the sample. A 40× UV-compatible microscope objective (NA = 0.75) was used. The spectrometer pinhole was kept fairly large, at 400 μm, resulting in less-than-optimal depth and lateral resolution. However, laser throughput was improved with the larger pinhole, giving exceptionally high Raman intensities, in some cases tens-of-thousands of counts when collected with a relatively short exposure time (200 s). The spectra range was restricted to Raman shift above 450 cm^{-1}. Measurements at lower frequencies were not possible because of the presence of a factory-installed edge filter for eliminating the exciting line. As a consequence, Raman bands associated with deformation modes, commonly observed below 500 cm^{-1}, were not observable in this study. Instead, focus was on the stretching modes, both network and those involve NBOs, which occur at higher frequencies.

4.1.2 Raman Analysis Results

Deep-UV Raman spectra of glasses in the RD and RE series are shown in Figure 4.1. The single glass in the AB series is not shown but its composition is similar to RD33 and RE20 in that it is essentially the "trisilicate" composition, although this one contains a trace amount of MoO_3. As expected, the spectra of RD33, RE20 and A0B5 resemble each other closely. The spectra of all of the glasses in this study, both the "trisilicate" composition and those richer in silica, contain an envelope of several strong bands between 850-1300 cm^{-1} and, within this region, there is a particularly strong band between 1070-1100 cm^{-1} indicative of SiO_4 tetrahedra containing one non-bridging oxygen atom, i.e. a Q^3 structure. Parkinson et al. (2008) reports this band at 1060 cm^{-1} in a series of borosilicate glasses with higher B content and, generally in silicates the corresponding mode is closer to 1100 cm^{-1} (Parkinson et al. 2008, Brawer and White 1977). A recent study by Lenoir et al. (2008) reports Q^3 at 1087 cm^{-1} for a glass with composition close to RD67. The higher frequency shoulder, centered at approximately 1150 cm^{-1}, is assigned to Q^4, as is a portion of the intensity on the low-frequency side of Q^3, which arises from a small band at approximately 950 cm^{-1}. This assignment is in accord with others (Parkinson et al. 2008, Lenoir et al. 2008). Parkinson et al. (2008) associates Q^4 in borosilicate glasses with bands at 1150 cm^{-1} and 970

cm^{-1}. Attributing the 950 cm^{-1} band to a component of Q^4 is reasonable for borosilicate glasses since there should be a significant amount of tetrahedral BO_4 units bridged into the SiO_4 silica network without the formation of non-bridging oxygen atoms. Vibrational modes involving mostly B-O stretch within this network should appear at lower frequencies (because of the weaker BO_4 bonds) than equivalent modes involving either SiO_4 tetrahedra alone or BO_3 triangles.

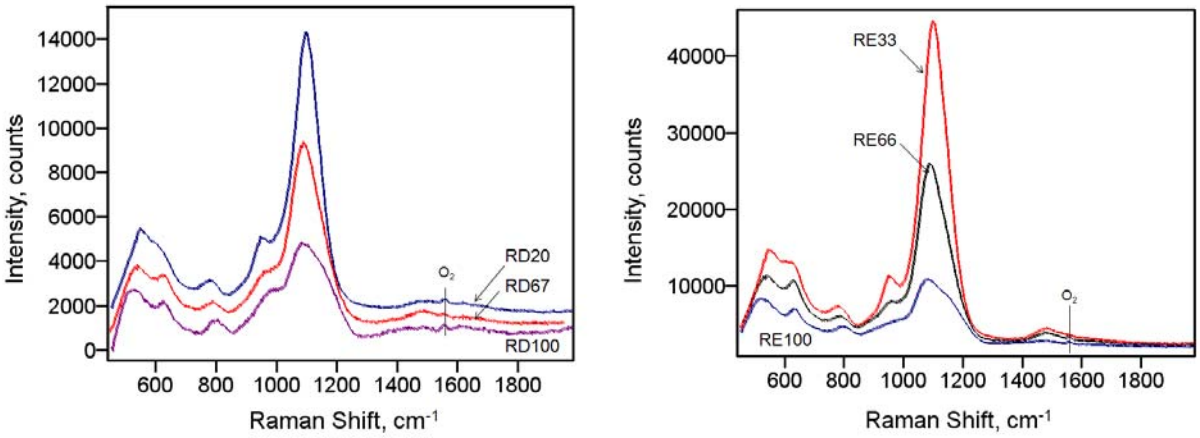

Figure 4.1. Deep-UV Raman spectra of RD (left) and RE (right) series glasses.

A second, much weaker, lower-frequency Q^3 band is also proposed at approximately 990 cm^{-1}, consistent with Parkinson, et al. (2008) and others (Tan et al. 2004, Konijnendijk et al. 1975) on silica-rich glasses. The inclusion of this second Q^3 band improved the fits significantly. Finally, a very weak Q^2 band was added at about 900 cm^{-1} to explain the shape of the tail of the envelope of bands associated with Q^n units. The Q^2 bands are reported to appear between 900-950 cm^{-1} (Lenoir et al. 2008). Although insignificant Q^2 is expected for these silica-rich compositions based on ^{29}Si MAS NMR (Parkinson et al. 2008), as in the case of the weaker Q^3 band, both a qualitative inspection of the spectra and the results of repeated curve-fitting attempts suggested that some of these structures are, in fact, present. As shown by the results of curve fits discussed below, the amount of Q^2 is very small and does not appear to change much across the composition range studied in this work.

The region between 700-1300 cm^{-1} was fit to six Gaussian bands in line with the assignments discussed above involving Q^n units, and with the addition of a weak band between 780- 800 cm^{-1}. The latter is in a region that is not usually associated with stretching modes from Q^n units but instead from deformation modes or modes involving one or more medium-size structures containing B (Parkinson et al. 2008). Although the region below 800 cm^{-1} was not of primary interest in this work, incorporating the well-resolved band between 780 and 800 cm^{-1} improved the quality of curve fits significantly, particularly in regard to the lower portion of the Q^n envelope. A typical curve fit employed in this study is shown in Figure 4.2. Note the strong Q^3, named Q^3a, centered below 1100 cm^{-1} and the accompanying smaller Q^3, named Q^3b, close to 1000 cm^{-1}. The Q^4 assignments, named Q^4a and Q^4b, are in accord with Parkinson et al. (2008).

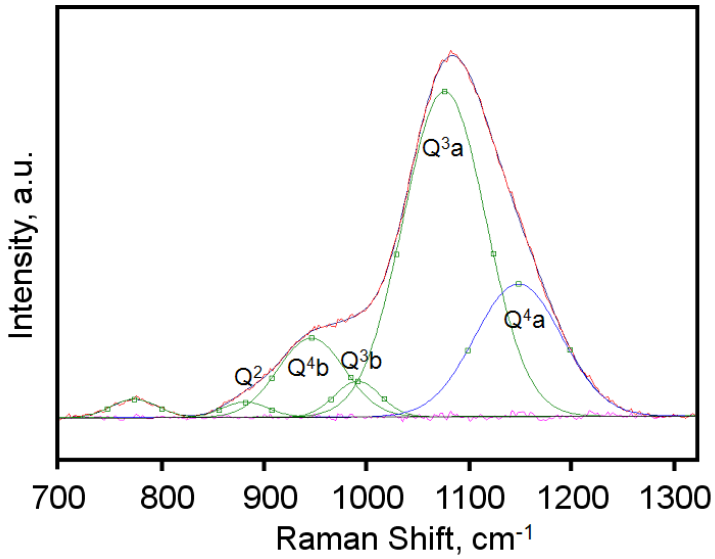

Figure 4.2. Example Curve Fit for 700-1300 cm^{-1} region of the Deep-UV Raman Spectra of the Borosilicate glasses for (RD67 is shown). Spectrum Analysis is Based upon an approach Developed by Parkinson et al. (2008). Residuals are Illustrated along the Baseline.

Unconstrained curve fitting using the collection of six bands described above produced convergent results but the solutions were unsatisfactory. Solutions were non-unique in several cases, and the Q^4a band often became very intense and wandered (during curve fitting) to 1100 cm^{-1} and below. Based on the spectral assignments discussed above, including a principal Q^4 band above 1100 cm^{-1} and almost always at 1150 cm^{-1}, the behavior of the predicted Q^4 component seemed unreasonable. Consequently we elected to impose a constraint during the Gaussian curve fits: holding the Q^4a band at a fixed frequency (= 1150 cm^{-1}). The intensity and bandwidth of Q^4a, along with the frequencies, intensities and bandwidths of the remaining five bands, were permitted to vary to achieve the best fit. With this single constraint in palace, the curve fitting results followed a consistent pattern with respect to relative intensities and exhibited residuals typical of that shown in the Figure 4.3 with R^2 values of 0.9990 or better. In addition, as shown in Figure 4.3, the peak frequencies determined from the curve fits varied only slightly over the composition range (determined by Na_2O content) and, in all cases, remained within spans of frequencies consistent with the spectral assignments in the literature that were discussed above.

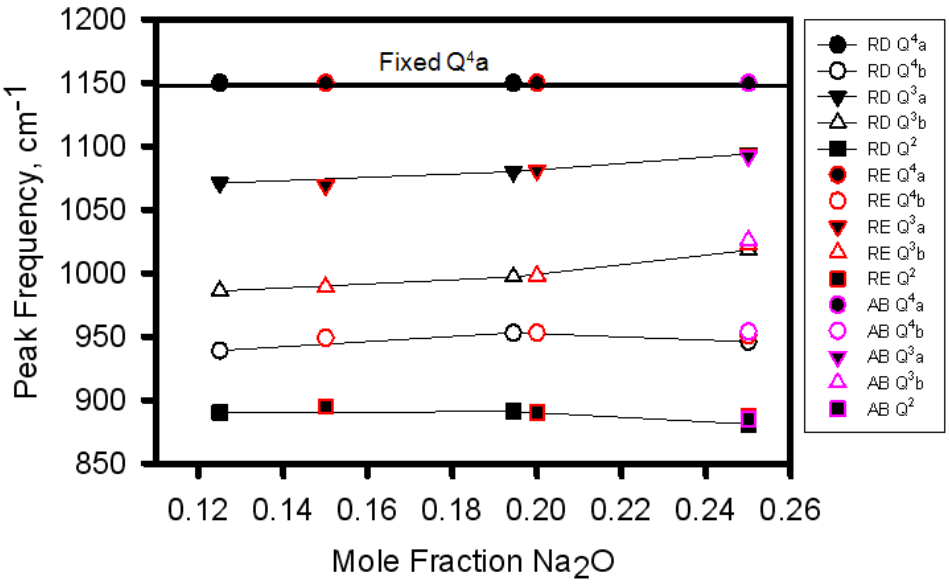

Figure 4.3. Plot of Deep-UV Raman Peak Frequencies from Results of Curve Fits and Assignments Based on Parkinson et al. (2008).

Curve fitting of the 700-1300 cm^{-1} region yielded integrated intensities or areas of the peaks associated with each Q^n structure. Although a direct correlation of these areas to a quantitative distribution of the Q^n structures can be problematic (because Raman band arising from different vibrational modes do not necessary have the same scattering cross-sections), extensive study of glass spectra of similar compositions supported by other techniques, particularly ^{29}Si NMR, has led to defensible strategies for using the areas of the Raman bands for this purpose. In one method (Parkinson et al. 2008), the fraction of Q^3 was calculated by rationing the sum of area of the Q^3 (i.e. the sum of Q^3a and Q^3b) against the total area in the Q^n envelope (total area associate with all Q^2, Q^3 and Q^4 structures). The results of applying this approach to spectra obtained in our work, shown in the plots in Figure 4.4, give a clear indication that the Q^3 fraction increases with increasing mole fraction of Na_2O in the glass, decreases as a fraction of B_2O_3 and increases as a function of the Na_2O/B_2O_3 ratio. The effect of Na_2O (Figure 4.4a) is consistent with many published studies (see, for example, Mysen et al. 1982 and Furukawa and White 1981) that argue the role of network modifiers like Na is to depolymerize the SiO_4 network by creating NBOs. Over the composition range in our study, this appears to be accomplished primarily by creating Q^3 units at the expense of Q^4. The effect would be enhanced by the simultaneous removal of B_2O_3 (Figure 4.4b) since B is mostly present in the form of tetrahedrally coordinated BO_4 units, a sink for NBOs that otherwise would occur on Si. The assessment is line with arguments made by Fukukwa and White (1981) that, when $Na_2O/B_2O_3 > 1$, Na^+ ions distributed between silicate and borate units approximately in proportion to the concentration ratio of Si to B. The overall effect is a direct dependence of Q^3 on the Na_2O/B_2O_3 ratio (Figure 4.4c). Interestingly, Fukukwa and White (1981) distinguish a different behavior when $Na_2O/B_2O_3 < 1$ that they attribute to a preference of Na^+ ions for borate groups (over silica groups). As shown in Figure 4.4c, the Q^3 fraction appears to show greater sensitivity to Na_2O/B_2O_3 when the ratio drops to unity. Although the reason for this is debatable, it would not be unexpected if conditions were such that Q^3 concentration was "driven to zero" under conditions where all of the NBOs were essentially scavenged by borate groups.

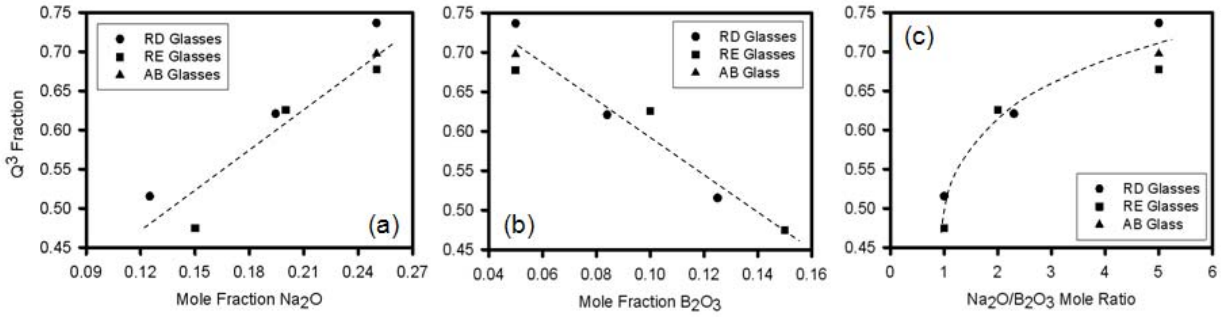

Figure 4.4. Plot of Q^3 Fraction Versus Compositional Parameters for the RD and RE Series Glasses, as well as AB compositions Containing Na_2O and B_2O_3, but no Al_2O_3.

As shown in Figure 4.5, calculation of the fraction of Q^2, using an approach similar to that described above for Q^3, suggests the fraction of Q^2 drops slightly over the concentration range but the conclusion is a weak one. Note that the range in the value of Q^2 over all of the concentrations in Figure 4.5 (about 0.015) is significantly less than the maximum deviation of the points in Figure 4.4 (approximately 0.05). This means that the uncertainty in the Q^2 values is too high for an accurate assessment of any variation in Q^2 and that the most we can say with confidence is that the Q^2 fraction is itself small and that it varies very little over the concentration range compared to the Q^3 fraction.

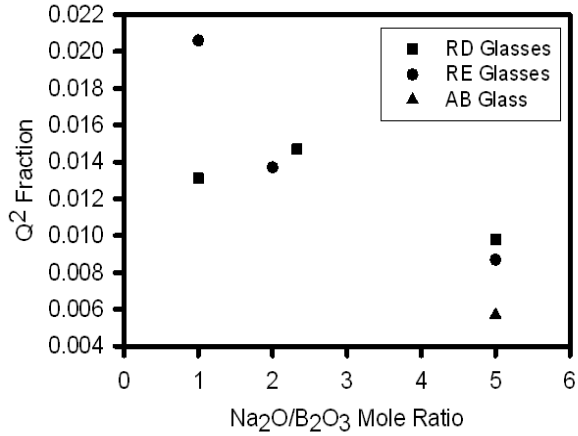

Figure 4.5. Plot of Q^2 Fraction versus Na_2O/B_2O_3 Mole Ratio for the RD and RE Series Glasses, as well as AB Composition Containing Both Na_2O and B_2O_3, but no Al_2O_3.

The 1300-1800 cm^{-1} region of the Raman spectrum of the borosilicate glasses studied in this work also contains some Raman bands that are much weaker than those discussed above. Other than the relatively sharp band near 1550 cm^{-1} due to atmospheric O_2, and the broad band above 1600 cm^{-1} in the spectra of the RD glasses that probably arises from moisture (the bending mode of H_2O is at approximately 1640 cm^{-1}), bands in this region arise from B-O stretching modes involving mostly BO_3 triangles with one NBO (Chryssikos et al. 1990). The bands are particularly well resolved in the spectra of the RE glasses that generally have slightly lower silica content than the RD glasses. Although there

appears to be an increase in the intensity of these bands with Na_2O concentration (RE33 has the most Na_2O), the observation is based on absolute Raman intensities so the trend should be regarded with caution. It is interesting that there is also a coincident weakening of a band near 620 cm^{-1} with higher Na_2O concentration. If this band arises from rings containing one or more covalently bonded tetrahedral BO_4 units as previously proposed (Lenoir et al. 2008), the trends in the two regions, taken together, may indicate that B-containing rings break up with increasing Na_2O concentration and that one consequence is the formation of a small quantity of partly unbridged BO_3 units.

4.1.3 Summary of Raman Analyses

Deep-UV Raman spectroscopy employing 244-nm excitation was advantageous over visible Raman spectroscopy when applied to glasses in finely powdered form. In particular, both reduced fluorescence background and improved signal-to-noise were realized, the latter approaching a magnitude consistent with the fourth-power scattering law. Raman spectra acquired this way on a silica-rich borosilicate glass powders with compositions at or above the trisilicate composition were successfully curve fit using protocol similar to that previously discussed in the literature. The results demonstrated a systematic variation of Q^3 units in the glass as a function of both Na_2O and B_2O_3 content. Increasing Na_2O was found to raise the fraction of Q^3 units in the glasses systematically. Finally, these will be direct inputs into the Monte Carlo model for the purpose of predicting the gel-layer composition for ILAW glasses.

5.0 Experimental Testing and Geochemical Modeling

5.1 Overview

As part of the project entitled "Immobilized Low Activity Waste (ILAW) Glass Testing for Disposal at IDF," a laboratory testing program is being performed at PNNL for Washington River Protection Solutions, Inc. to develop a chemical reaction network of secondary phases that form during the weathering of LAW glasses for future IDF PAs. In this work, a combination of geochemical and stochastic MC modeling simulations and experimental solid phase characterization techniques will be conducted to develop the technical basis for relating glass composition to secondary phase formation. The chemical reaction network of secondary phases determined for LAW glasses will be used as input for STOMP simulations of the IDF for ILAW. The STOMP code will be used to provide the near-field radionuclide release source term for the future IDF-PAs.

The tasks discussed here support two separate but related phases of work. The Phase I work scope focuses on acquiring the information needed to support future IDF PAs based upon specific glass formulations, whereas the Phase II work scope seeks to develop a technical basis for relating ranges of glass compositions to the formation of specific suites of secondary phases. The objective of this Phase II work is to reduce the amount of experimental and modeling work required when new glass formulations are developed.

This section of the report summarizes the progress made in FY2010 on these tasks. Some of the preparatory modeling work conducted will be beneficial to both Phase I and Phase II and is described before the accomplishments that are applicable specifically to Phases I and II.

5.2 Geochemist's Workbench® for Modeling Secondary Phase Formation During Glass Corrosion

In the previous ILAW studies, the geochemical modeling program EQ3/EQ6 (Wolery and Daveler 1992) was used to model experimental ILAW glass weathering data for determining chemical reaction networks of secondary phases that form during glass weathering. Beginning this year, it is anticipated that the program Geochemist's Workbench® (Bethke and Yeakel 2009) will also be used for reasons of convenience, which include convenient input and output interfaces and user-friendly graphical data presentation capabilities. The same thermodynamic database used previously for geochemical modeling of ILAW data with EQ3/EQ6 is also available in the suite of thermodynamic databases available in Geochemist's Workbench®. To confirm that the Geochemist's Workbench® was computationally equivalent to EQ3/EQ6, a validation and verification exercise was completed using the same input data set (from LAWA44) and the same thermodynamic data file. The details of the approach and results of the validation and verification exercise were documented in a Validation and Verification Plan and Validation and Verification Report that has been added to the project records. The conclusions of the report indicated that both the Geochemist's Workbench® and EQ3/EQ6 are computationally equivalent.

5.3 Description of Geochemical Modeling Approach for Determining Secondary Phase Formation During Glass Corrosion

To determine the suite of secondary phases that form during corrosion of a particular glass sample, the React Module of Geochemist's Workbench® (Bethke and Yeakel 2009) is used to trace a reaction path that takes place as a particular sample of glass dissolves in water. To set up the model, the glass composition is placed in an input file in terms of its component metal oxide composition, e.g., SiO_2, B_2O_3, Al_2O_3, and Na_2O. In the case of the halides, these components are added as their elemental gases, e.g., F_2 and Cl_2. The quantity of material included in the input file is set to equal one mole of glass. This is done so that when one mole of glass dissolves, the reaction progress equals 100 percent. The input file is also set up so that the solution in which the glass dissolves is in equilibrium with air (the oxygen fugacity is set to 0.21 atmospheres, and the CO_2 fugacity is set to $10^{-3.5}$ atmospheres). As an increment of reactant (glass in our case) is added to water, its components are initially completely dissolved in the water and are then allowed to come to equilibrium. The model accounts for all possible aqueous species that could potentially form, redox reactions that could occur, and mineral species that could precipitate at equilibrium (based upon the thermodynamic database that is used). If the saturation index (SI) of a particular mineral phase exceeds 1.0, it will precipitate until the solution attains an equilibrium status (SI = 1.0 or less for all minerals considered). The program keeps track of how much glass has dissolved, which phases and quantity of minerals have precipitated, and the solution composition and speciation in equilibrium with the suite of minerals that have dissolved or precipitated.

To develop the correct mineral phases for the chemical reaction network, it is necessary to eliminate a large number of the phases from consideration for the following reasons: 1) the formation of some phases is kinetically inhibited at the disposal system temperature of 15°C, 2) the selection of some phases will violate the Gibbs phase rule, 3) the simulations need to be consistent with experimental observations, therefore phases that generate solution compositions that are inconsistent with these observations will be eliminated from consideration, or 4) the stability of these phases must be consistent with the range of chemical conditions expected for the ILAW disposal system. The bulk of the final set of phases appropriate for each glass type will be determined by simulating the solution chemistry observed in product consistency test (PCT) experiments.

In addition to the computer simulations, characterization of alteration products is used to identify key secondary phases that are required to constrain the computer simulations. Alteration products formed at the surfaces of the glass in the Pressurized Unsaturated Flow Test (PUF) and PCT experiments are characterized by X-ray diffraction (XRD), scanning electron microscopy/energy dispersive spectroscopy (SEM/EDS), and transmission electron microscopy (TEM). In addition to characterization of secondary phase alteration products, changes in the structure of the glass as it weathers will be characterized by nuclear magnetic resonance (NMR) and Raman spectroscopy. These data will be used to verify and validate phases used in the modeling work that cannot be characterized with the methods described above.

5.3.1 Phase I—Experimental

Experimental characterization work that has been conducted to date includes XRD analyses for a number of glass samples collected from PUF and PCT tests. These include LAWB45 and LAWC22 from PUF tests and H28-10A-2, SRL-10A-S, 052010D, LC22-10A-S, and LB45-10A-S from long-term PCTs

(PCT-B) conducted at PNNL (Figure 5.1). Only two of the samples contained peaks that indicated the presence of crystalline material; the rest all appear to be completely amorphous.

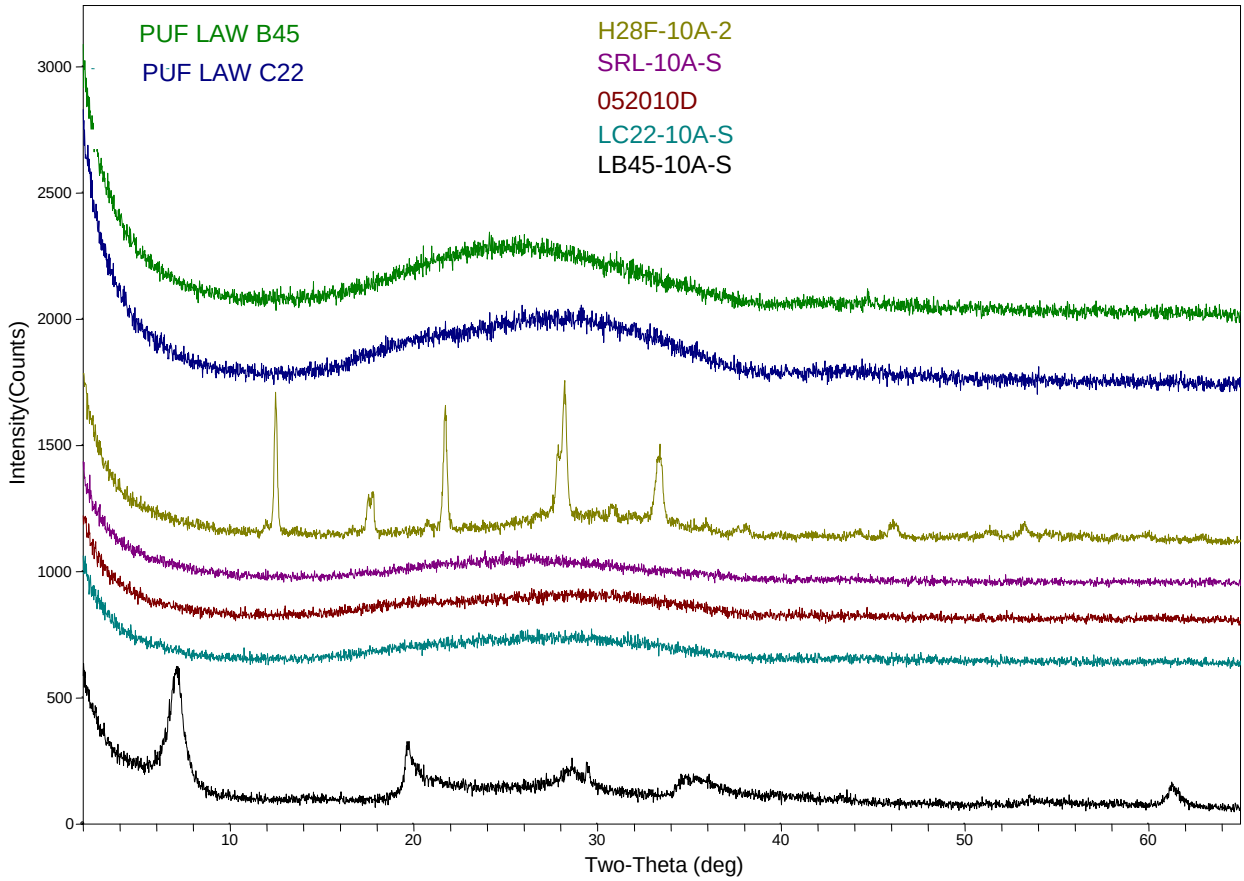

Figure 5.1. XRD Patterns for ILAW Glass Samples LAWB45 and LAWC22 from PUF tests and H28-10A-2, SRL-10A-S, 052010D, LC22-10A-S, and LB45-10A-S from PCTs

The as-measured XRD pattern for the glass sample H28F-10A-S collected at the end of a PCT is shown in Figure 5.2. Below the measured pattern are standard patterns of two phases that provided the best fit to the measured pattern. A range of Na Al silicate phases were determined with JADE to be close matches to the measured XRD pattern. The top pattern (1-74-1787) scored highest with JADE, but the pattern for the hydrated compound (04-011-7946) at the bottom is favored because it matches the peak splitting observed in the XRD spectra.

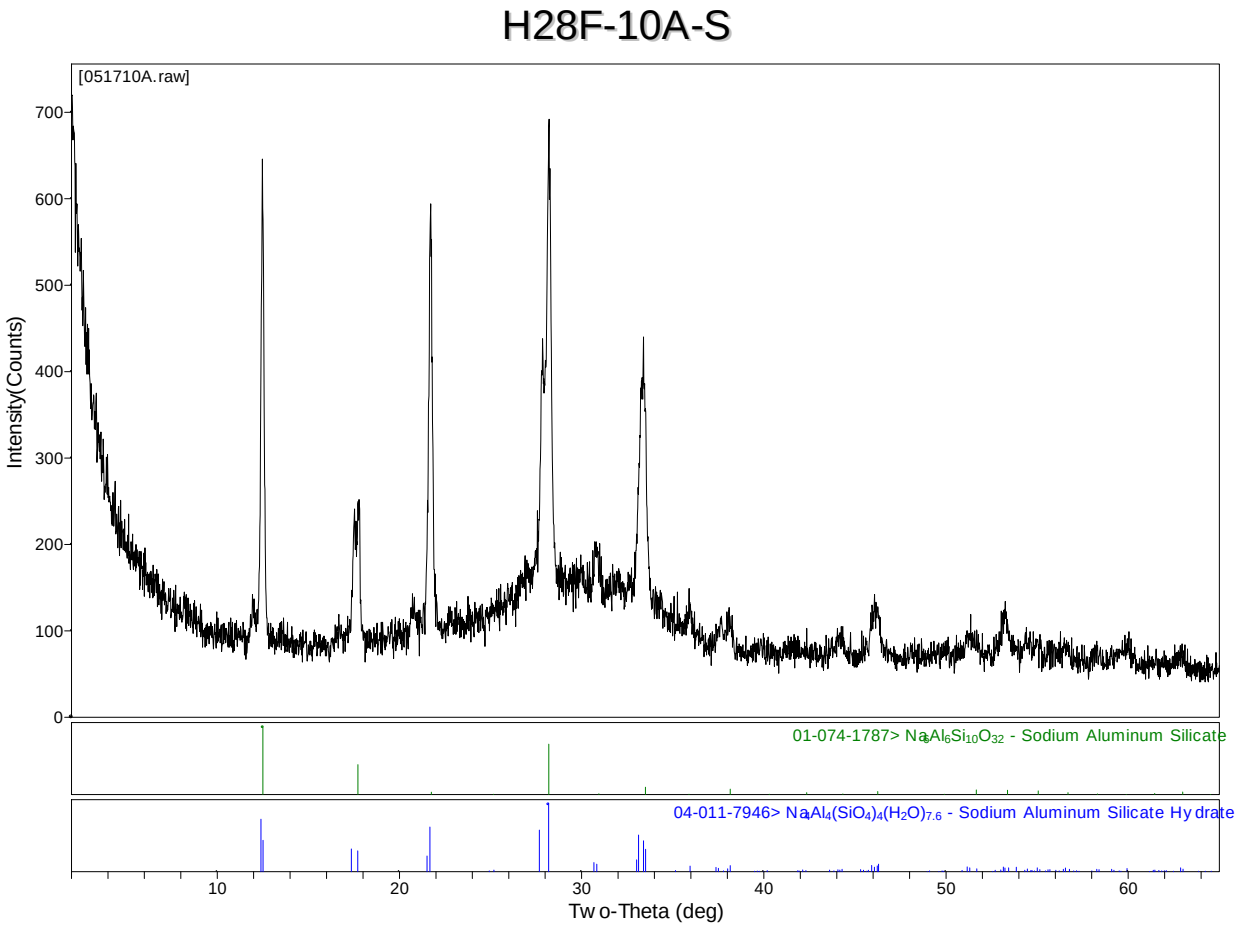

Figure 5.2. As Measured XRD Patterns for Glass Sample H28F-10A-S Collected at the End of a PCT

The as-measured XRD pattern for the glass sample LB45-10A-S collected at the end of a PCT is shown in Figure 5.3. Below the measured pattern is a standard pattern for the Na Al silicate phase $Na_{0.61}Al_{4.70}Si_{7.32}O_{20}(OH)_4$ (ICDD 00-47-197) that provided the best match to the measured pattern. The peak's fits were not aligned particularly well, which suggests that the actual phase may have a crystal structure that is somewhat different than this particular phase. By making small changes to the unit cell, it is possible to obtain better fits to the measured pattern. This suggests that the actual phase may have a crystal structure that is somewhat different that this particular phase and would imply that the Na/Al/Si/OH stoichiometry is somewhat different than that of $Na_{0.61}Al_{4.70}Si_{7.32}O_{20}(OH)_4$.

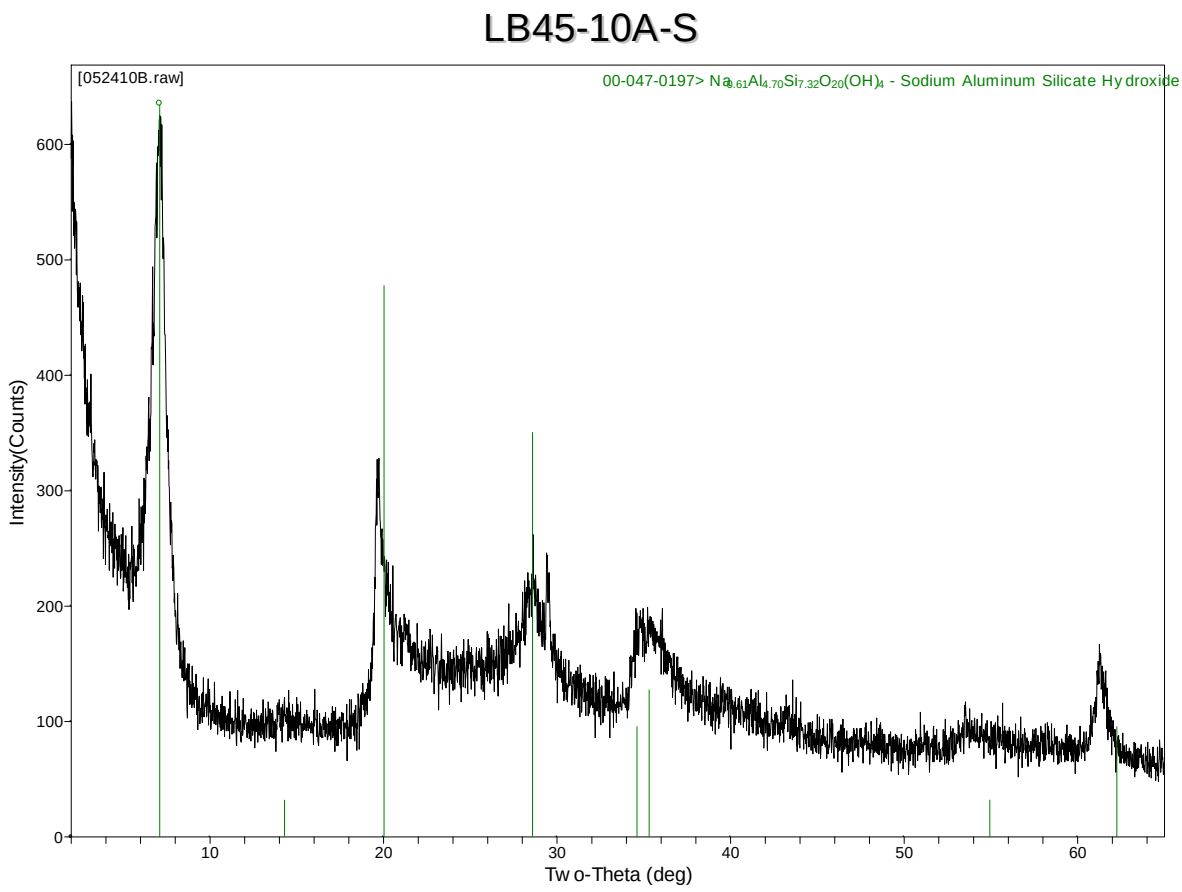

Figure 5.3. As Measured XRD Patterns for Glass Sample LB45-10A-S (LAWB45) Collected at the End of a PCT

5.3.2 Phase I—Modeling

As part of the Phase I modeling work, chemical reaction networks of secondary phases are being developed for the following glass samples: LAWB45, LAWC22, H28-10A-2, and SRL-10A-S. In addition to these calculations, analyses have been performed using the LAWA44 glass sample discussed in Pierce et al. (2004a).

5.3.3 Phase II—Modeling

As of the date of this report, we have received glass composition and long-term PCT data compiled by Catholic University of America for a large quantity of glasses (over 250 samples). Of these, over 137 sample sets have PCT data for multiple days that are suitable for geochemical modeling to determine chemical reaction networks of secondary phases that form during the glass weathering. Input data files for geochemical modeling simulations have been constructed for all of these sample data sets, and the actual modeling has been initiated and is ongoing. To date, modeling has been performed on four samples. Figure 5.4 is an example of chemical reaction network of secondary phases determined by the modeling for A1-AN105R2 glass.

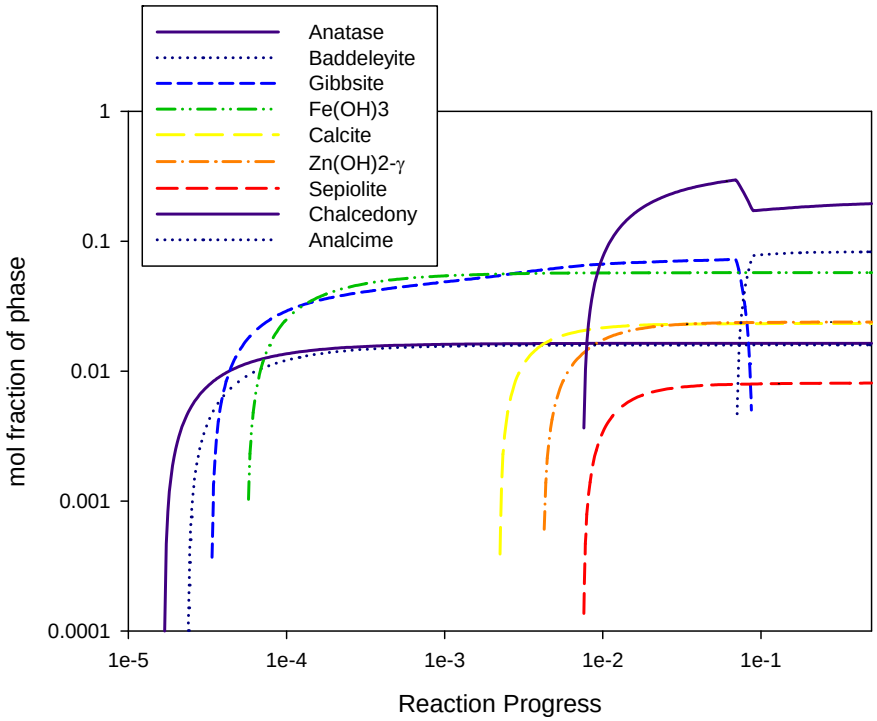

Figure 5.4. Predicted Paragenetic Sequence of Alteration Phases Formed During Reaction of A1-AN105R2 Glass in Deionized Water (DIW) in Equilibrium with Air

Model fits of the solution chemistry versus experimental data for the PCT test for A1-AN105R2 glass are shown in Figure 5.5. The model fits of the solution data are quite good and display the major attributes observed in the experimental data as a function of reaction progress.

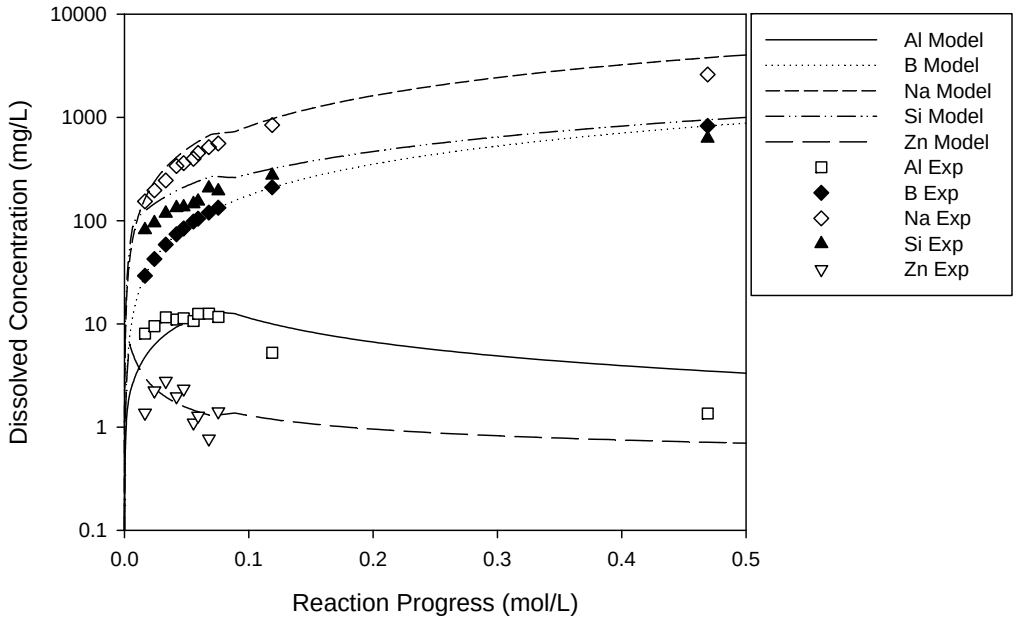

Figure 5.5. Solution Chemistry Model Fits Versus Experimental PCT Data for A1-AN105R2 Glass

The chemical reaction network of secondary phases determined for A1C1-1 glass by modeling is shown in Figure 5.6. The chemical reaction network of secondary phases determined for the A1C1-1 glass is very similar to that determined for the A1-AN105R2. This is not particularly surprising because both of these glasses have similar compositions of the major component oxides.

Model fits of the solution chemistry versus experimental data for the PCT test for the A1C1-1 glass is shown in Figure 5.7. Again, the model fits of the solution data are quite good and display the major attributes observed in the experimental data as a function of reaction progress.

Once model fits for all of the glass samples have been completed, variations in the chemical reaction network of secondary phases will be compared with variations in the oxide compositions of the various glasses. For example, Figure 5.8 shows a ternary diagram of glass compositions plotted with axes consisting of Al_2O_3/SiO_2, $(B_2O_3+Fe_2O_3)/SiO_2$, and $(Na_2O+Li_2O+K_2O)/SiO_2$. By comparing how the reaction network of secondary phases changes with the variations in these parameters, it may be possible to delineate over what compositional range of glasses that one can expect a particular suite of secondary phases to likely form.

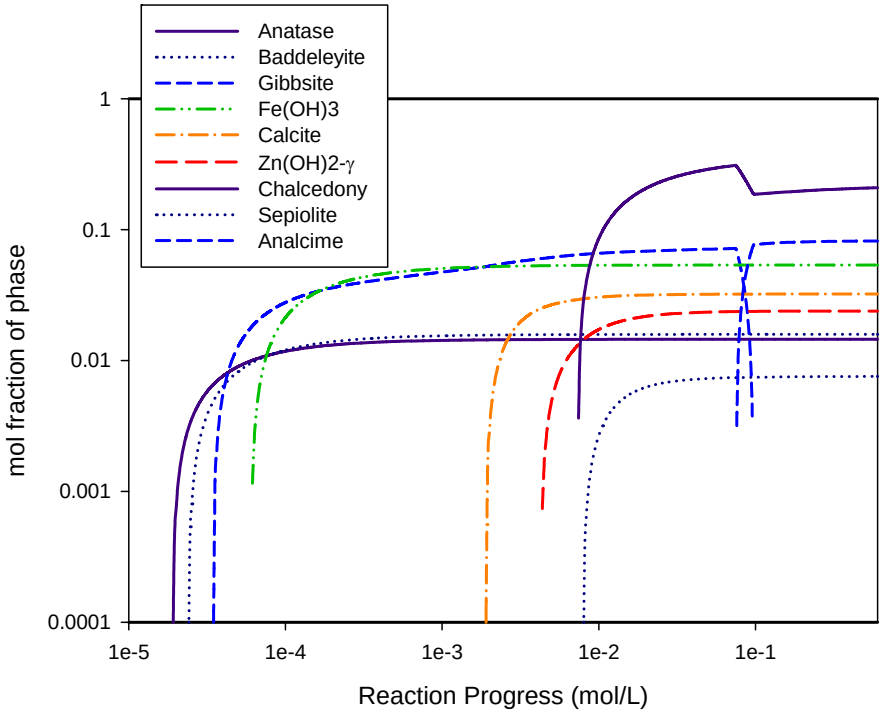

Figure 5.6. Predicted Paragenetic Sequence of Alteration Phases Formed During Reaction of A1C1-1 Glass in DIW in Equilibrium with Air

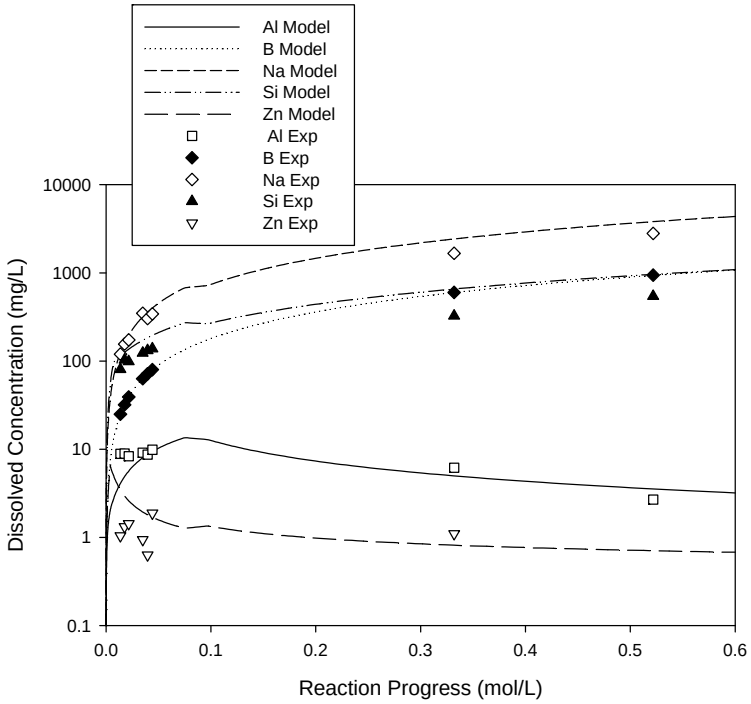

Figure 5.7. Solution Chemistry Model Fits Versus Experimental PCT Data for A1C1-1 Glass

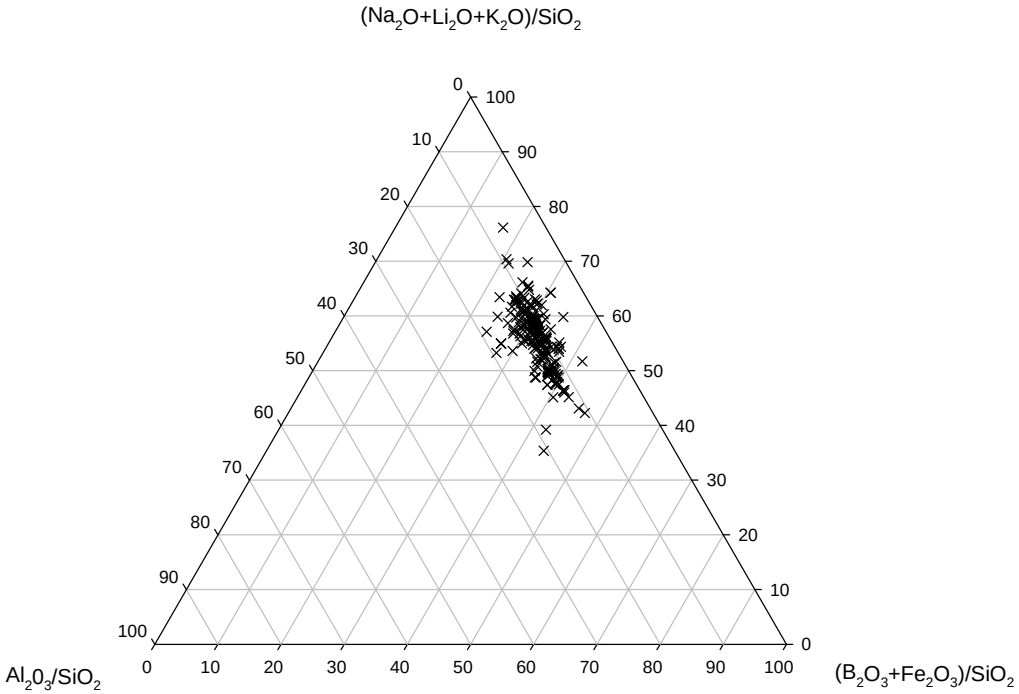

Figure 5.8. Ternary Diagram of 253 ILAW Glass Sample Compositions (Compiled by the Catholic University of America) Plotted with Axes Consisting of Al_2O_3/SiO_2, $(B_2O_3+Fe_2O_3)/SiO_2$, and $(Na_2O+Li_2O+K_2O)/SiO_2$

6.0 Monte Carlo Simulations

6.1 Overview

The primary objective of the MC simulations is to predict the composition, extent, and morphology of the hydration layer as a function of glass composition and thus provide input data for geochemical modeling of secondary phase formation. To achieve this objective, the MC work will be divided into three tasks: model development, model parameterization, and data production. The three tasks will initially be undertaken linearly, although the introduction of new glass components in the out-years could require us to carry out further model development and parameterization. In what follows, the three tasks are described in further detail:

The MC simulations will use as input structural data obtained from NMR and Raman measurements performed under this project. The experimental structural data will allow us to determine the coordination environment and speciation of the different glass components. It is therefore imperative that the simple preliminary model described in the previous section be extended to include a range of improved structural features to accommodate all eventual experimental structural findings. These features include the following:

- Nuclear waste glasses often consist of more than 20 elements. Therefore, the MC program will be upgraded to be able to treat any number of glass components.
- Each cation in the glass forms *n* bonds with oxygen atoms and is said to be in *n*-fold coordination. Boron atoms can be found in both threefold and fourfold coordinations, and silicon and aluminum atoms are generally fourfold coordinated whereas iron and zirconium atoms are present in six-fold coordination. Therefore, the MC program will be modified to model the entire range of observed coordination environments for the major glass components. In addition, non-bridging oxygens are important species that break the connectivity of the glass-former network and will therefore also be included in the MC program.
- The glass species do not adopt a fully random distribution. For example, aluminosilicate glasses are known to follow the aluminum avoidance rule. Also, boron atoms often distribute themselves between ring and non-ring environments. Therefore, the MC program will be amended to account for the structure speciation of the glass components.

The MC simulations use three main types of input data: glass composition, glass structure, and the reactivity of glass components (i.e., hydrolysis and condensation rate constants). As already mentioned, the glass composition and glass structure will be determined from NMR, Raman, and other experimental characterization studies performed under this project. In previous MC studies of glass dissolution (e.g., Aertsens and Van Iseghem 1996, Devreux et al. 2001), reactivity parameters for Si-O-Si linkages were set to reproduce experimentally derived bond strengths or silica equilibrium solubility. In the rare case where other partially soluble species were considered (Devreux et al. 2001), their reactivity parameters were set arbitrarily to yield a dissolution rate that was faster than that of Si. Although such an approach is adequate for a qualitative simulation of glass dissolution when a limited number of components are present, a more sophisticated parameterization approach is required to accurately reproduce the relative dissolution rates of the many components that compose nuclear waste glasses. A quantitative description of the long-term dissolution kinetics (i.e., on the timescale of months and years) of nuclear waste glasses using MC simulations is beyond the scope of this project because such a timescale is not obtainable with the current algorithm within the lifetime a single project; however, the characteristics of the hydration layer are expected to be sensitive to the relative dissolution rates of the glass components. Therefore, an

accurate description of the relative dissolution rates of the glass components is crucial to the success of this task.

For the purposes of our model parameterization effort, the glass components are divided into three groups based on their mass percentage in typical prospective low activity waste glasses, namely, major components (10% and above), minor components (between 1 and 10%), and trace components (below 1%). The major component group consists of Si, Al, B, and Na. Typical minor components are Li, K, Mg, Ca, Ti, Fe, Zn, and Zr. Finally, trace components include Cl, F, Ni, Pb, and Ce amongst others. Many dissolution studies have been carried out with glasses, and these compositions were restricted to the major components (Cailleteau et al. 2008a, Jegou et al. 2000, Ledieu et al. 2006 Ledieu et al. 2004a, 2004b). In particular, some studies have investigated the effects of substituting one major component by another on the dissolution kinetics (Icenhower et al. 2008, Pierce et al. 2010). Both sets of studies will provide us with three types of data for deriving the reactivity parameters (i.e., the hydrolysis and condensation rate constants):

1. Kinetics of dissolution
2. Composition of the leached layer
3. Composition of the leached fraction.

The reactivity parameters will be optimized to maximize the agreement between the calculated and experimental data for the three types of data listed above. Published work on the dissolution of glasses containing either one or two minor components in addition to several major components will be employed to isolate the effects of the different minor components on the kinetics of dissolution (e.g., Zr [Cailleteau et al. 2008b, Lobanova et al. 2001]; Ca [Arab et al. 2008, Devreux et al. 2010, Jollivet et al. 2008]; and Ti [Leturcq et al. 1999]). If time allows, the derivation of reactivity parameters for a series of trace components will be undertaken in the last year of the project once the MC model has been shown to give an accurate description of the dissolution of nuclear waste glasses that consist of major and minor components only.

It should be noted that supporting information to help determine the relative dissolution rates of the different glass components can be obtained from gathering data on the dissolution kinetics of the corresponding single (hydr)oxides. Indeed, the work of Oelkers (2001) and Casey (1991) strongly suggests that there exists a correlation between the relative rates of metal-oxide bond breaking in single- and multi-oxides.

Initially, test simulations will be run after each new structural feature is implemented to investigate its effects on dissolution kinetics and hydration layer characteristics. This step-by-step approach will enable us to isolate and determine the role of known structural features of nuclear waste glasses, thereby contributing to our general understanding of glass dissolution chemistry. This will allow us to remove any unnecessary program features and establish the standards for atomic-level simulations of glass dissolution. After the necessary model development and parameterization steps have been taken, a series of MC simulations will be carried out to investigate the steady-state characteristics of the hydration layer for a range of glass compositions. The data of interest computed in the MC simulations include:

1. Composition of hydration layer (i.e., mole fractions of Si, Al, B, Na, etc)
2. Thickness of hydration layer
3. Morphology/porosity of hydration layer (fraction of solution sites within the hydration layer).

The MC algorithm involves bookkeeping of the nature of each site, which enables a direct and straightforward computation of each of the three characteristics listed above. Three sets of glass compositions will be considered: 1) glasses that consist of major components only; 2) glasses that consist of major components and one minor component; and 3) glasses that consist of major components and

several minor components. For each set, the initial mole fractions of each component will be varied. If time allows, similar calculations with glasses that also include trace components will be carried out in the last year of the project. The MC simulations will be performed on local workstations. Next, we discuss the methods and results obtained from an initial set of calculations completed in FY2010 using a series of four component glasses that contain Al, B, Na, and Si, the four main components of ILAW glass.

6.2 Computational Methods

A MC computer program was designed and implemented to model glass dissolution. The MC program is based on the glass dissolution model of Devreux, Barboux, and co-workers (Devreux et al. 2001, Devreux et al. 2004, Ledieu et al. 2006, Lobanova et al. 2001). In the MC model, the glass framework is mapped onto a cubic array, which allows for high computing efficiency. Each lattice site represents a glass-former cation (e.g., Si, Al, and B) and its first oxygen coordination shell. Glass-modifier cations (e.g., Na) are placed in interstitial positions. Connections (also referred to as bonds) between nearest-neighbor sites represent X-O-X linkages, where X is a glass-former cation. To represent the fourfold connectivity of the glass-former cations (e.g., Si, Al, and B), two connections (bonds) were removed at each lattice site. Special cases arise for silicon sites with a non-bridging oxygen (NBO) and for trigonal boron atoms, as described in detail below. In all simulations, the initial configuration of the glass was that of a slab with a perfectly smooth surface. The glass slab had a surface area of 32×32 lattice sites and a depth of 1024 lattice sites. The volume of the contacting aqueous solution was considered to be infinite to mimic the conditions in an SPFT experiment conducted under dilute conditions, and therefore none of the species were allowed to condense at the glass-water interface. Finally, overhangs are permitted in the glass dissolution model, and therefore a cluster of lattice sites will dissolve when it finds itself unconnected to the main glass slab. As explained by Devreux et al. (2001), the glass connectivity needs to be computed to account for this process, and therefore the cluster labeling algorithm of Hoshen and Kopelman (1976) was implemented in the MC program.

Four elements were considered in this work, namely, silicon, boron, aluminum, and sodium. Silicon atoms are in tetrahedral coordination ($SiO_{4/2}$) and therefore form four bonds with nearest-neighbor sites. If associated with a non-bridging oxygen, a silicon site is considered to form only three bonds with nearest-neighbor sites and is charge compensated by a sodium ion $SiO^-_{5/2}$. Boron atoms can be found in both tetrahedral $BO^-_{4/2}$ and trigonal $BO_{3/2}$ coordination environments, thus forming four and three bonds with nearest-neighbor sites, respectively. The $BO^-_{4/2}$ units are charge compensated by sodium ions. Additionally, three $BO_{3/2}$ units can form a boroxol ring. In the MC algorithm, a boroxol ring is generated by inserting a trigonal boron at random in the glass network and additional trigonal boron atoms at two of the four possible nearest-neighbor positions. Boroxol rings can also polymerize. In the MC model, the extent of polymerization is fixed by setting the boroxol rings cluster size, nbr, which is an input parameter. A lattice site that can accommodate a boroxol ring is selected at random, and then a nearest-neighbor site that can accommodate an additional boroxol ring is also selected at random and so on until nbr continuous boroxol rings have been inserted. Aluminum atoms are always found in tetrahedral coordination $AlO^-_{4/2}$, are charge compensated by sodium, and cannot be associated with a non-bridging oxygen. Sodium atoms are either used to charge compensate $BO^-_{4/2}$ and $AlO^-_{4/2}$ units or used to induce the formation of non-bridging oxygens. In the MC algorithm, a silicon site and one of its silicon nearest-neighbor sites are selected at random, and then the connection between them is broken. Each site is assigned a non-bridging oxygen and is charge compensated by a sodium ion.

The MC algorithm proceeds as follows. Once the initial glass structure has been generated, the program enters a loop that it exits only when the glass has been completely dissolved, or a set number of simulation steps has been reached. Each simulation step comprises the following three stages: 1) a dissolution evaluation and execution stage, in which each surface site is evaluated for dissolution using dissolution probabilities determined as described in detail below; 2) a connectivity evaluation stage, in which the new glass configuration is evaluated to determine whether clusters of lattice sites not connected to the main glass slab are present and therefore should also be dissolved; and 3) a coordination evaluation stage, in which the coordination of each site in the final glass configuration is re-calculated.

Boron atoms are considered to dissolve instantaneously once in contact with the aqueous solution (i.e., B-O-Si and B-O-Al linkages are assumed to have zero strength), and therefore, their dissolution probability is set to 1 regardless of their coordination. Silicon sites, however, have a probability for dissolution dependent on their coordination. Probabilities w_1, w_2, and w_3 are used for sites with one, two, or three bonds to nearest neighbors. Only Si-O-Si and Si-O-Al linkages are considered when determining the number of nearest neighbors because the strength of Si-O-B linkages is assumed to be zero. The MC program also includes aluminum, and therefore Si and Al can find themselves in a number of possible bonding environments. To minimize the number of reactivity parameters used to describe all possible bonding environments, we employ the formulation introduced by Ledieu et al. (2006), which defines the Si and Al dissolution probabilities as follows:

$$w_d(Si,n,m) = \frac{w_n}{r^m} \tag{1}$$

and

$$w_d(Al,n,m) = \frac{w_n}{r^{m+1}} \tag{2}$$

where w_d = dissolution probability for Si or Al
n = total number of bonds
m = number of bonds with Al
r = relative bond strength between Si-O-Si and Si-O-Al linkages.

Therefore, four parameters, namely, w_1, w_2, w_3, and r, are required to generate all possible dissolution probabilities.

Finally, we include a note on the nomenclature used in this work. Silicon sites in the bulk of the glass with four and three bonds to nearest-neighbor sites will be referred to as Q^4 and Q^3 sites, respectively. Similarly, silicon sites at the glass-water interface with one, two, and three bonds to nearest-neighbor sites will be referred to as S^1, S^2, and S^3 sites, respectively.

6.2.1 Results and Discussion

6.2.1.1 Effect of Boron Content on the Dissolution of Sodium Borosilicate Glasses

In this section, we investigate the effects of varying the boron content on the rate and mechanism of dissolution of sodium borosilicate glasses. In the glass series evaluated in this section, all boron atoms are considered to be in tetrahedral coordination and are charge compensated by sodium ions. Therefore, the Na_2O and B_2O_3 mole fractions are set to be equal. The B_2O_3 mole fraction was varied from approximately 0.05 to 0.30, which corresponds to Si/B ratios from 8.0 to 0.7. The probabilities w_1, w_2, and w_3 were also varied to evaluate to what extent they influence the dissolution behavior as a function of boron content. For all sets of probabilities used in this section, the ratios w_1/w_2 and w_2/w_3 were set to be equal to δ, following the notation of Devreux et al. (2004). The probability set w_1=0.1, δ =10 was used as the reference set (referred to as P1). Two probability sets were generated by setting δ to 2 and 100 while keeping w_1 equal to 0.1 (P2 and P3, respectively), and two more probability sets were determined by setting w_1 to 0.5 and 0.02 while keeping δ equal to 10 (P4 and P5, respectively). In all cases, dissolution was calculated to be congruent; therefore, identical results would be obtained for dissolution rates based on silicon release or boron release to solution. The rate of dissolution for composition x, R_x, was calculated by normalizing the rate of silicon release by the fraction of silicon in the lattice and the initial surface area and therefore corresponds to the number of stoichiometric units dissolved per unit area and per simulation step.

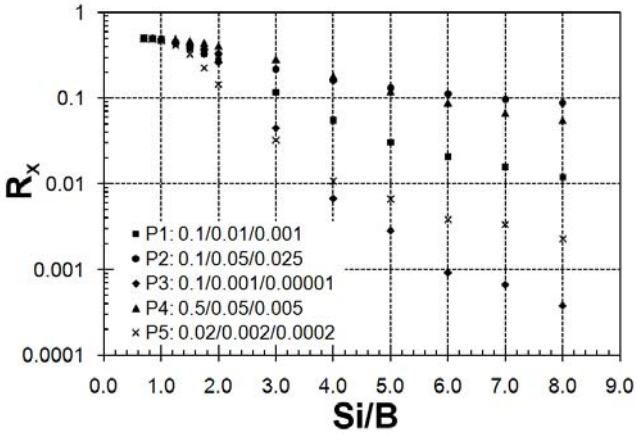

Figure 6.1. Glass Dissolution Rate (R_x) in Stoichiometric Unit Per Unit Area and Per Simulation Step as a Function of the Si/B Ratio for a Series of Silicon Dissolution Probability Sets

Figure 6.1 shows that, at the lowest Si/B ratios (1.25 and below), the dissolution rate is independent of the silicon dissolution probabilities, as previously demonstrated by Devreux et al. (2004). As explained by Devreux et al., at these boron contents, the boron percolation threshold has been reached, and the rate of dissolution is controlled by the dissolution rate of boron, which is instantaneous in the MC model. At the highest Si/B ratios (7.0 and above), the dependence on the boron content, although still observable, diminishes greatly. In between these two regimes, the dissolution rate is dependent on the boron content with greater sensitivity for the sets with low dissolution probabilities.

It is interesting to note that, when comparing the results obtained with the sets P2 and P4, there is a crossover between Si/B values of 4.0 and 5.0. Both sets have the same value of w_2, but w_1 is higher for P4, and w_3 is higher for P2. Similarly, there is a crossover between P3 and P5, which have similar w_2 probabilities but different values of w_1 and w_3. These crossovers result in the rates of dissolution being ordered according to w_3 at high Si/B ratios, to w_1 at low Si/B ratios, and to w_2 at intermediate Si/B ratios. Therefore, the simulation results indicate that the rate of dissolution is controlled by w_3, w_2, and w_1 at high, intermediate, and low Si/B ratios, respectively.

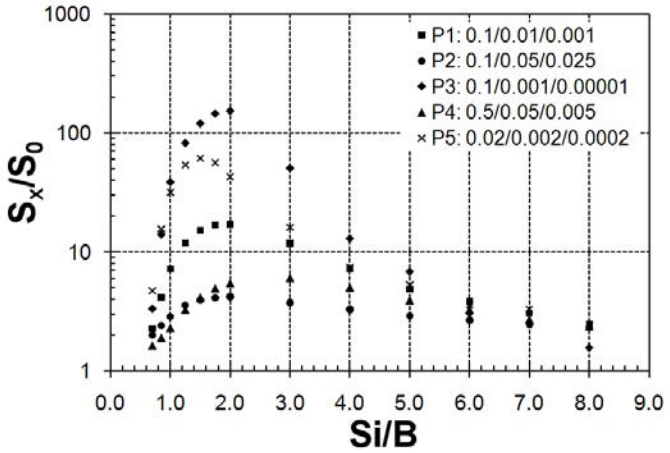

Figure 6.2. Hydration Layer Surface Area (S_x) Relative to Initial Surface Area (S_0) as a Function of the Si/B Ratio for a Series of Silicon Dissolution Probability Sets

Figure 6.2 shows the hydration layer surface area, S_x, normalized to the initial surface area, S_0, as a function of the Si/B ratio for the same five probability sets. The surface area is calculated at the start of every simulation step by summing the number of broken bonds at the glass-water interface. For example, a surface silicon site with three bonds to nearest-neighbor sites contributes one area unit to the surface area, thus accounting for the fact that one face of the SiO_4 tetrahedron is exposed to the aqueous solution. For all five sets, the surface area increases with increasing silicon content, reaches a maximum, and then decreases to almost 1. A similar plot of the hydration layer thickness (calculated as the difference between the topmost occupied layer and the topmost complete layer) as a function of the Si/B ratio displays the same behavior as shown in Figure 6.2 (data not shown), which indicates that surface area and thickness can be used interchangeably when discussing these glasses. At the silicon-poor end, boron is controlling the dissolution and, since its dissolution is instantaneous in the MC model, the glass is dissolving via a fast layer-by-layer mechanism, which is reflected by the normalized surface area converging to 1. As the silicon content increases, continuous networks of silicon sites start to develop and allow for the hydration layer to become progressively thicker. A larger thickness signifies a higher surface area, which, in turn, translates into a greater dissolution rate. As the silicon content increases further, S^2 and S^3 sites begin to dominate the composition of the hydration layer. In this regime, the gradual decrease in boron content prevents the aqueous solution from penetrating into the glass without having to dissolve silicon sites. In addition, S^1 and S^2 sites are preferentially removed before the dissolution front can advance by dissolving an S^3 site. This leads to the gradual decrease of the hydration layer thickness and surface area as this mechanism becomes more prominent. Finally, it should be noted that Figure 6.2 indicates that the lower the dissolution probabilities, the more pronounced the effect of the

Si/B ratio on the surface area is. Moreover, the position of the peak maximum is also found to be dependent on the silicon dissolution probabilities.

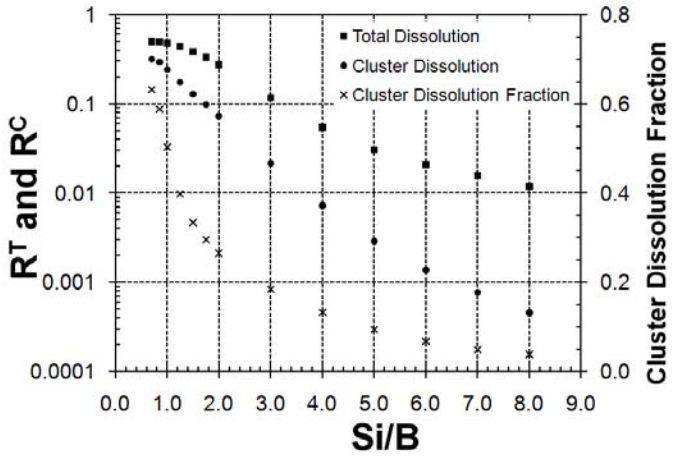

Figure 6.3. Total Dissolution Rate (R_x^T) and the Dissolution Rate Due to Detachment of Clusters (R_x^C) as a Function of the Si/B Ratio. Both rates are based on silicon release and are in stoichiometric unit per unit area and per simulation step. Also shown is the proportion of the total dissolution rate due to dissolution via detachment of clusters.

An important phenomenon that contributes to the dissolution rate is the dissolution of the glass via detachment of clusters, which takes place in the second of the three stages of the MC algorithm, as described in the Computational Methods section. Figure 6.3 shows the contribution of this mechanism to the total dissolution rate as a function of the Si/B ratio. The rate of dissolution due to the detachment of clusters increases greatly as the boron content increases. As the Si/B ratio decreases, the probability for the formation of continuous networks of boron atoms increases. As dissolution proceeds, such networks can lead to the formation of clusters that are not connected to the main solid and hence dissolve in one piece. Therefore, the amount of glass components dissolved via detachment of clusters from the surface increases with increasing boron content. This leads to a decrease of the hydration layer thickness and surface area as the dissolution via detachment of clusters plays a progressively more important role.

6.2.1.2 Effect on Non-Bridging Oxygens on the Dissolution of Sodium Borosilicate Glasses

In this section, simulations were performed to investigate the effects of varying the amount of non-bridging oxygens in sodium borosilicate glasses by adding sodium. Several series of glasses were investigated with Si/B ratios varying from 1.25 to 3.00. In each series, the mole fraction of sodium was increased while keeping the Si/B ratio constant. Five values of the fraction of silicon sites with a non-bridging oxygen (denoted as fQ^3) were used: 0.000, 0.085, 0.175, 0.270, and 0.370. These values were chosen to cover the range of values observed for the NeB glasses by Pierce et al. (2010). All boron atoms were in tetrahedral coordination and were charge compensated by sodium ions. The remaining free sodium ions break the connectivity of the glass-former network. Two sodium ions were used to break a Si-O-Si linkage and thus introduce two non-bridging oxygens. Each silicon site was associated with no more than one non-bridging oxygen. The reference probability set (w_1=0.1, δ=10) was used in this section.

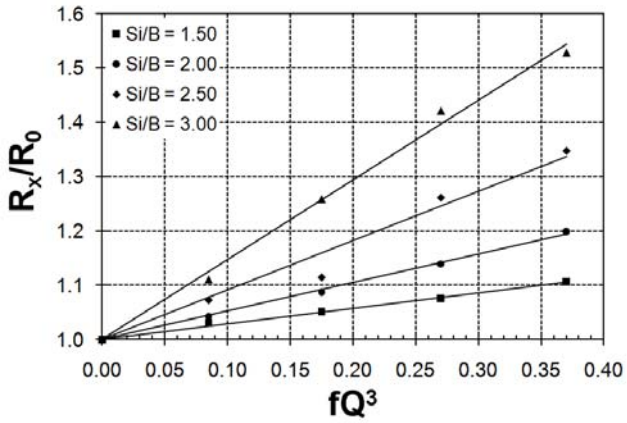

Figure 6.4. Glass Dissolution Rate (R_x) Relative to that with no NBOs (R_0) as a Function of the Fraction of Silicon Sites with an NBO (fQ^3) for a Range of Si/B Ratios

Using four example compositions, Figure 6.4 shows that an increasing amount of NBOs leads to an increase in dissolution rate at all Si/B ratios and that this increase is linearly dependent on the fraction of silicon sites with an NBO. However, as shown in Figure 6.5, the extent of this accelerating effect is dependent on the Si/B ratio. Notably, there appears to be two different dissolution regimes, namely, above and below Si/B = 2.00. To understand the origin of this phenomenon, we first note that in Figure 6.2, which shows the hydration layer surface area as a function of the Si/B ratio for compositions without NBOs, S_x/S_0 reaches a maximum at Si/B = 2.00 for the probability set used in this section. This was interpreted as the composition at which the contribution of the dissolution via detachment of clusters diminishes sufficiently that the glass dissolution becomes controlled by the silicon dissolution probabilities w_2 and w_3. This change in controlling mechanism influences the effect of NBOs on the glass dissolution rate. NBOs break the connectivity of the glass network, making the dissolution of individual blocks more facile. This effect is similar to that of isolated boron atoms since, again, Si-O-B linkages are considered as having zero strength. However, unlike boron atoms, NBOs do not affect significantly the extent of dissolution via detachment of clusters, as illustrated in Figure 6.6. Therefore, their effect is felt more strongly when dissolution via detachment of clusters is not a dominant process, i.e., at high Si/B ratios. This explains the change in gradient shown in Figure 6.5, whereby, below Si/B = 2.00, dissolution via detachment of clusters becomes a dominant process, and thus the effect of NBOs diminishes, which translates into a gentler gradient.

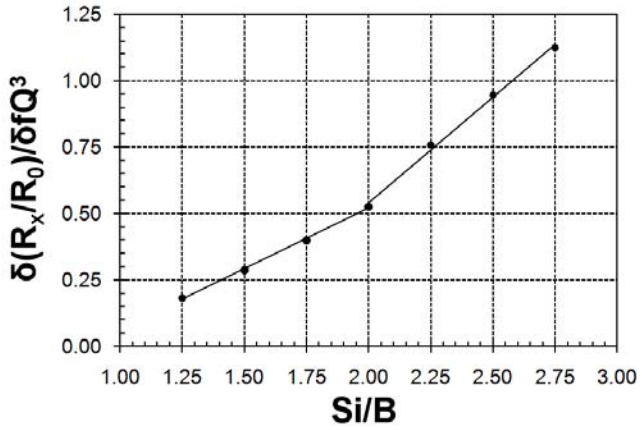

Figure 6.5. Gradient of the Relative Glass Dissolution Rate with Respect to the Fraction of Silicon Sites with an NBO ($\delta(R_x/R_0)/\delta fQ^3$) as a Function of the Si/B Ratio

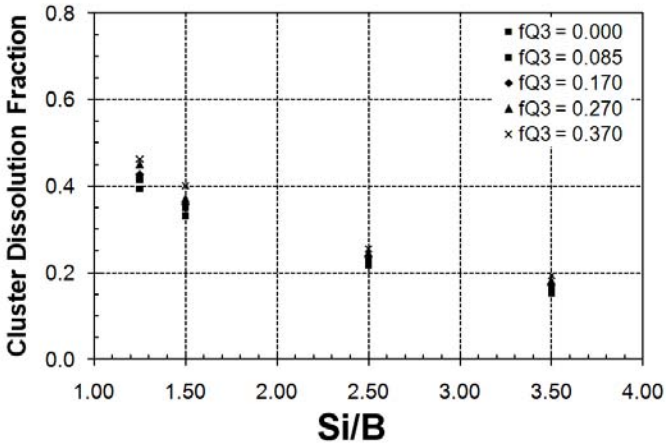

Figure 6.6. Fraction of the Dissolution Rate Due to Detachment of Clusters as a Function of the Si/B Ratio for Different Fractions of Silicon Sites with a Non-Bridging Oxygen (fQ^3)

6.2.1.3 Effect of Boroxol Ring Formation and Polymerization on the Dissolution of Sodium Borosilicates

As mentioned above, an important structural characteristic of borosilicate glasses is the partition of boron between trigonal $\left(BO_{3/2}\right)$ and tetrahedral $\left(BO_{4/2}^{-}\right)$ coordination environments. In addition, three $\left(BO_{3/2}\right)$ groups can link to form a boroxol ring. Moreover, it has been reported that boroxol rings can polymerize within the glass network (Du and Stebbins 2003). Therefore, in this section, we determine the effect of boroxol ring formation and polymerization on the dissolution rate and mechanism of sodium borosilicate glasses. The reference probability set (w_1=0.1, δ=10) was used in all calculations presented in this section.

First, we carried out two MC simulations for a series of Si/B ratios. In the first simulation, all boron atoms are in tetrahedral coordination and are charge compensated by sodium ions. In the second simulation, the same number of boron atoms is used; however, all boron atoms are now in trigonal

coordination, and each boron atom is part of a boroxol ring. Boroxol rings are distributed randomly in the glass network. Figure 6.7 shows the dissolution rate of silicon, normalized to the fraction of silicon sites in the lattice, per the simulation step as a function of the Si/B ratio for both series of MC simulations. Figure 6.7 indicates that the presence of boroxol rings increases the rate of dissolution of the borosilicate glasses at all boron contents. However, the extent of this accelerating process is dependent on the Si/B ratio. At the lowest Si/B ratios, the effect is weak to negligible because the glass dissolution is controlled by boron dissolution. As the Si/B ratio increases, the rate increase becomes greater. The origin of this phenomenon is similar to that described above for the effect of NBOs on glass dissolution, whereby the grouping of boron atoms in boroxol rings decreases the likelihood for the formation of continuous networks of boron atoms and thus reduces the extent of dissolution via detachment of clusters. Conversely, the presence of boroxol rings increases the likelihood for the formation of continuous networks of silicon atoms, thereby increasing the capability of the glass to develop a thick hydration layer. Both effects give rise to a thicker hydration layer, which translates into a higher surface area and therefore a faster dissolution rate. At high Si/B ratios, the dissolution is controlled by the dissolution of S^2 and S^3 sites, and the boron content becomes too low to have a pronounced effect. The R($^{[3]}$B)/R($^{[4]}$B) ratio diminishes as a result.

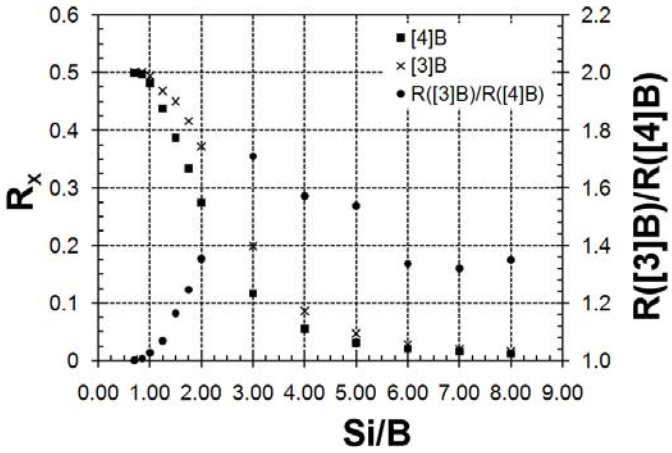

Figure 6.7. Glass Dissolution Rate (R_x) in Stoichiometric Unit Per Unit Area and Per Simulation Step as a Function of the Si/B Ratio for a Random Distribution of Tetrehedral Boron Atoms ($^{[4]}$B) and for a Random Distribution of Boroxol Rings ($^{[3]}$B). This is also shown in the ratio of the two rates as a function of Si/B.

We now investigate to what extent the formation of polymers (or clusters) of boroxol rings affects the rates and mechanisms of dissolution of borosilicate glasses. A series of MC simulations was carried out for values of n_{br} ranging from 2 to 25 with borosilicate glasses with a range of Si/B ratios. Figure 6.8 shows the rate of silicon dissolution relative to the rate for isolated boroxol rings as a function of the Si/B ratio for five values of n_{br}. Overall, the rate of dissolution is seen to increase with increasing n_{br}. Similar to the mechanism discussed previously, the increase in boron polymerization increases the likelihood for the formation of continuous networks of silicon atoms, which allows for a thicker hydration layer to develop, which, in turn, translates into a higher surface area and thus into a faster dissolution rate. However, at the silicon-poor end, the extent of the rate increase diminishes as Si/B decreases to the extent that it becomes insignificant at the lowest Si/B ratios. In this regime, the boron content is high enough to be little affected by the extent of polymerization. Indeed, as Si/B is reduced, the likelihood for the clusters of boroxol rings to become adjacent increases. At the silicon-rich end, the extent of the rate

increase also decreases. In this regime, as explained above, the dissolution is controlled by the dissolution of S^2 and S^3 sites and, therefore, boron atoms, and by extension boroxol rings and clusters of rings, do not play a significant role.

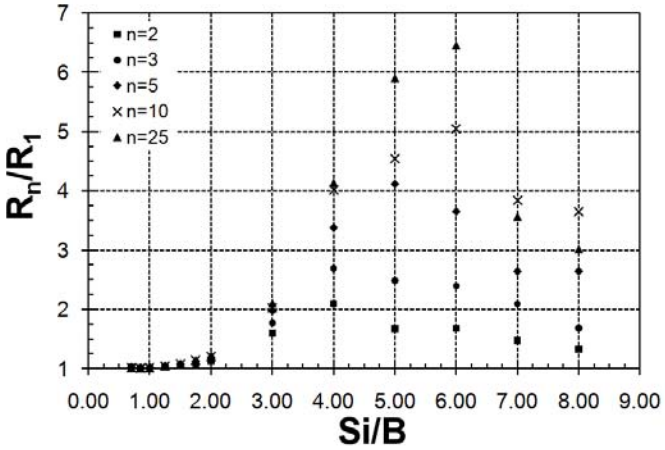

Figure 6.8. Glass Dissolution Rate for Boroxol Rings Clusters of Size *n* (R_n) Relative to the Rate for Isolated Boroxol Rings (R_1) as a Function of the Si/B Ratio for Different Values of *n*

6.2.1.4 Effect of Aluminum Content and Aluminum Avoidance Rule on the Dissolution of Sodium Aluminoborosilicates

Having studied in detail the dissolution rates and mechanisms of three-component glasses, we will now increase the level of complexity by focusing on four-component glasses. Aluminum will be considered as the fourth component as it is the fourth component present in the NeB glass series. One important characteristic of aluminum-containing glasses is the aluminum avoidance rule, which says that Al-O-Al linkages between tetrahedra are unstable. Therefore, we initiate our study of aluminum-containing glasses by evaluating the effects of including the aluminum avoidance rule on the rates and mechanisms of glass dissolution.

In this section, the value of *r* is varied to investigate the effects of making the Si-O-Al linkage stronger or weaker than the Si-O-Si linkage. This approach has the advantage of enabling us to draw conclusions that are more general than if we had selected a particular value of *r*, and thus we expect our findings to likely be applicable to other glass components. We performed a series of MC simulations with aluminosilicate glasses with silicon-to-aluminum (Si/Al) ratios of 3:1 and 2:1. There is no boron present in these glasses. All aluminum atoms are in fourfold coordination and charge compensated by sodium ions; the Al_2O_3 and Na_2O mole fractions are therefore set to be equal in these glasses. For each composition, we ran simulations with seven values of *r*: 0.03, 0.1, 0.3, 1, 3, 10, and 30. The reference probability set (w_1=0.1, δ=10) was employed in this section.

For *r* values lower than 1, we observed that following the avoidance rule reduces the dissolution rate, as shown in Figure 6.9. This phenomenon stems from the fact that enforcing the avoidance rule modifies the hydration layer thickness, and thus its surface area, and that the larger the surface area, the higher the dissolution rate (Figure 6.10). Indeed, when the distribution of Al and Si atoms in the glass network is purely random, clustering of Al may occur, which increases the likelihood for continuous networks of silicon sites. As a result, a thick hydration layer can develop, leading to a large surface area and thus a

high dissolution rate. When the avoidance rule is enforced, however, the hydration layer is weakened by reducing the probability for occurrence of continuous networks of silicon sites. This yields a thinner hydration layer than in the purely random case and thus a lower dissolution rate.

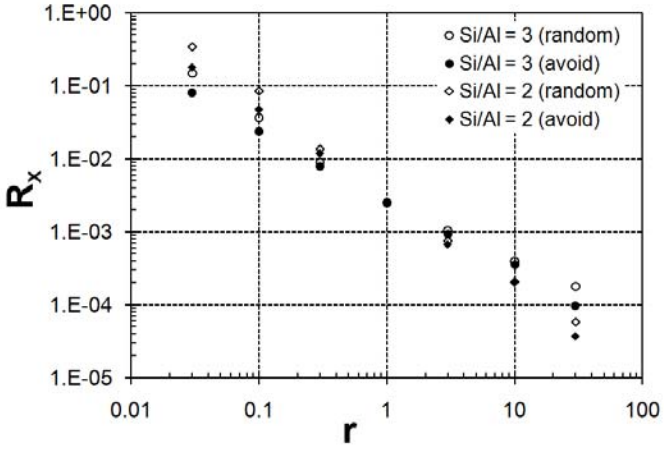

Figure 6.9. Glass Dissolution Rate (R_x) in Stoichiometric Unit Per Unit Area and Per Simulation Step as a Function of the Parameter *r* for Two Si/Al Ratios, with and Without the Aluminum Avoidance Rule

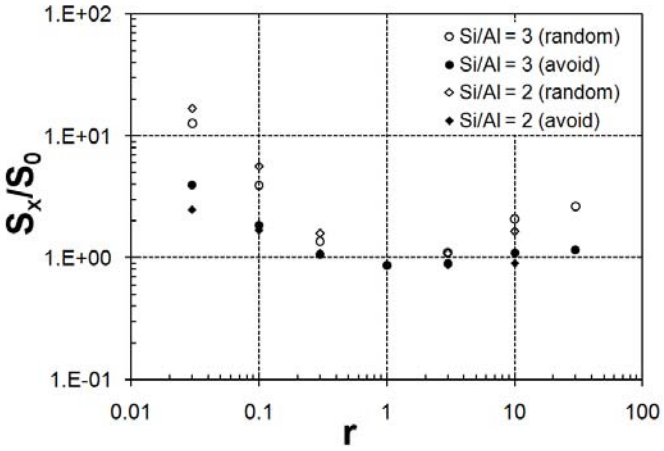

Figure 6.10. Hydration Layer Surface Area (S_x) Relative to Initial Surface Area (S_0) as a Function of the Parameter *r* for Two Si/Al Ratios with and Without the Aluminum Avoidance Rule

For values of *r* higher than 1, we also observe that implementing the aluminum avoidance rule yields a lower dissolution rate (Figure 6.9). As before, when the distribution of Al and Si atoms in the glass network is purely random, Al-O-Al linkages can occur. These linkages are particularly difficult to dissolve, which creates areas of low reactivity. This, in turn, leads to thick hydration layers, large surface areas, and thus overall high dissolution rates. However, when the avoidance rule is followed, Al-O-Al linkages are absent in the glass network. Al ions are therefore isolated and are thus more easily dissolved. This causes the thickness of the hydration layer to shrink, the surface area to lower, and hence the dissolution rate to decrease.

To summarize this section, our results indicate that implementing the aluminum avoidance rule does affect the rate of dissolution of sodium aluminosilicate glasses and that the dissolution rate decreases for all values of *r* different from 1.

6.2.1.5 Dissolution of the Sodium Aluminoborosilicate Glasses Series NeB

In this section, we model the dissolution of the glasses used in the study of Pierce et al. (2010) on the effect of the B/Al ratio on glass dissolution to identify the mechanisms that controlled the dissolution of these glasses. A summary of the compositional and structural characteristics of the glasses, determined experimentally by Pierce and co-workers and used as input parameters in the MC simulation, is presented in Table 6.1. The structural features of the NeB glasses (aluminum, trigonal boron, and non-bridging oxygens) have been studied separately in the previous sections. Therefore, insights gained in previous sections will enable us to interpret the dissolution behavior of the NeB glass series. The aluminum avoidance rule was employed in all five glasses. However, for the glasses with the highest aluminum contents, NeB0 and NeB1, the fraction of aluminum sites in the lattice was too high to enforce a strict aluminum avoidance rule for every single site given that the approach for incorporating aluminum is to use random insertion with conditions. Therefore, for each aluminum site to be placed, the aluminum avoidance rule was relaxed if a suitable site could not be found after 100,000 trials. The reference probability set (w_1=0.1, δ=10) was employed in this section.

Table 6.1. Chemical Compositions of NeB Glasses and Corresponding MC Input Parameters

Glass ID	NeB0	NeB1	NeB2	NeB3	NeB4
Composition (mole fractions)					
SiO_2	0.50	0.50	0.50	0.50	0.50
B_2O_3	0.00	0.05	0.10	0.15	0.20
Al_2O_3	0.25	0.20	0.15	0.10	0.05
Na_2O	0.25	0.25	0.25	0.25	0.25
$^{[4]}B/B_T$	-	0.127	0.397	0.551	0.622
MC Input Parameters					
Si^a	0.50	0.50	0.50	0.50	0.50
$B_T{}^a$	0.00	0.10	0.20	0.30	0.40
Al^a	0.50	0.40	0.30	0.20	0.10
$^{[3]}B^b$	-	0.873	0.603	0.449	0.378
Q^{3c}	0.000	0.175	0.241	0.269	0.302

Figure 6.11 shows the Si dissolution rates calculated for the five glasses for different values of the parameter *r*, which is the relative bond strength between Si-O-Si and Si-O-Al linkages. As seen previously, an increase in the strength of the Si-O-Al linkage relative to that of Si-O-Si results in a decrease of the dissolution rate. This effect is obviously more pronounced when the proportion of Al is greater, i.e., at low B/Al ratios. In addition, the lower the *r* parameter, the smaller the effect of the B/Al ratio. This is expected because an infinitely small *r* parameter would correspond to the Si-O-Al linkage being as weak as the Si-O-B linkage, which is assumed to have no strength in the MC model. Interestingly, Figure 6.11 shows that the effect of *r* is small below *r*=0.10, indicating that, below a cutoff

value, the strength of the Si-O-Al linkage does not significantly affect the overall dissolution rate. Comparison with the corresponding experimental results shown in Figure 16 of Pierce et al. (2010) suggests that *r* should have a value of 0.10 or below because the experimental dissolution rates based on Si were found to be largely independent of the B/Al ratio. In the formulation of Ledieu et al. (2006), which is used in the current MC algorithm, a value of r=0.1 means that an Al site attached to the glass network by n Al-O-Si linkages is 10 times more likely to dissolve than a Si site with n Si-O-Si linkages (where n=1, 2, or 3).

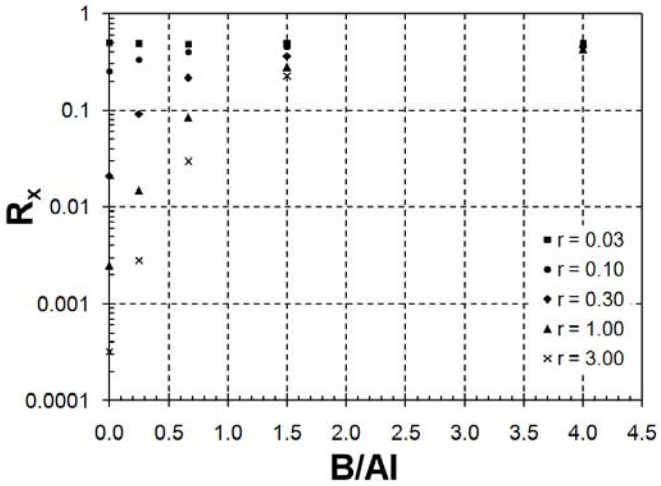

Figure 6.11. Glass Dissolution Rate (R_x) in Stoichiometric Unit Per Unit Area and Per Simulation Step as a Function of the B/Al Ratio for a Series of Si-O-Si/Si-O-Al Relative Linkage Strengths (r)

A value of *r* of 0.10 or below is consistent with the fact that the Al-O-Si linkage has been reported in the literature as being weaker than the Si-O-Si linkage. Indeed, in their *ab initio* quantum mechanical study, Xia and Lasaga (1994) calculated an activation energy for hydrolyzing the Si-O-Al linkage that was 8 kcal/mol lower than that for hydrolyzing the Si-O-Si linkage.

Figure 6.12 shows the dissolution rate of the five glasses based on the release of the four elements present in these glasses for a value of *r* of 0.03. The rates of dissolution of Si and Na are superimposed and remain constant as B/Al increases. The rate of dissolution of Al diminishes with increasing the B/Al ratio as seen experimentally in Pierce et al. (2010). Finally, B increases as B/Al increases, again as seen experimentally in Pierce et al. (2010). However, when the rates of dissolution are normalized to the stoichiometries of the glasses (Figure 6.13), all four elemental dissolution rates are superimposed, clearly indicating that the glasses are dissolving congruently at all B/Al ratios. Therefore, our results suggest that the changes in the dissolution rates of B and Al observed experimentally are principally due to the changes in the stoichiometries of the glasses.

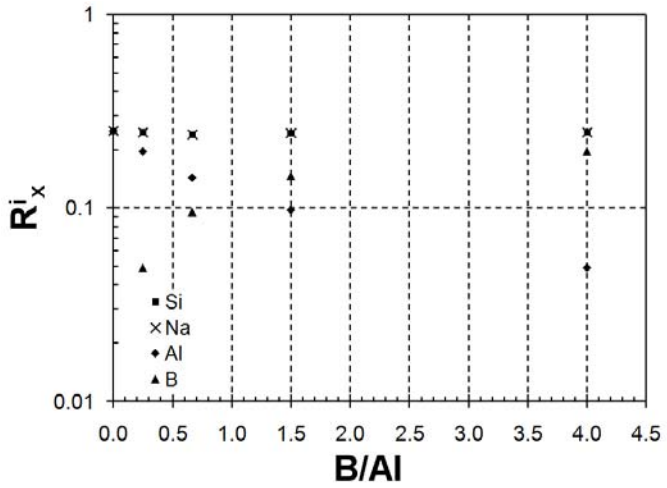

Figure 6.12. Elemental Dissolution Rates (R^i_x) in Sites Per Unit Area and Per Simulation Step as a Function of B/Al for r=0.03

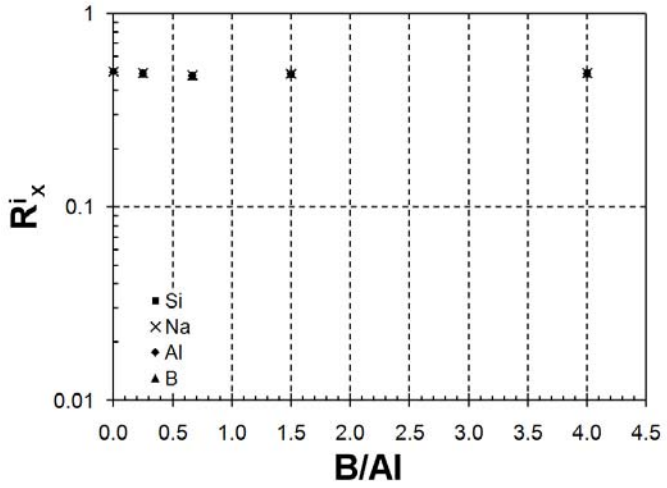

Figure 6.13. Elemental Dissolution Rate (R^i_x) in Stoichiometric Unit Per Unit Area and Per Simulation Step as a Function of the B/Al Ratio for r=0.03

To further investigate the structural and compositional characteristics that control glass dissolution and give rise to the experimentally observed dissolution behavior as a function of the B/Al ratio, we computed the composition of the glass-water interface (Figure 6.14) as well as the area and thickness of the hydration layer (Figure 6.15) from the simulations where r=0.03. Figure 6.15 shows that the amount of Al atoms that persist at the interface rapidly diminishes as the B/Al ratio increases, suggesting that Al only contributes to the glass resistance to dissolution at very low B/Al ratios. Figure 6.15 shows that both the surface area and the thickness of the hydration layer increase with increasing B content above a B/Al ratio of 0.667. Taken together, these two plots show that, although the overall dissolution rate remains fairly constant for r=0.03 when B/Al is varied, the dissolution behavior is somewhat different at low and high B/Al ratios. At low B/Al ratios, Al occupies a sizeable fraction of the interfacial sites. The low strength of the Al-O-Si linkage relative to that of the Si-O-Si linkage means that the glass dissolves relatively fast despite a low surface area and thin hydration layer. As the Al content decreases, the

interface is dominated by Si, but the expected decrease in dissolution rate is compensated by the increase in hydration layer thickness, which, as described previously, enhances the dissolution rate.

To conclude this section, using the value of *r* that yields the best agreement with the experimental dissolution rates of Pierce et al. (2010), the MC simulations suggest that the rupture of the Al-O-Si linkages contributes to the rate of dissolution at low B/Al ratios but not at high B/Al ratios.

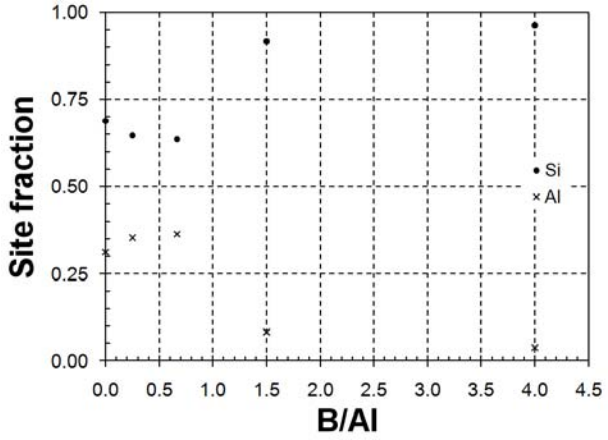

Figure 6.14. Average Site Fractions of Surface Sites that Persist After the Dissolution Stage of the MC Algorithm as a Function of the B/Al Ratio for *r*=0.03

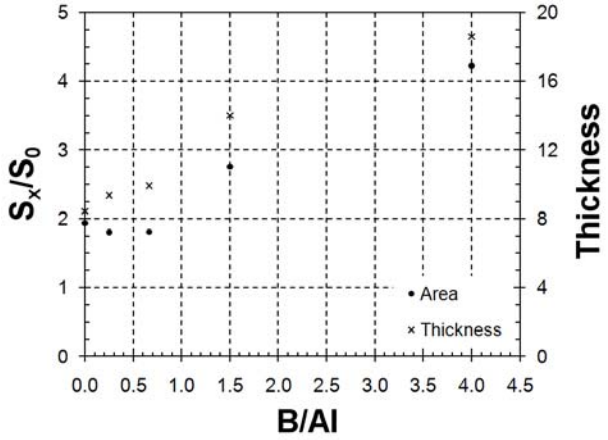

Figure 6.15. Hydration Layer Surface Area (S_x), Relative to Initial Surface Area (S_0), and Thickness as a Function of the B/Al Ratio for *r*=0.03

6.2.1.6 Kinetic Monte Carlo Summary

An MC program was designed and implemented to model the rates and mechanisms of dissolution of sodium aluminoborosilicate glasses in a simulated SPFT setup. A series of structural features (non-bridging oxygens, boroxol rings, and aluminum avoidance rule), relevant to the NeB glass series studied by Pierce et al. (2010), was implemented, and their effects on the dissolution of sodium borosilicate and sodium aluminosilicate glasses were studied individually.

Three dissolution regimes emerged when the boron content of sodium borosilicate glasses was varied over a wide range of values. At the boron-rich end, boron controls the dissolution, and the rate of dissolution is independent of the silicon dissolution probabilities. In addition, in these conditions, the hydration layer is thin as the dissolution is too rapid to allow for an extended hydration layer to form. At low Si/B ratios, the hydration layer becomes thicker as the silicon increases, S^2 and S^3 sites are dissolved mostly via detachment of clusters, and the dissolution rate is controlled by the dissolution of S^1 sites. At higher Si/B ratios, the dissolution via detachment of clusters plays a more minor role, and the dissolution rate is controlled by the dissolution of S^2 and then S^3 sites. In this regime, the thickness of the hydration layer diminishes as it becomes progressively more difficult for water to penetrate the glass structure.

The dissolution rate of sodium borosilicate glasses was found to be linearly dependent on the amount of non-bridging oxygens, and the effect of the non-bridging oxygens was more pronounced in the dissolution regime where the dissolution via detachment of clusters played a lesser role. Similarly, the formation of boroxol rings was found to enhance the dissolution rate, as compared to when only isolated boron atoms are present, and again this effect was more efficient at intermediate Si/B ratios where dissolution via detachment of clusters is low, but the boron content is still significant. Implementing the aluminum avoidance rule was found to decrease the dissolution rate of sodium aluminosilicate glasses for the two Si/Al ratios studied in this work. Scenarios where the Al-O-Si linkage is both stronger and weaker than the Si-O-Si linkage were investigated. In both cases, following the aluminum avoidance rule diminishes the dissolution rate as the thickness of the hydration layer decreases. This reducuction in hydration layer is cause by the reducing the probability that continuous networks of silicon sites will occur, when Al-O-Si is weak relative to Si-O-Si, and by more easily dissolving Al, when the Al-O-Si linkage is strong relative to Si-O-Si.

Finally, when the MC algorithm was applied to model the dissolution of the NeB glass series, a low value of the Al-O-Si linkage strength was found to best match the experimental data. The experimental study of Pierce et al. (2010) had concluded that the rupture of either the Al-O or Si-O bonds was the rate-limiting step controlling dissolution of the NeB glasses. Insights gained in our MC study allow us to refine this conclusion. Indeed, it was found that, at low B/Al ratios, the rupture of both Al-O-Si and Si-O-Si linkages contribute to the dissolution rate, whereas, at high B/Al ratios, the dissolution rate is independent of the rupture of Al-O-Si linkages and is controlled by S^1 sites and dissolution via detachment of clusters.

7.0 Near Field Modeling

7.1 Overview

A primary goal of the Near Field Modeling task was to transition from STORM, which was used in previous PAs, to STOMP-W-R, which has been validated as safety software through a rigorous testing program. A description of previous PA modeling is given in Section 7.2, and a description of the STORM and STOMP simulators is given in Section 7.3.

For the IDF PA, the following modes of STOMP have been tested to be compliant with Nuclear Quality Assurance (NQA)-1-2000 Software Requirements and DOE Order 414.1c: STOMP-W (water), STOMP-W-T (water with transport), and STOMP-W-R (water with reactions). The STOMP quality assurance program is described in Section 7.4.

Creating the near-field modeling framework has progressed through developing a STOMP simulation that incorporates the geochemical reaction network needed to model the weathering of waste glass. The reaction network includes all kinetic reactions, equilibrium reactions, mineral species, and aqueous species used in STORM simulations for the Sensitivity Analysis base case simulation at 99°C. Kinetic reactions include glass dissolution, sodium-hydrogen ion exchange, and secondary mineral precipitation. A one-dimensional (1-D), high-temperature simulation was chosen for the first STOMP/STORM benchmark to speed the development of the modeling framework because a 1-D simulation at high temperature requires a much shorter time to achieve a significant change in simulation output than a two-dimensional (2-D), field-scale simulation at low temperature and water flux. This was described in a report regarding the sensitivity of glass kinetic rate law parameters (Bacon and Pierce 2010). This initial STOMP/STORM benchmark is described in Section 7.5.

7.2 Previous Performance Assessment Modeling

A critical component of the PA will be to provide quantitative estimates of radionuclide release rates from the engineered portion of the disposal facilities (source term). Computer models are essential for this purpose because effects on groundwater resources must be projected out 10,000 years and longer. Details on the recommended technical strategy for developing this source term have been published (McGrail et al. 2003) and have undergone review by an international panel of experts.

The 2001 ILAW PA (Mann et al. 2001) showed that a key variable was the waste-form release rate, calculated over thousands of years. In this PA, the waste-form release rate was evaluated by modeling the basic physical and chemical processes that are known to control the waste-form dissolution behavior instead of using empirical extrapolations from laboratory "leaching" experiments commonly used in other PAs. This methodology was adopted for the following reasons:

- The radionuclide release rate from dissolving silicate glass or grout cannot be determined independently of other system variables. For example, neglecting the waste-form composition, the glass dissolution rate is a function of three variables: temperature, pH, and composition of the fluid contacting the glass (McGrail et al. 2001). The temperature of the ILAW disposal system is assumed to be known and constant. However, both pH and composition of the fluid contacting the glass are variables affected by flow rate, reactions with other engineered materials, gas-water equilibria, secondary phase precipitation, alkali ion exchange, and the glass-dissolution, classic-feedback

mechanism. Consequently, glass-dissolution rates vary both in time and as a function of position in the disposal system. A "leach rate" or radionuclide release rate parameter cannot be assigned to a waste form in such a dynamic system.

- One of the principal purposes of the IDF PA is to provide feedback to engineers regarding the effects of design options on disposal-system performance. A model based on empirical release rates for different waste forms is inadequate for this task. Unfortunately, the robust methodology we used comes with additional requirements. First, detailed information is needed on the reaction mechanisms controlling the dissolution behavior of the waste form. Laboratory experiments are required to obtain the rate-law parameters needed for the models used for our simulations. Second, the model now being used (described in the next section) is markedly more complex than a model based on empirical release rates because of its capability to simulate reactive transport coupled with heterogeneous, unsaturated flow. Execution times with today's most sophisticated massively parallel computers can be 2 weeks for the 2-D simulations presented in this report. The benefits, however, particularly with regard to the technical defensibility of the methodology and results, far outweigh the penalties.

For the 2005 IDF PA, a variety of waste-form materials were simulated, including three Hanford Tank Waste Treatment and Immobilization Plant (WTP) glasses (LAWA44, LAWB45, and LAWC22), grout, and two bulk-vitrification glasses, a six-tank composite, and S-109 (Bacon and McGrail 2005).

7.3 Numerical Simulators

7.3.1 STORM

STORM has been used to simulate the corrosion of waste forms containing radioactive glass at the Hanford Site in Richland, Washington (Bacon and McGrail 2005). STORM was developed by coupling STOMP, a non-isothermal multiphase flow simulator (White and Oostrom 2006), with Analyzer for RadionuclidE Source-Term with Chemical Transport (AREST-CT) Version 1.1, a reactive transport and porous medium alteration simulator (Chen et al. 1995, Chen et al. 1997). The underlying mathematics in STORM is contained in a set of coupled, nonlinear, partial differential equations. They describe the rate of change of the solute concentrations of pore water in a variably saturated, non-isothermal porous medium. STORM capabilities include kinetic dissolution of glass, kinetic precipitation and dissolution of secondary phases, aqueous equilibrium speciation, gas-aqueous equilibria, two-phase flow (water and air), and dynamic hydraulic properties.

STORM has the capability to simulate the special glass kinetic reaction in which many aqueous species are released, but equilibrium depends only on a few of these, such as silica and aluminum. Also, reactive transport in STORM is fully coupled with unsaturated flow; the unsaturated flow field may be altered by mineral dissolution and precipitation reactions. STORM runs efficiently in parallel on multi-core workstations and supercomputers, shortening execution times. The verification studies for STORM are documented in the STORM user's guide (Bacon et al. 2004).

However, STORM has certain limitations that limit its usefulness for the present work. Due to lack of funding, STORM has not been updated for 5 years, and has never been graded as Class C Safety and Hazard Analysis and Design Software. Therefore, under DOE Order 414.1C, STORM cannot be used for PAs. Also, reactive transport in STORM is limited to two dimensions.

7.3.2 STOMP

The Subsurface Transport Over Multiple Phases (STOMP) code has been graded as Class C Safety and Hazard Analysis and Design Software under DOE Order 414.1C (see Section 7.4.1), making it applicable to PAs. The flow modules in STORM were derived from STOMP. The main difference between STOMP and STORM is that STORM uses the AREST-CT reactive transport solver, and STOMP uses the ECKEChem reaction solver (White and McGrail 2005). AREST-CT uses a global implicit solution scheme in which the transport and reaction equations are solved simultaneously. ECKEChem uses an operator split-solution scheme in which the transport equations and reaction equations are solved sequentially.

The STOMP simulator (White and McGrail 2005) has been developed by PNNL for modeling subsurface flow and transport systems and remediation technologies. The STOMP simulator's fundamental purpose is to produce numerical predictions of thermal and hydrogeologic flow and transport phenomena in variably saturated subsurface environments. The STOMP simulator is written in the FORTRAN 77 and 90 languages, following American National Standards Institute (ANSI) standards. The simulator uses a variable source code configuration that allows the execution memory and speed to be tailored to the problem specifics and essentially requires that the source code be assembled and compiled through a software maintenance utility. Auxiliary applications include numerical predictions of solute transport processes, including reactive transport. Quantitative predictions from the STOMP simulator are generated from the numerical solution of partial differential equations that describe subsurface environment transport phenomena. The description of the contaminated subsurface environment is founded on governing conservation equations and constitutive functions. Governing coupled flow equations are partial differential equations for the conservation of water mass, air mass, and thermal energy. Constitutive functions relate primary variables to secondary variables. The governing partial differential equations are solved with the integral volume finite-difference method. The governing equations that describe thermal and hydrogeological flow processes are solved simultaneously using Newton-Raphson iteration to resolve the nonlinearities in the governing equations. Governing transport equations are partial differential equations for the conservation of solute mass. Governing equations for solute mass conservation are solved sequentially, following the solution of the coupled flow equations.

Version 4.0 of STOMP includes the PNNL-developed batch geochemistry solution module ECKEChem (Equilibrium-Conservation-Kinetic Equation Chemistry) (White and McGrail 2005). The ECKEChem batch-chemistry module was developed in a fashion that would allow its implementation into all operational modes of the STOMP simulator, making it a more versatile chemistry component. Additionally, this approach allows for verification of the ECKEChem module against more classical reactive transport problems involving aqueous systems. Currently, the ECKEChem package has been implemented in the *STOMP-W-R* and *STOMP-WCS-R* modes. The fundamental objective in developing the ECKEChem module was to embody a systematic procedure for converting geochemical systems for mixed equilibrium and kinetic reactions into a system of nonlinear equations. This objective has been realized through a recently developed general paradigm for modeling reactive chemicals in batch systems, which has been coded into a preprocessor for BIOGEOCHEM (Fang et al. 2003). To couple this processor to the STOMP simulator, a conversion program, BioGeoChemTo, was written in Perl that reads the preprocessor output and converts it into STOMP simulator input format. This addition has been incorporated in accord with the STOMP simulator quality assurance and control program; see Section 7.4.1 and the associated references for more detail.

7.4 Quality Assurance

The quality of the work was verified through compliance with *the ILAW Glass Testing for Disposal at IDF Quality Assurance Project Plan* (QAPP-EED-58762), which contains hyperlinks to the applicable requirements sections of PNNL's standards-based management system called "How Do I…?" (HDI). Computer software procedures were followed for STORM reactive transport software. All staff members contributing to the work described in this report have received proper technical and quality assurance training in the use and operation of the STORM and STOMP codes.

7.4.1 Description of STOMP QA/QC Program

The STOMP simulator is custom-developed software at PNNL that meets NQA-1-2000 software requirements as well as the requirements specified under DOE Order 414.1C for Safety Software. Specifically, STOMP management follows the PNNL HDI "Safety Software" subject area that is written to meet those requirements. To this end, STOMP development is managed under a configuration management plan (White and Freedman 2007) in conjunction with a software test plan (Freedman and White 2007) that detail the procedures used to test, document, and archive modifications to the source code. Formal procedures for software problem reporting and corrective actions for software errors and updates are maintained and rigorously implemented (Nichols and White 2007a). The documentation of all verification and validation testing is publicly available.

Managing STOMP software includes maintaining both an internal and external STOMP user list. PNNL STOMP users are trained in the design, use, and evaluation of the software (Oostrom et al. 2003). Internal users are also trained to the problem reporting and corrective action procedures that are outlined in the configuration management plan.

STOMP software is also supported by a software requirement specification (Zhang et al. 2007) and software design document (Nichols and White 2007b), which are essential for developing quality software and life cycle maintenance. In addition to the documentation used to manage and document software development, STOMP is supported by user and theory guides. The User Guide (White and Oostrom 2006) is frequently updated to document input requirements for new capabilities. Updates to the theory guide (White and Oostrom 2000) are supported by addendums (Ward et al. 2005, White and McGrail 2005).

STOMP software can be used in a variety of different applications, including the analysis of nuclear facilities. Hence, under DOE Order 414.1C, STOMP software has been generically graded as Class C Safety and Hazard Analysis and Design Software. This classification was selected because results from STOMP-based analyses may impact regulatory permitting requirements for nuclear facilities. The classification of the software, however, will be application dependent, and the classification is evaluated on a project basis.

For the IDF PA, the following modes of STOMP have been tested to be compliant with NQA-1-2000 Software Requirements and DOE Order 414.1c: STOMP-W, STOMP-W-T, and STOMP-W-R. These are the water, water with transport, and water with reactions modes, respectively. The verification test logs are maintained as a part of project records.

7.5 Benchmarking of STORM vs. STOMP

7.5.1 PUF Test Simulation Description

The PUF test column is modeled as a vertical, 1-D domain, 7.62-cm long, divided into 100 grid cells. The cross sectional area of the column is 2.856 cm^2. The upper boundary condition is a constant water influx of 0.70175 cm/day (2563 mm/yr), which, multiplied by the cross-sectional area, gives a flow rate of 2 mL/day. The column temperature is modeled as a constant 99°C. The inflowing and initial water in the column is assumed to be DIW with all total species concentrations equal to 1×10^{-10} mol/kg and pH equal to 7.

The glass composition used in the STOMP and STORM simulations is shown in (Table 7.1).

Table 7.1. LAWA44 Composition Used in STORM Simulations

Element	LAWA44 (mol fraction)
Al	8.15×10^{-2}
B	1.71×10^{-1}
Ca	2.38×10^{-2}
Cl	1.23×10^{-2}
Cr	1.76×10^{-4}
F	3.53×10^{-4}
Fe	5.86×10^{-2}
K	7.11×10^{-3}
Mg	3.31×10^{-2}
Mo	4.65×10^{-5}
Na	4.32×10^{-1}
O	$1.83 \times 10^{+0}$
P	2.83×10^{-4}
S	8.37×10^{-4}
Si	4.97×10^{-1}
Tc	2.77×10^{-4}
Ti	1.67×10^{-2}
Zn	2.44×10^{-2}
Zr	1.63×10^{-2}

For a dissolution reaction involving glass, parameters associated with the following kinetic rate law are needed:

$$r_g = \bar{k} a_{H^+}^{\eta} e^{\frac{-E_a}{RT}} \left[1 - \left(\frac{Q}{K_g} \right)^{\sigma} \right] \tag{5.1}$$

where r_g = dissolution rate, mol m^{-2} s^{-1}
$\vec{k}$ = intrinsic rate constant, mol m^{-2} s^{-1}
a_{H^+} = hydrogen ion activity (variable to be calculated by STORM)
E_a = activation energy, kJ/mol
R = gas constant, kJ/(mol·K)
T = temperature, K (assumed constant at 15°C)
Q = ion activity product for Glass (variable to be calculated by STORM)
K_g = pseudo-equilibrium constant
η pH power law coefficient
σ Temkin coefficient ($\sigma = 1$ assumed).

Equation (5.1) is an approximation for glass because glass is metastable, and the reaction proceeds one way (i.e., glass dissolves). The unknown parameters in Equation (5.1) ($\vec{k}$, E_a, K_g, and η) have been determined for LAW glasses (Pierce et al. 2004a) and bulk vitrification glasses (Pierce et al. 2004c); values for LAWA44 are given in Table 7.2.

Test results with LAW and bulk vitrification glasses (excluding LAWB45) show that it is susceptible to a secondary reaction mechanism, alkali ion exchange. This reaction results in the selective extraction of Na via the reaction:

$$\text{LAWA44-Na} + H^+ \rightarrow \text{LAWA44-H} + Na^+ \qquad (5.2)$$

where LAWA44-Na represents the unreacted glass containing Na, and LAWA44-H represents a hydrated glass where the Na has been replaced with an equimolar amount of hydrogen. The rate of this reaction has been determined from SPFT experiments (Pierce et al. 2004a; Pierce et al. 2004c). STORM keeps track of the amount of hydrated glass formed via reaction (5.2) and then allows it to dissolve according to the same kinetic rate law (Reaction 2) as the parent glass.

Table 7.2. Summary of Kinetic Rate Parameters Used for Glass

Parameter	Meaning	LAWA44
$\vec{k}$	Intrinsic rate constant, mol m^{-2} s^{-1}	2.25×10^{-3}
K_g	Apparent equilibrium constant for glass based on activity of SiO_2(aq)	$10^{-2.3}$
η	pH power law coefficient	-0.49
E_a	Activation energy of glass dissolution reaction, kJ/mol	60
r_x	Na ion-exchange rate, mol m^{-2} s^{-1}	1.51×10^{-8}

Secondary phases are solids that precipitate from a supersaturated aqueous solution. Potential secondary phases and their equilibrium constant values were determined using long-term weathering experiments with the various waste glass formulations and by modeling the analyzed solutions with the EQ3/6 code (Pierce et al. 2004b). The secondary phase and corresponding log K at 99ºC added to the geochemical database for the simulations are provided in Table 7.4 and were identified by simulating the dissolution of waste glass in DIW at 99°C with the EQ3/6 code package (Wolery and Jarek 2003). All data were obtained from the EQ3/6 data0.com.R8 database (Daveler and Wolery 1992). The EQ3/6 software was used to extract a subset of aqueous equilibrium reactions (Table 7.5) from the large thermodynamic database that were relevant for the reactive transport simulations.

Table 7.3. Composition of Secondary Minerals Used in Simulations

Species[(a)]	Formula	Mol. Wt.	Molar Volume
Anatase	TiO_2	79.8	20.5
Clinochlore-14Å	$Mg_5Al_2Si_3O_{10}(OH)_8$	555.8	207.1
Baddeleyite	ZrO_2	123.2	21.9
Diaspore	$AlHO_2$	60.0	17.8
$Zn(OH)_2$(gamma)	$Zn(OH)_2$	99.4	30.0

(a) All data were obtained from the EQ3/6 data0.com.R8 database (Daveler and Wolery 1992)

Table 7.4. Equilibrium Constants for Secondary Phases at 99°C

Reaction[(a)]	Log_{10} K (99°C)
$Anatase + 2H_2O = Ti(OH)_4(aq)$	-5.4
$Baddeleyite + 2H_2O = Zr(OH)_4(aq)$	-5.2
$Clinochlore\text{-}14Å = 3SiO_2(aq) + 5Mg^{2+} + 8OH^- + 2AlO_2^-$	-79.0
$Diaspore = AlO_2^- + OH^-$	-4.7
$Zn(OH)_2(gamma) = 2OH^- + Zn^{2+}$	-15.0

(a) All data were fit to SPFT data for LAWA44 glass (Pierce et al. 2004b)

Table 7.5. Aqueous Equilibrium Reactions at 99°C

Reaction[(a)]	$\text{Log}_{10}\ K$ (99°C)
$Al(OH)_2^+ + 2OH^- = AlO_2^-$	14.912
$BO_2^- + H_2O = OH^- + B(OH)_3(aq)$	-3.45
$CO_2(aq) + OH^- + H_2O = HCO_3^-$	5.89
$CO_3^- = OH^- + HCO_3^-$	-2.19
$CaB(OH)_4^+ = OH^- + B(OH)_3(aq) + Ca^{2+} + H_2O$	-4.85
$CaCO_3(aq) = OH^- + Ca^{2+} + HCO_3^-$	-6.30
$CaHCO_3^+ = Ca^{2+} + HCO_3^-$	-1.41
$CaHPO_4(aq) = Ca^{2+} + HPO_4^{2-}$	-2.74
$CaPO_4^- = OH^- + Ca^{2+} + HPO_4^{2-}$	-6.41
$CaSO_4(aq) = Ca^{2+} + SO_4^{2-}$	-2.50
$Fe(OH)_2^+ + H_2O + OH^- = + Fe(OH)_3(aq)$	5.94
$Fe(OH)_4^- = OH^- + H_2O + Fe(OH)_3(aq)$	-2.67
$H_2PO_4^- + OH^- = HPO_4^{2-}$	4.99
$H_6(H_2SiO_4)_4^{2-} = 2OH^- + 4SiO_2(aq) + 8H_2O$	-10.90
$HAlO_2(aq) + OH^- = AlO_2^-$	6.85
$HCrO_4^- + OH^- = CrO_4^{2-}$	5.33
$HSiO_3^- = OH^- + H_2O + SiO_2(aq)$	-3.18
$MgB(OH)_4^+ = OH^- + B(OH)_3(aq) + H_2O + Mg^{2+}$	-4.93
$MgCO_3(aq) = OH^- + HCO_3^- + Mg^{2+}$	-5.70
$MgHCO_3^+ = HCO_3^- + Mg^{2+}$	-1.43
$MgHPO_4(aq) = HPO_4^{2-} + Mg^{2+}$	-2.91
$MgPO_4^- = OH^- + HPO_4^{2-} + Mg^{2+}$	-6.54
$MgSO_4(aq) = Mg^{2+} + SO_4^{2-}$	-3.34
$Na_2HPO_4(aq) = HPO_4^{2-} + 2Na^+$	-1.00
$NaAlO_2(aq) = Na^+ + AlO_2^-$	0.25
$NaB(OH)_4(aq) = OH^- + B(OH)_3(aq) + H_2O + Na^+$	-3.30
$NaCl(aq) = Cl^- + Na^+$	0.48
$NaF(aq) = F^- + Na^+$	0.63
$NaHCO_3(aq) = HCO_3^- + Na^+$	0.40
$NaHPO_4^- = HPO_4^{2-} + Na^+$	-0.92
$NaHSiO_3(aq) = OH^- + H_2O + Na^+ + SiO_2(aq)$	-4.44
$NaSO_4^- = Na^+ + SO_4^{2-}$	-0.82
$OH^- + H^+ = H_2O$	12.27
$PO_4^{3-} = OH^- + HPO_4^{2-}$	-0.20
$Zn(OH)_2(aq) = 2OH^- + Zn^{2+} + 2H_2O$	-7.22
$ZnCO_3(aq) = OH^- + HCO_3^- + Zn^{2+}$	-5.84
$ZnOH^+ = OH^- + H_2O + Zn^{2+}$	-5.26
$ZnPO_4^- = OH^- + HPO_4^{2-} + Zn^{2+}$	-7.97

(a) All data were obtained from the EQ3/6 data0.com.R8 database (Daveler and Wolery 1992).

7.5.2 PUF Test Simulation Results

Results from STOMP and STORM compare well; concentrations of $B(OH)_3(aq)$, H^+, Na^+ and TcO_4^- at the bottom node of the PUF column are nearly identical (Figure 7.1). Fluxes of water and TcO_4^- at the bottom outflow boundary of the PUF column are also very similar (Figure 7.2). Slight differences at early times may be attributed to the fact that STORM includes a feature to have fixed gas species concentrations; in this case, $CO_2(g)$ was fixed at a partial pressure of 3×10^{-4} atm. This assumes that equilibrium with atmospheric CO_2 buffers the pH. In the STOMP simulation, which does not currently

have the option to simulate gas species, the total amount of dissolved carbonate was set to a value of 3.52×10^{-4}. This value of dissolved carbonate was equal to the value observed in the STORM simulation at the bottom node at steady state, but was higher than the average value in the PUF column. For this reason, pH buffering in the STOMP simulation may have been slightly too high, resulting in the TcO_4^- flux being slightly too low.

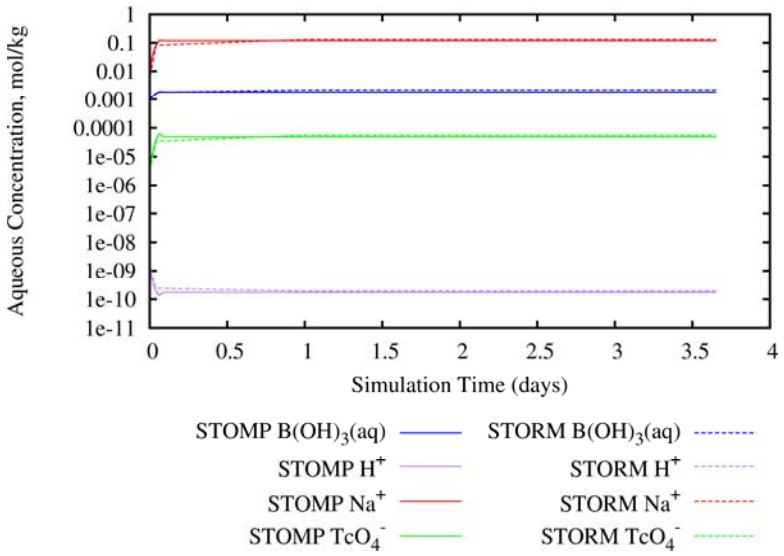

Figure 7.1. Comparison of Concentrations at the Bottom of PUF Column Predicted by STOMP and STORM

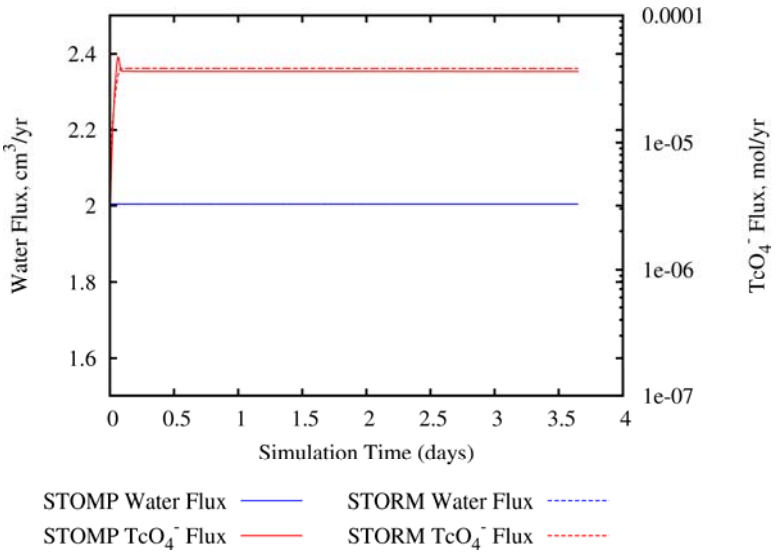

Figure 7.2. Comparison of Water and TcO_4^- Flux from Bottom Outflow Boundary of PUF Column Predicted by STOMP and STORM

7.6 Near Field Modeling Summary

The STOMP code does not include several of the features required to exactly reproduce STORM simulations developed for previous PAs. As mentioned in the previous section, STOMP-W-R does not have the capability of simulating gas species. Also, in STORM, the effective reaction area for the glass is decreased at low moisture contents, which reduces the glass dissolution rate. Also in STORM, the porosity changes as the glass dissolves, and secondary minerals precipitate, which decreases the flow of water through the glass. In addition, the surface area of precipitated secondary minerals is calculated in STORM and is specified as a constant value in STOMP. All of these features affect the rate of Tc flux from the repository, and hence the predicted performance of the glass. It is planned to incorporate these features into STOMP over the next several months and to rerun the validation test suite that is required to certify STOMP as safety software.

8.0 Compilation of Alteration Phases

Low-Activity Waste (LAW) performance assessment models must account for the long-term corrosion rate of each LAW glass formulation. This corrosion rate is a key parameter affecting the overall performance of the integrated disposal facility (IDF). In addition to rate law parameters, additional data are also required to conduct source-term calculations with the STORM code is 1) a set of secondary phases that form from the long-term corrosion of these glasses in the disposal system environment, and 2) the precipitation-dissolution rate and/or solubility product for each of these phases. Although the suite of weathering products that will form as a consequence of the glass-water reactions cannot be determined a priori at this time, discussed by McGrail et al. (2001b), laboratory tests can be used to simulate and accelerate the weathering process. These weathering test include the product consistency test (PCT-B), vapor hydration test, and pressurized unsaturated flow (PUF) apparatus. This section provides an overview of each test method, along with a list of the alteration phases identified from the weathering of a series of HLW ILAW glasses using the various test methods.

8.1 Product Consistency Test

The PCT method is a water-saturated and static (closed-system) test, based on the MCC test method number three (MCC-3). The PCT Method A was developed specifically for verifying process control of vitrified HLW forms and is conducted with specific test conditions: -100 +200 mesh size fraction material; demineralized water; and a solid/solution mass ratio of 1/10, 90°C, and 7 days. It is conducted by immersing a specimen of crushed glass in a volume of leachant at a known surface area-to-solution volume ratio (S/V). The mass and size fraction of the crushed material in the test is known and used to estimate the surface area. The test vessel is sealed and placed in a constant-temperature oven for a prescribed duration. The solution concentrations of components of interest are measured at the end of the test. The tests are usually conducted in demineralized water, but can be conducted with synthetic or actual groundwaters.

Unlike the PCT Method A which is conducted under specific test conditions, the PCT Method B is also a water saturated static (closed-system) test that does not specify the values of test parameters. The reaction products are allowed to accumulate in the aqueous phase, thus altering the solution chemistry in contact with the glass. Although information on the solution chemistry is obtained, the changes to the solution chemistry measured in this closed-system test may not be representative of the solution chemistry that is expected in an open-system repository. For example, PUF tests results with LD6-5412 and LAWA33 glasses suggests that in PUF test the ageing processes are accelerated by as much as 50 times in comparison to the PCT method run at the same temperature (McGrail et al. 1999). This observed acceleration in the ageing process is probably the results of the differences in the glass-water reaction rate, the solution chemistry, and the rate of alteration phase formation in PUF test in comparison to PCT.

8.2 Vapor Hydration Test Method

The VHT is the simplest accelerated test to be used in the recommended testing strategy because there is only one degree of freedom in test parameters that can be varied, temperature, excluding test duration and humidity. The principle use of the test is as a convenient means of generating alteration phases for analysis within a short period, but it is also useful for a qualitative measure of the effect of

alteration phase formation on the corrosion rate. The VHT is a static test in which a monolithic sample is exposed to water vapor in a sealed vessel. At relative humidity (RH) above about 80%, a thin film of water condenses on the sample. The thickness of the film increases with the RH, and it is in this film that the glass corrodes. The thickness of the film determines the effective S/V ratio of the system; for a uniform layer, the S/V ratio is simply the inverse of the thickness of the film. Most VHTs have been performed in 100% relative humidity at temperatures above 100°C, although tests have been conducted at lower humidity and temperature. At the completion of a test, the sample is removed from the vessel, and the reacted surface is analyzed with high-resolution electron microscopy. Discrete precipitated crystalline phases usually form when the sample corrodes. The solution evaporates from the sample when the test is terminated and is not available for analysis. This precludes using the test to evaluate and test models of glass corrosion behavior, which require detailed measurements of the solution composition in contact with the glass.

Vapor hydration has been used by archaeologists to replicate the weathering observed on obsidian artifacts recovered from terrestrial sites (Friedman and Long 1976). The method has also been used to simulate the long-term weathering of tektite (Mazer et al. 1992) and basaltic glasses (Byers et al. 1986). Because the test method produces the same alteration phases that form during the weathering of natural glasses over long periods, the test has also been used to accelerate the corrosion of waste glasses.

8.3 Pressurized Unsaturated Flow Test Method

The PUF apparatus allows for accelerated weathering experiments to be conducted under hydraulically unsaturated conditions, thereby mimicking the open-flow and transport properties of the disposal system environment while allowing the dissolving glass to achieve a final reaction state. The final reaction state, commonly referred to as Stage IV in the weathering process of glasses, is a point reached during long-term weathering that consists of the formation of secondary phases, while stage I and II mechanisms (e.g., network hydrolysis, ion exchange, and network dissolution) occur simultaneously (see Section 2.1). The PUF apparatus provides the capability to vary the volumetric water content from saturation to 20% or less, minimize the flow rate to increase liquid residence time, and operate at a maximum temperature of 99°C. The PUF column operates under a hydraulically unsaturated condition by creating a steady-state vertical water flow, while maintaining uniform water content throughout the column; by using gravity to assist in drainage; and by maintaining a constant pressure throughout the column. Constant pressure is maintained with a porous Ti plate and gas pressure. For a more detailed description of the PUF system see McGrail et al. (1996, 1999a,b, and 2000a) and Pierce et al. (2004a, 2006, 2007, and 2009).

8.4 Alteration Phases

A list of the alteration phases observed in accelerated weathering experiments are listed in Table 8.1.

Table 8.1. Compiled List of Alteration Phases

Glass Type	Method	Temp °C	Duration (days)	Phase ID	Mass % Estimate	Phase ID Method	Comment	Reference
GP WAK1	Closed system - Clay pore water solutions	50 , 90 ºC	14 – 800	Powellite, barite, Mg(Ca,Fe) silicate	--	XAS		Bosbach et al 2009
NIT04	Closed system- humic acid solution under N_2	60 ºC	76	Fe, Zr enriched phases	--	Rutherford backscattering spectrometry (RBS)		Takagi et al. 2004
LAW BP1	Closed system- static test, Hanford groundwater	160 ºC	42	Analcime, zeolite P, Cancrinite	15 -30, 60 – 75, 10	XRD, SEM-EDX		Mattigod et al 2003
LAW BP1	Closed system- dynamic test, Hanford groundwater	95, 160 ºC	7 cycles of 7 days each. Total 49 days	Analcime, zeolite P, Cancrinite	95 ºC - amorphous phase, 160 C – Analcime 95%, phillipsite 5%	XRD, SEM-EDX		Mattigod et al 2003
LAW BP1	Closed system- static test, Hanford groundwater spiked with ^{75}Se, ^{99}Tc, or ^{125}I + stable Se, I	160 ºC	42	Analcime, sodalite	10 - 100, 90 - 100	XRD, SEM-EDX		Mattigod et al 2003
LAWA44	Closed system- static test Hanford groundwater	160 ºC	42	Analcime, zeolite P,	35 – 100, 65	XRD, SEM-EDX		Mattigod et al 2003
LAW A44	Closed system- static test, Hanford groundwater spiked with ^{75}Se, ^{99}Tc, or ^{125}I + stable Se, I	160 ºC	42	Sodalite, unidentified crystalline phase	95, 5	XRD, SEM-EDX		Mattigod et al 2003
LAW33	Closed system- Hanford groundwater	160 ºC	14	Analcime, herschelite, phillipsite & paragonite	5 – 65, 20 – 75, 15 - 30	XRD, SEM-EDX		Mattigod et al 2002
LD6	Closed system- Hanford groundwater	160 ºC	14-Jul	Analcime, thermonitrite	95 -100, <5	XRD, SEM-EDX		Mattigod et al 2002
R7T7	Closed system – NaOH solution 0.03, 0.1, 0.5M	120 , 150, 180 ºC	Oct-80	Analcime, Na-beidellite	10 – 19%, no estimate for beidellite	XRD		Inagaki et al 2002
R7T7	Closed system – KOH solution 0.1M	120 , 150, 180 ºC	Oct-80	amorphous	--	XRD		Inagaki et al 2002
R7T7	Closed system – DI water	120 , 150, 180 ºC	Oct-80	Na-beidellite	--	XRD		Inagaki et al 2002
Borosilicate	Closed system – ambient air	ambient	14 - 240	Na_2CO_3, $NaBO_2 \cdot H_2O$	--	CPMAS -NMR		Egan & Mueller 2000
SRL 202A	Closed system – water vapor	150 - 200	Jul-56	analcime, adularia, Na-weeksite, halweeite	--	Optical microscopy, XRD, SEM-EDS,		Wronkiewicz et al 1993

Glass Type	Method	Temp °C	Duration (days)	Phase ID	Mass % Estimate	Phase ID Method	Comment	Reference
		ºC				AEM		
SRL 165A, U	Closed system – water vapor	150 - 200 ºC	Jul-56	Analcime, weeksite, adularia, Ca-Si phase, tobermorite, calcite	--	Optical microscopy, XRD, SEM-EDS, AEM		Wronkiewicz et al 1993
SRL 131A	Closed system – water vapor	150 - 200 ºC	Jul-56	Analcime, weeksite, herschelite, phillipsite, unidentified	--	Optical microscopy, XRD, SEM-EDS, AEM		Wronkiewicz et al 1993
SRL 131	MCC-1	40 & 90 ºC	~1460	Birnessite, saponite, nontronite, serpentine/nontronite, amorphous phase	--	TEM		Bates et al. 1991
SRL 165	MCC-1	40 & 90 ºC	~1460	Fe, Ca, Zr-rich smectit	--	TEM		Bates et al. 1991
HMI	MIIT test WIPP	90 ºC	180 - 730	Amor Mg-silicate, Mg chloride, anhydrite	--	SEM, XRD, EMPA, AEM		Jercinovic et al 1990
R7T7	MIIT test WIPP	90 ºC	730	Amor Mg-silicate, Mg-oxychloride, halite	--	SEM, XRD, EMPA, AEM		Jercinovic et al 1990
Borosilicate	MCC-1	90 ºC	14-Jan	Al, Fe, Co crystalline fibers	--	AEM		Murakami et al 1989
R7T7	Closed system - DI water	60 -200 ºC	0.5	Fe, Zr, REE hydrosilicates	--	RBS		Petit et al 1989
Borosilicate BS	Closed system - DI water	65 ºC	25	Ca-Al hydrosilicates	--	RBS		Petit et al 1989
R7T7	Closed system – DI water	250 ºC	28	Analcime, pollucite	--	XRD, SEM		Caurel et al 1988
R7T7	Closed system – DI water	250 & 300 ºC	28	Amorphous phase, Datolite, danburyite, uralborite, natrolite thomsonite, gonnardite, mesolite, analcime albite, natrolite, elpidite, catapleite, zeckzerite, emeleusite,	--	XRD, SEM		Caurel et al 1988
Basaltic glass	DI water, 0.5M NaCl, 0.05 $MgCl_2$ solution	70 ºC	301	Amorphous Fe, Ti hydroxide, gibbsite, palagonite	--	AEM		Murakami et al 1985
R7T7	DI water, NaCl brine	20 & 90 ºC	0.04 - 28	Ni,Zn silicates, Zr Silicate	--	AEM, XPS, SEM		Godon et al 1988
C-31-3-EC-SPF-Na	Closed system – NaCl brine	200 ºC	3 - 1000	Analcime, phyllosilicates (Na-mont), willeite, hemimorphite, arsenate apatite, barium molybdate, calcium molybdate, Ba chromate-molybdate, Ca uranyl silicate	Analcime Al:Si 4.6:10.6 atom%, phyllosilicate Al:Si:Mg:Zn 0.7:3.1:0.9:1.3 Zinc silicate Zn:Si 0.3:0.2	XRD, EPMA, SEM		Haaker et al 1985
Borosilicate	Open system – Soxhlet extraction-DI water	100 ºC	0.5 - 60	Fe, Ni, U, REE hydroxides	--	XPS, RBS		Manara et al 1985
MCC-DWRG	MCC-1 with DI water, Grand Ronde groundwater	90 ºC	140	Mg oxychloride, Mg-montmorillonite, amorphous material	--	SEM/EDX, XRD, XPS, SIMS		Flintoff and Harker 1985
MCC-DWRG, ICPP-127, PNL	Open system – DI water	90 ºC	28-Apr	Fe,Zr silicate, Al,Ca Mg hydrates	--	SIPS, SIMS		Hauser and Pantano 1985a,b

Glass Type	Method	Temp °C	Duration (days)	Phase ID	Mass % Estimate	Phase ID Method	Comment	Reference
76-68								
ABS 39, 41	STRIPA burial in contact with glass	90 ºC	365	Mg, Ca, Sr, Ba, Zn,Al, Fe silicates and hydroxides	--	SIMS, FTIRRS		Hench and Werme 1984
C31-3EC	Closed system – NaCl solution	200ºC	0.2 - 365	Anacime, U-rich crystals (U, Ti, Si, Na, Fe, Zn, Ca), unidentified crystalline phase (Si, Al, Mg, Fe, Ti, Mn)	--	TEM, SEM-EDX, EPMA		Lutz et al 1983
C31-3EC	Closed system – DI water	165ºC	0.2 - 365	Zn-rich nodules (Zn, Si, Na, Ni, Fe, Al, Ba), Zn-rich needles (Zn, Si, Al, Mg, Na)	--	TEM, SEM-EDX, EPMA		Lutz et al 1983
HLP-01	VHT-DIW	200	125	Analcime-C ($NaAlSi_2O_6•H_2O$)	97	XRD	surface material	Vienna et al. (2001)
HLP-01	VHT-DIW	200	125	Sodium titanium silicate ($NaTiSi_2O_6$)	3	XRD	surface material	Vienna et al. (2001)
HLP-02	VHT-DIW	200	30	Sodium aluminum silicate boron hydroxide hydrate ($Na_{7.55}(AlSiO_4)_6(B(OH)_4)_{1.685}•1.97H_2O$	69	XRD	bulk glass	Vienna et al. (2001)
HLP-02	VHT-DIW	200	30	Analcime-C ($NaAlSi_2O_6•H_2O$)	16	XRD	bulk glass	Vienna et al. (2001)
HLP-02	VHT-DIW	200	30	Sodium titanium silicate ($NaTiSi_2O_6$)	15	XRD	bulk glass	Vienna et al. (2001)
HLP-03	VHT-DIW	200	125	Analcime-C ($NaAlSi_2O_6•H_2O$)	90	XRD	surface material	Vienna et al. (2001)
HLP-03	VHT-DIW	200	125	Sodium titanium silicate ($NaTiSi_2O_6$)	10	XRD	surface material	Vienna et al. (2001)
HLP-04	VHT-DIW	200	16	Analcime-C ($NaAlSi_2O_6•H_2O$)	46	XRD	bulk glass	Vienna et al. (2001)
HLP-04	VHT-DIW	200	16	Sodium titanium silicate ($NaTiSi_2O_6$)	44	XRD	bulk glass	Vienna et al. (2001)
HLP-04	VHT-DIW	200	16	Pinakiolite [$(Mg,Mn)_2Mn(BO_3)_2$]	10	XRD	bulk glass	Vienna et al. (2001)
HLP-05	VHT-DIW	300	8	Aegirine [$NaFe(SiO_3)_2$]	96	XRD	surface material	Vienna et al. (2001)
HLP-05	VHT-DIW			Unidentified phase	4	XRD	surface material	Vienna et al. (2001)
HLP-06	VHT-DIW	200	106	Analcime-C ($NaAlSi_2O_6•H_2O$)	100	XRD/SEM-EDS	surface material	Vienna et al. (2001)
HLP-07	VHT-DIW	200	100	Analcime-C ($NaAlSi_2O_6•H_2O$)	94	XRD	bulk glass	Vienna et al. (2001)
HLP-07	VHT-DIW	200	100	Sodium titanium silicate ($NaTiSi_2O_6$)	6	XRD	bulk glass	Vienna et al. (2001)
HLP-08	VHT-DIW	200	100	Analcime-C ($NaAlSi_2O_6•H_2O$)	95	XRD	surface material	Vienna et al. (2001)
HLP-08	VHT-DIW	200	100	Sodium titanium silicate ($NaTiSi_2O_6$)	5	XRD	surface material	Vienna et al. (2001)
HLP-09	VHT-DIW	300	5	Analcime-C ($NaAlSi_2O_6•H_2O$)	93	XRD/SEM-EDS	surface material	Vienna et al. (2001)
HLP-09	VHT-DIW	300	5	Sodium titanium silicate ($NaTiSi_2O_6$)	4	XRD/SEM-EDS	surface material	Vienna et al. (2001)
HLP-09	VHT-DIW	300	5	Sodium aluminum silicate hydrate[$Na_3Al_3Si_3O_{12}•2H_2O$	3	XRD/SEM-EDS	surface material	Vienna et al. (2001)
HLP-10	VHT-DIW	200	129	Analcime-C ($NaAlSi_2O_6•H_2O$)	98	XRD	surface material	Vienna et al. (2001)
HLP-10	VHT-DIW	200	129	Sodium titanium silicate ($NaTiSi_2O_6$)	2	XRD	surface material	Vienna et al. (2001)
HLP-11	VHT-DIW	200	68	Analcime-C ($NaAlSi_2O_6•H_2O$)	100	XRD	surface material	Vienna et al. (2001)
HLP-12	VHT-DIW	200	105	Analcime-C ($NaAlSi_2O_6•H_2O$)	82	XRD/SEM-EDS	bulk glass	Vienna et al. (2001)
HLP-12	VHT-DIW	200	105	Aegirine [$NaFe(SiO_3)_2$]	18	XRD/SEM-EDS	bulk glass	Vienna et al. (2001)

Glass Type	Method	Temp °C	Duration (days)	Phase ID	Mass % Estimate	Phase ID Method	Comment	Reference
HLP-12	VHT-DIW	300	2	Analcime-C ($NaAlSi_2O_6•H_2O$)	45	XRD	bulk glass	
HLP-12	VHT-DIW	300	2	Sodium titanium silicate ($NaTiSi_2O_6$)	55	XRD	bulk glass	Vienna et al. (2001)
HLP-13	VHT-DIW	200	80	Analcime-C ($NaAlSi_2O_6•H_2O$)	97	XRD	surface material	Vienna et al. (2001)
HLP-13	VHT-DIW	200	80	Sodium titanium silicate ($NaTiSi_2O_6$)	3	XRD	surface material	Vienna et al. (2001)
HLP-14	VHT-DIW	200	101	Analcime-C ($NaAlSi_2O_6•H_2O$)	57	XRD	bulk glass	Vienna et al. (2001)
HLP-14	VHT-DIW	200	101	Aegirine [$NaFe(SiO_3)_2$]	43	XRD	bulk glass	Vienna et al. (2001)
HLP-15	VHT-DIW	200	75	Analcime-C ($NaAlSi_2O_6•H_2O$)	99	XRD	surface material	Vienna et al. (2001)
HLP-15	VHT-DIW	200	75	Sodium titanium silicate ($NaTiSi_2O_6$)	1	XRD	surface material	Vienna et al. (2001)
HLP-16	VHT-DIW	200	75	Analcime-C ($NaAlSi_2O_6•H_2O$)	98	XRD	surface material	Vienna et al. (2001)
HLP-16	VHT-DIW	200	75	Sodium titanium silicate ($NaTiSi_2O_6$)	2	XRD	surface material	Vienna et al. (2001)
HLP-17	VHT-DIW	200	75	Analcime-C ($NaAlSi_2O_6•H_2O$)	98	XRD	surface material	Vienna et al. (2001)
HLP-17	VHT-DIW	200	75	Sodium titanium silicate ($NaTiSi_2O_6$)	2	XRD	surface material	Vienna et al. (2001)
HLP-18	VHT-DIW	200	32	Analcime-C ($NaAlSi_2O_6•H_2O$)	93	XRD	bulk glass	Vienna et al. (2001)
HLP-18	VHT-DIW	200	32	Sodium titanium silicate ($NaTiSi_2O_6$)	7	XRD	bulk glass	Vienna et al. (2001)
HLP-19	VHT-DIW	300	3	Analcime-C ($NaAlSi_2O_6•H_2O$)	30	XRD	bulk glass	Vienna et al. (2001)
HLP-19	VHT-DIW	300	3	Sodium aluminum silicate boron hydroxide hydrate ($Na_{7.55}(AlSiO_4)_6(B(OH)_4)_{1.685}•1.97H_2O$	10	XRD	bulk glass	Vienna et al. (2001)
HLP-19	VHT-DIW	300	3	Acmite-augite [$(Na,Ca)FeSi_2O_6$]	60	XRD	bulk glass	Vienna et al. (2001)
HLP-20	VHT-DIW	200	75	Analcime-C ($NaAlSi_2O_6•H_2O$)	87	XRD	surface material	Vienna et al. (2001)
HLP-20	VHT-DIW	200	75	Sodium titanium silicate ($NaTiSi_2O_6$)	13	XRD	surface material	Vienna et al. (2001)
HLP-21	VHT-DIW	200	32	Analcime-C ($NaAlSi_2O_6•H_2O$)	85	XRD	surface material	Vienna et al. (2001)
HLP-21	VHT-DIW	200	32	Unidentified phase	15	XRD	surface material	Vienna et al. (2001)
HLP-22	VHT-DIW	200	32	Analcime-C ($NaAlSi_2O_6•H_2O$)	71	XRD	surface material	Vienna et al. (2001)
HLP-22	VHT-DIW	200	32	Unidentified phase	29	XRD	surface material	Vienna et al. (2001)
HLP-23	VHT-DIW	200	7	Analcime-C ($NaAlSi_2O_6•H_2O$)	95	XRD	surface material	Vienna et al. (2001)
HLP-23	VHT-DIW	200	7	Sodium aluminum silicate hydrate [$Na_6Al_6Si_{10}O_{32}•12H_2O$]	5	XRD	surface material	Vienna et al. (2001)
HLP-24	VHT-DIW	200	32	Analcime-C ($NaAlSi_2O_6•H_2O$)	95	XRD	surface material	Vienna et al. (2001)
HLP-24	VHT-DIW	200	32	Sodium titanium silicate ($NaTiSi_2O_6$)	5	XRD	surface material	Vienna et al. (2001)
HLP-27	VHT-DIW	200	4	Analcime-C ($NaAlSi_2O_6•H_2O$)	88	XRD	bulk glass	Vienna et al. (2001)
HLP-27	VHT-DIW	200	4	Sodium aluminum silicate hydrate [$Na_6Al_6Si_{10}O_{32}•12H_2O$]	12	XRD	bulk glass	Vienna et al. (2001)
HLP-27	VHT-DIW	200	100	Analcime-C ($NaAlSi_2O_6•H_2O$)	100	XRD	bulk glass	Vienna et al. (2001)

Glass Type	Method	Temp °C	Duration (days)	Phase ID	Mass % Estimate	Phase ID Method	Comment	Reference
HLP-28	VHT-DIW	200	300	Analcime-C ($NaAlSi_2O_6•H_2O$)	100	XRD	surface material	
HLP-29	VHT-DIW	200	13	Analcime-C ($NaAlSi_2O_6•H_2O$)	39	XRD	bulk glass	Vienna et al. (2001)
HLP-29	VHT-DIW	200	13	Sodium titanium silicate ($NaTiSi_2O_6$)	60	XRD	bulk glass	Vienna et al. (2001)
HLP-29	VHT-DIW	200	13	Sodium aluminum silicate boron hydroxide hydrate ($Na_{7.55}(AlSiO_4)_6(B(OH)_4)_{1.685}•1.97H_2O$	1	XRD	bulk glass	Vienna et al. (2001)
HLP-30	VHT-DIW	200	23	Analcime-C ($NaAlSi_2O_6•H_2O$)	94	XRD	surface material	Vienna et al. (2001)
HLP-30	VHT-DIW	200	23	Tincalconite [$Na_2B_4O_7•5H_2O$]	6	XRD	surface material	Vienna et al. (2001)
HLP-31	VHT-DIW	200	2	Analcime-C ($NaAlSi_2O_6•H_2O$)	100	XRD/SEM-EDS	surface material	Vienna et al. (2001)
HLP-31	VHT-DIW	200	10	Analcime-C ($NaAlSi_2O_6•H_2O$)	68	XRD	bulk glass	Vienna et al. (2001)
HLP-31	VHT-DIW	200	10	Sodium titanium silicate ($NaTiSi_2O_6$)	32	XRD	bulk glass	Vienna et al. (2001)
HLP-32	VHT-DIW	200	24	Analcime-C ($NaAlSi_2O_6•H_2O$)	85	XRD	surface material	Vienna et al. (2001)
HLP-32	VHT-DIW	200	24	Sodium titanium silicate ($NaTiSi_2O_6$)	15	XRD	surface material	Vienna et al. (2001)
HLP-33	VHT-DIW	200	129	Analcime-C ($NaAlSi_2O_6•H_2O$)	93	XRD	surface material	Vienna et al. (2001)
HLP-33	VHT-DIW	200	129	Sodium titanium silicate ($NaTiSi_2O_6$)	7	XRD	surface material	Vienna et al. (2001)
HLP-33	VHT-DIW	300	5	Analcime-C ($NaAlSi_2O_6•H_2O$)	29	XRD/SEM-EDS	bulk glass	Vienna et al. (2001)
HLP-33	VHT-DIW	300	5	Sodium titanium silicate ($NaTiSi_2O_6$)	71	XRD/SEM-EDS	bulk glass	Vienna et al. (2001)
HLP-34	VHT-DIW	300	8	Analcime-C ($NaAlSi_2O_6•H_2O$)	8	XRD	surface material	Vienna et al. (2001)
HLP-34	VHT-DIW	300	8	Sodium aluminum silicate boron hydroxide hydrate ($Na_{7.55}(AlSiO_4)_6(B(OH)_4)_{1.685}•1.97H_2O$	46	XRD	surface material	Vienna et al. (2001)
HLP-34	VHT-DIW	300	8	Phillipsite ($(K,Na)_2(Si, Al)_8O_{16}•4H_2O$)	46	XRD	surface material	Vienna et al. (2001)
HLP-35	VHT-DIW	200	21	Analcime-C ($NaAlSi_2O_6•H_2O$)	61	XRD	bulk glass	Vienna et al. (2001)
HLP-35	VHT-DIW	200	21	Sodium aluminum silicate boron hydroxide hydrate ($Na_{7.55}(AlSiO_4)_6(B(OH)_4)_{1.685}•1.97H_2O$	39	XRD	bulk glass	Vienna et al. (2001)
HLP-36	VHT-DIW	200	32	Analcime-C ($NaAlSi_2O_6•H_2O$)	86	XRD	surface material	Vienna et al. (2001)
HLP-36	VHT-DIW	200	32	Tincalconite [$Na_2B_4O_7•5H_2O$]	14	XRD	surface material	Vienna et al. (2001)
HLP-37	VHT-DIW	200	24	Analcime-C ($NaAlSi_2O_6•H_2O$)	76	XRD	surface material	Vienna et al. (2001)
HLP-37	VHT-DIW	200	24	Pinakiolite [$(Mg,Mn)_2Mn(BO_3)_2$]	24	XRD	surface material	Vienna et al. (2001)
HLP-38	VHT-DIW	200	24	Analcime-C ($NaAlSi_2O_6•H_2O$)	38	XRD	bulk glass	Vienna et al. (2001)
HLP-38	VHT-DIW	200	24	Sodium aluminum silicate boron hydroxide hydrate ($Na_{7.55}(AlSiO_4)_6(B(OH)_4)_{1.685}•1.97H_2O$	2	XRD	bulk glass	Vienna et al. (2001)
HLP-38	VHT-DIW	200	24	Spinel ($[Fe,Zn,Ni][Fe,Ti,Cr]_2O_4$)	60	XRD	bulk glass	Vienna et al. (2001)
HLP-38	VHT-DIW	200	64	Analcime-C ($NaAlSi_2O_6•H_2O$)	24	XRD	bulk glass	Vienna et al. (2001)

Glass Type	Method	Temp °C	Duration (days)	Phase ID	Mass % Estimate	Phase ID Method	Comment	Reference
HLP-38	VHT-DIW	200	64	Sodium aluminum silicate boron hydroxide hydrate ($Na_{7.55}(AlSiO_4)_6(B(OH)_4)_{1.685}•1.97H_2O$	10	XRD	bulk glass	Vienna et al. (2001)
HLP-38	VHT-DIW	200	64	Spinel ($[Fe,Zn,Ni][Fe,Ti,Cr]_2O_4$)	66	XRD	bulk glass	Vienna et al. (2001)
HLP-39	VHT-DIW	300	5	Aegirine [$NaFe(SiO_3)_2$]	58	XRD	bulk glass	
HLP-39	VHT-DIW	300	5	Zirconium oxide ($Zr_{0.94}O_2$)	26	XRD	bulk glass	Vienna et al. (2001)
HLP-39	VHT-DIW	300	5	Catapleite, [$Na_2ZrSi_3O_9•H_2O_2$]	16	XRD	bulk glass	Vienna et al. (2001)
HLP-40	VHT-DIW	275	5	Analcime-C ($NaAlSi_2O_6•H_2O$)	5	XRD	bulk glass	Vienna et al. (2001)
HLP-40	VHT-DIW	275	5	Sodium aluminum silicate boron hydroxide hydrate ($Na_{7.55}(AlSiO_4)_6(B(OH)_4)_{1.685}•1.97H_2O$	33	XRD	bulk glass	Vienna et al. (2001)
HLP-40	VHT-DIW	275	5	Acmite-augite [$(Na,Ca)FeSi_2O_6$]	62	XRD	bulk glass	Vienna et al. (2001)
HLP-41	VHT-DIW	200	120	Analcime-C ($NaAlSi_2O_6•H_2O$)	90	XRD	surface material	Vienna et al. (2001)
HLP-41	VHT-DIW	200	120	Sodium titanium silicate ($NaTiSi_2O_6$)	10	XRD	surface material	Vienna et al. (2001)
HLP-42	VHT-DIW	200	68	Analcime-C ($NaAlSi_2O_6•H_2O$)	33	XRD	surface material	Vienna et al. (2001)
HLP-42	VHT-DIW	200	68	Sodium titanium silicate ($NaTiSi_2O_6$)	5	XRD	surface material	Vienna et al. (2001)
HLP-42	VHT-DIW	200	68	Spinel, $[Fe,Zn,Ni][Fe,Ti,Cr]_2O_4$	62	XRD	surface material	Vienna et al. (2001)
HLP-43	VHT-DIW	200	33	Analcime-C ($NaAlSi_2O_6•H_2O$)	53	XRD	bulk glass	Vienna et al. (2001)
HLP-43	VHT-DIW	200	33	Sodium titanium silicate ($NaTiSi_2O_6$)	6	XRD	bulk glass	Vienna et al. (2001)
HLP-43	VHT-DIW	200	33	Pinakiolite [$(Mg,Mn)_2Mn(BO_3)_2$]	41	XRD	bulk glass	Vienna et al. (2001)
HLP-44	VHT-DIW	300	3	Analcime-C ($NaAlSi_2O_6•H_2O$)	79	XRD	bulk glass	Vienna et al. (2001)
HLP-44	VHT-DIW	300	3	Aegirine [$NaFe(SiO_3)_2$]	21	XRD	bulk glass	Vienna et al. (2001)
HLP-45	VHT-DIW	300	3	Analcime-C ($NaAlSi_2O_6•H_2O$)	65	XRD	bulk glass	Vienna et al. (2001)
HLP-45	VHT-DIW	300	3	Aegirine [$NaFe(SiO_3)_2$]	35	XRD	bulk glass	Vienna et al. (2001)
HLP-46	VHT-DIW	200	1	Analcime-C ($NaAlSi_2O_6•H_2O$)	97	XRD/SEM-EDS	bulk glass	Vienna et al. (2001)
HLP-46	VHT-DIW	200	1	Gobbinsite, $[Ca_{0.6}Na_{2.6}K_{2.2}Al_6Si_{10}O_{32}•12H_2O]$	3	XRD/SEM-EDS	bulk glass	Vienna et al. (2001)
HLP-46	VHT-DIW	200	4	Analcime-C ($NaAlSi_2O_6•H_2O$)	95	XRD	bulk glass	Vienna et al. (2001)
HLP-46	VHT-DIW	200	4	Gobbinsite, $[Ca_{0.6}Na_{2.6}K_{2.2}Al_6Si_{10}O_{32}•12H_2O]$	5	XRD	bulk glass	Vienna et al. (2001)
HLP-47	VHT-DIW	200	24	Analcime-C ($NaAlSi_2O_6•H_2O$)	97	XRD/SEM-EDS	bulk glass	Vienna et al. (2001)
HLP-47	VHT-DIW	200	24	Sodium titanium silicate ($NaTiSi_2O_6$)	3	XRD/SEM-EDS	bulk glass	Vienna et al. (2001)
HLP-48	VHT-DIW	200	20	Analcime-C ($NaAlSi_2O_6•H_2O$)	41	XRD/SEM-EDS	bulk glass	Vienna et al. (2001)
HLP-48	VHT-DIW	200	20	Sodium aluminum silicate boron hydroxide hydrate ($Na_{7.55}(AlSiO_4)_6(B(OH)_4)_{1.685}•1.97H_2O$	51	XRD/SEM-EDS	bulk glass	Vienna et al. (2001)
HLP-48	VHT-DIW	200	20	Pinakiolite [$(Mg,Mn)_2Mn(BO_3)_2$]	8	XRD/SEM-EDS	bulk glass	Vienna et al. (2001)

Glass Type	Method	Temp °C	Duration (days)	Phase ID	Mass % Estimate	Phase ID Method	Comment	Reference
HLP-49	VHT-DIW	200	50	Analcime-C ($NaAlSi_2O_6•H_2O$)	47	XRD	surface material	Vienna et al. (2001)
HLP-49	VHT-DIW	200	50	Unidentified phase	53	XRD	surface material	Vienna et al. (2001)
HLP-51	VHT-DIW	150	187	Analcime-C ($NaAlSi_2O_6•H_2O$)	13	XRD	surface material	Vienna et al. (2001)
HLP-51	VHT-DIW	150	187	Phillipsite [$(K,Na)_2(Si, Al)_8O_{16}•4H_2O$]	87	XRD	surface material	
HLP-51	VHT-DIW	200	75	Analcime-C ($NaAlSi_2O_6•H_2O$)	19	XRD/SEM-EDS	bulk glass	Vienna et al. (2001)
HLP-51	VHT-DIW	200	75	Sodium aluminum silicate hydrate [$Na_6Al_6Si_{10}O_{32}•12H_2O$]	81	XRD/SEM-EDS	bulk glass	Vienna et al. (2001)
HLP-51	VHT-DIW	250	3	Analcime-C ($NaAlSi_2O_6•H_2O$)	70	XRD	surface material	Vienna et al. (2001)
HLP-51	VHT-DIW	250	3	Sodium aluminum silicate boron hydroxide hydrate $(Na_{7.55}(AlSiO_4)_6(B(OH)_4)_{1.685}•1.97H_2O$	30	XRD	surface material	Vienna et al. (2001)
HLP-52	VHT-DIW	200	13	Sodium zirconium silicate [$Na_{14}Zr_2Si_{10}O_{31}$]	38	XRD	bulk glass	Vienna et al. (2001)
HLP-52	VHT-DIW	200	13	Sodium aluminum silicate hydrate [$Na_{14}Al_{12}Si_{13}O_{51}•6H_2O$]	62	XRD	bulk glass	Vienna et al. (2001)
HLP-53	VHT-DIW	200	3	Sodium aluminum silicate boron hydroxide hydrate $(Na_{7.55}(AlSiO_4)_6(B(OH)_4)_{1.685}•1.97H_2O$	94	XRD	bulk glass	Vienna et al. (2001)
HLP-53	VHT-DIW	200	3	Calcium silicate hydroxide hydrate [$Ca_{4.5}Si_6O_{15}(OH)_3•2H_2O$]	6	XRD	bulk glass	Vienna et al. (2001)
HLP-54	VHT-DIW	200	41	Analcime-C ($NaAlSi_2O_6•H_2O$)	65	XRD	bulk glass	Vienna et al. (2001)
HLP-54	VHT-DIW	200	41	Sodium aluminum silicate boron hydroxide hydrate $(Na_{7.55}(AlSiO_4)_6(B(OH)_4)_{1.685}•1.97H_2O$	45	XRD	bulk glass	Vienna et al. (2001)
HLP-55	VHT-DIW	200	14	Analcime-C ($NaAlSi_2O_6•H_2O$)	40	XRD	bulk glass	Vienna et al. (2001)
HLP-55	VHT-DIW	200	14	Sodium aluminum silicate boron hydroxide hydrate $(Na_{7.55}(AlSiO_4)_6(B(OH)_4)_{1.685}•1.97H_2O$	60	XRD	bulk glass	Vienna et al. (2001)
HLP-56	VHT-DIW	250	5	Analcime-C ($NaAlSi_2O_6•H_2O$)	96	XRD	surface material	Vienna et al. (2001)
HLP-56	VHT-DIW	250	5	Sodium titanium silicate ($NaTiSi_2O_6$)	4	XRD	surface material	Vienna et al. (2001)
HLP-56	VHT-DIW	250	7	Analcime-C ($NaAlSi_2O_6•H_2O$)	71	XRD	surface material	Vienna et al. (2001)
HLP-56	VHT-DIW	250	7	Sodium titanium silicate ($NaTiSi_2O_6$)	20	XRD	surface material	Vienna et al. (2001)
HLP-56	VHT-DIW	250	7	Catapleite, [$Na_2ZrSi_3O_9•2H_2O$]	9	XRD	surface material	Vienna et al. (2001)
HLP-56	VHT-DIW	300	3	Analcime-C ($NaAlSi_2O_6•H_2O$)	21	XRD/SEM-EDS	surface material	Vienna et al. (2001)
HLP-56	VHT-DIW	300	3	Sodium titanium silicate ($NaTiSi_2O_6$)	72	XRD/SEM-EDS	bulk glass	Vienna et al. (2001)
HLP-56	VHT-DIW	300	3	Sodium aluminum silicon oxide [$Na_{2.12}Al_2Si_2O_{8.06}$]	7	XRD/SEM-EDS	bulk glass	Vienna et al. (2001)
HLP-58	VHT-DIW	200	101	Analcime-C ($NaAlSi_2O_6•H_2O$)	present	XRD	bulk glass	Vienna et al. (2001)
HLP-59	VHT-DIW	200	44	Analcime-C ($NaAlSi_2O_6•H_2O$)	present	XRD	bulk glass	Vienna et al. (2001)

Glass Type	Method	Temp °C	Duration (days)	Phase ID	Mass % Estimate	Phase ID Method	Comment	Reference
HLP-59	VHT-DIW	200	44	Unidentified phase	present	XRD	bulk glass	Vienna et al. (2001)
HLP-61	VHT-DIW	200	149	Analcime-C ($NaAlSi_2O_6•H_2O$)	present	XRD	bulk glass	Vienna et al. (2001)
HLP-61	VHT-DIW	200	149	Unidentified phase	present	XRD	bulk glass	Vienna et al. (2001)
HLP-64	VHT-DIW	200	44	Unidentified phase	present	XRD/SEM-EDS	bulk glass	Vienna et al. (2001)
HLP-65	VHT-DIW	200	28	Analcime-C ($NaAlSi_2O_6•H_2O$)	present	XRD	bulk glass	Vienna et al. (2001)
HLP-65	VHT-DIW	200	28	Unidentified phase	present	XRD	bulk glass	Vienna et al. (2001)
HLP-65	VHT-DIW	200	43	Analcime-C ($NaAlSi_2O_6•H_2O$)	present	XRD	bulk glass	Vienna et al. (2001)
HLP-68	VHT-DIW	200	28	Analcime-C ($NaAlSi_2O_6•H_2O$)	present	XRD	bulk glass	
HLP-69	VHT-DIW	200	42	Unidentified phase	present	XRD/SEM-EDS	bulk glass	Vienna et al. (2001)
HLP-70	VHT-DIW	200	28	Unidentified phase	present	XRD/SEM-EDS	bulk glass	Vienna et al. (2001)
HLP-71	VHT-DIW	200	28	Unidentified phase	present	XRD	bulk glass	Vienna et al. (2001)
HLP-72	VHT-DIW	200	50	Unidentified phase	present	XRD	bulk glass	Vienna et al. (2001)
HLP-72	VHT-DIW	200	151	Analcime-C ($NaAlSi_2O_6•H_2O$)	present	XRD	bulk glass	Vienna et al. (2001)
HLP-72	VHT-DIW	200	151	Unidentified phase	present	XRD	bulk glass	Vienna et al. (2001)
HLP-74	VHT-DIW	200	29	Analcime-C ($NaAlSi_2O_6•H_2O$)	present	XRD	bulk glass	Vienna et al. (2001)
HLP-74	VHT-DIW	200	29	Unidentified phase	present	XRD	bulk glass	Vienna et al. (2001)
HLP-75	VHT-DIW	200	28	Analcime-C ($NaAlSi_2O_6•H_2O$)	present	XRD	bulk glass	Vienna et al. (2001)
HLP-75	VHT-DIW	200	42	Analcime-C ($NaAlSi_2O_6•H_2O$)	present	XRD	bulk glass	Vienna et al. (2001)
HLP-76	VHT-DIW	200	42	Analcime-C ($NaAlSi_2O_6•H_2O$)	present	XRD	bulk glass	Vienna et al. (2001)
HLP-77	VHT-DIW	200	42	Analcime-C ($NaAlSi_2O_6•H_2O$)	present	XRD	bulk glass	Vienna et al. (2001)
HLP-02	PCT-DIW, S/V ratio of about 2300 m^{-1}	90	42	Phillipsite $(K,Na)_2(Si, Al)_8O_{16}•4H_2O$	present	XRD	bulk glass	Ebert et al. (2001)
AMBG-05-Q	VHT-DIW	200	21	Cancrinite $[Na_6CaAl_6Si_6(CO_3)O_{24}•2H_2O]$ and Analcime-$[NaAlSi_2O_6•H_2O]$	present	XRD	bulk glass	Hrma et al. (2005)
AMBG-05-SC	VHT-DIW	200	21	Analcime-$[NaAlSi_2O_6•H_2O]$	present	XRD	bulk glass	Hrma et al. (2005)
AMBG-11-Q	VHT-DIW	200	14	Hydroxycancrinite – $Na_8Al_6Si_6O_{24}(OH)_2•2H_2O$, Lithium Titanium Oxide – $LiTiO_2$	present	XRD	bulk glass	Hrma et al. (2005)
AMBG-11-SC	VHT-DIW	200	14	Hydroxycancrinite – $Na_8Al_6Si_6O_{24}(OH)_2•2H_2O$	present	XRD	bulk glass	Hrma et al. (2005)
AMBG-13-Q	VHT-DIW	200	28	Analcime-$[NaAlSi_2O_6•H_2O]$	present	XRD	bulk glass	Hrma et al. (2005)
AMBG-13-SC	VHT-DIW	200	28	Analcime-$[NaAlSi_2O_6•H_2O]$	present	XRD	bulk glass	Hrma et al. (2005)
AMBG-15-Q	VHT-DIW	200	14	Analcime-$[NaAlSi_2O_6•H_2O]$, Nosean – $Na_8SO_4Al_6Si_6O_{24}$	present	XRD	bulk glass	Hrma et al. (2005)

Glass Type	Method	Temp °C	Duration (days)	Phase ID	Mass % Estimate	Phase ID Method	Comment	Reference
AMBG-15-SC	VHT-DIW	200	14	Sodalite – $Na_8(AlSiO_4)_6(ClO_3)_{1.91}(OH)_{0.09,}$ Analcime-[$NaAlSi_2O_6•H_2O$] , Calcium Zirconium Oxide – [$CaZrO_3$]	present	XRD	bulk glass	Hrma et al. (2005)
ASCM-04-Q	VHT-DIW	200	14	Analcime-[$NaAlSi_2O_6•H_2O$] , Calcium Zirconium Oxide – [$CaZrO_3$] , Lithium Iron Oxide -[$LiFeO_2$]	present	XRD	bulk glass	Hrma et al. (2005)
ASCM-05-Q	VHT-DIW	200	14	Sodalite – $Na_8(AlSiO_4)_6(ClO_3)_{1.91}(OH)_{0.09,}$ Lithium Iron Oxide -[$LiFeO_2$]	present	XRD	bulk glass	Hrma et al. (2005)
SON-68	PCT-DIW, S/V ratio of 2000 cm-1	>150	not specified	Analcime-[NaAlSi2O6•H2O] and Pollucite	present	XRD/SEM-EDS	alteration phase	Frugier et al. (2006)
SON-68	PCT-DIW, S/V ratio of 2000 cm-1	150	561	Nontronite [$Na_{0.33}Fe_2Al_{0.33}Si_{3.67}O_{10}(OH)_2$]	present	XRD/SEM-EDS	alteration phase	Frugier et al. (2006)
LAWA44	PUF-DIW; 2ml/d flow rate	90	550	Clinochlore ferroan [$(Mg, Fe, Al)_6(Si,Al)_4O_{10}(OH)_8$]	present	XRD/SEM-EDS		Pierce and Bacon (2009)
LAW-AN102	PUF-DIW; 2ml/d flow rate	90	560	no chrystalline phases observed	amorphous alteration solids observed	XRD/SEM-EDS		Pierce et al. (2006)

VHT – Vapor Hydration Test
DIW – Deionized Water
PCT – Product Consistency Test
PUF – Pressurized Unsaturated Flow Test
XRD – X-ray Diffraction
SEM-EDS – Scanning Electron Microscopy with Energy Dispersive Spectroscopy
SIM – Secondary Ion Mass Spectrometry

9.0 Summary

A combined experimental and computational approach is being used to predict the long-term performance of ILAW glass in a near-surface disposal facility. This report highlights the activities that were performed at PNNL during FY2010. In summary, these results discussed in this report will be used to conduct source term calculation using the STOMP code in future IDF PAs and to develop a link between glass composition and alteration phase formation. Although improvements have been made to the STOMP code during FY2010, at the time this report was written several of the features that have an affect on the rate of Tc flux from the repository, and hence the predicted performance of the glass, are still being added. It is planned to incorporate these features into STOMP over the next several months and to rerun the validation test suite that is required to certify STOMP as safety software. In addition to improving the continuum scale simulations of glass weather, a combined MC and geochemical modeling approach is being used to link glass composition to alteration phase formation. In support of these simulations, a compiled list of alteration phases have been developed and additional glass characterization is being performed using SEM, XRD, Raman spectroscopy, and magic angle spinning nuclear magnetic resonance spectroscopy. The results from this effort will be used as input information for the MC and geochemical modeling calculations.

10.0 References

Aagaard P and HC Helgeson. 1982. "Thermodynamic and Kinetic Constraints on Reaction Rates among Minerals and Aqueous Solutions. I. Theoretical Considerations." *American Journal of Science* 282:237-285.

Abraitis PK, FR Livens, JE Monteith, JS Small, DP Trivedi, DJ Vaughan and RA Wogelius. 2000. "The kinetics and mechanisms of simulated British Magnox waste glass dissolution as a function of pH, silicic acid activity, and time in low temperature aqueous systems." *Applied Geochemistry* 15:1399-1416.

Aertsens M and P Van Iseghem. 1996. "Modelling glass dissolution with a Monte Carlo technique." *Mater. Res. Soc. Symp. Proc.* 412:271-278.

Arab M, C Cailleteau, F Angeli, F Devreux, L Girard, and O Spalla. 2008. "Aqueous alteration of five-oxide silicate glasses: Experimental approach and Monte Carlo modeling." *J. Non-Cryst. Solids* 354:155-161.

Bacon DH and BP McGrail. 2005. *Waste Form Release Calculations for the 2005 Integrated Disposal Facility Performance Assessment*. PNNL-15198, Pacific Northwest National Laboratory, Richland, Washington.

Bacon DH and EM Pierce. 2010. *Sensitivity Analysis of Kinetic Rate-Law Parameters Used to Simulate Long-Term Weathering of ILAW Glass*. PNNL-19472, Pacific Northwest National Laboratory, Richland, Washington.

Bacon DH, MD White, and BP McGrail. 2004. *Subsurface Transport Over Reactive Multiphases (STORM): A Parallel, Coupled, Nonisothermal Multiphase Flow, Reactive Transport, and Porous Medium Alteration Simulator, Version 3.0, User's Guide*. PNNL-14783, Pacific Northwest National Laboratory, Richland, Washington.

Barkatt A, BC Gibson, PB Macedo, CJ Montrose, W Sousanpour, A Barkatt, MA Boroomand, V Rogers and M Penafiel. 1986. "Mechanisms of defense waste glass dissolution." *Nuclear Technology* 73:140-164.

Bates, JK, LJ Jardine, and MJ Steindler. 1982. "Hydration Aging of Nuclear Waste glass." *Science* 218:51-54.

Bates JK, WL Ebert, JJ Mazer, JP Bradley, CR Bradley, and NL Dietz. 1991. "The Role of Surface Layers in Glass Leaching Performance." *Material Research Society Symposium Proceedings*, v. 212, pp. 77 - 87, Material Research Society, Pittsburgh, Pennsylvania.

Bethke CM and S Yeakel. 2009. *The Geochemist's Workbench®, Release 8.0, Reference Manual*. Hydrogeology Program, University of Illinois, Urbana, Illinois.

Bosbach, D, B Lucksheiter, B Bredebach, MA Denecke, and N Finck. 2009. High Leel Nuclear Waste Glass Corrosion in Synthetic Clay Pore solution and retention of Actinides in Secondary Phases. *Journal of Nuclear Materials* 385:456-460.

Bourcier WL. 1991. "Overview of chemical modeling of nuclear waste glass dissolution." *Material Research Symposium Proceedings* 212:3-17.

Brawer, SA and WB White. (1977). "Raman Spectroscopic Investigation of the Structure of Silicate Glasses (II). Soda-Alkaline Earth-Alumina Ternary and Quaternary Glasses." Journal of Non-Crystalline Solids, Vol. 23, pp. 261.

Bunker BC, DR Tallant, TJ Headley, GL Turner and RJ Kirkpatrick. 1988. "The Structure of Leached Sodium Borosilicate Glass." *Physics and Chemistry of Glasses* 29(3):106-120.

Byers CD, MJ Jercinovic, and RC Ewing. 1986. *A Study of Natural Glass Analogues as Applied to Alteration of Nuclear Waste Glass*. NUREG/CR-4842, Nuclear Regulatory Commission, Washington D.C.

Cailleteau C, F Angeli, F Devreux, S Gin, J Jestin, P Jollivet, and O Spalla. 2008a. "Insight into silicate-glass corrosion mechanisms." *Nature Mat.* **7:**978-983.

Cailleteau C, C Weigel, A Ledieu, P Barboux, and F Devreux F. 2008b. "On the effect of glass composition in the dissolution of glasses by water." *J. Non-Cryst. Solids* 354:117-123.

Casey WH. 1991. "On the relative dissolution rates of some oxide and orthosilicate minerals." *Journal of Colloid Interface Science* 146:586-589.

Casey WH and BC Bunker. 1990. "Leaching of Mineral and Glass Surfaces During Dissolution." *Mineral-Water Interface Geochemistry*. MF Hochella, Jr. and AF White (eds.). Washington, D.C., *Mineralogical Society of America*. 23:397-426.

Caurel J, D Beaufort, and EY Vernaz. 1988. "Mineral Phase Identification Along Two Profiles from LWR French Reference Glass: Use of an X-Ray Position Sensitive Detector." *Material Research Society Symposium Proceedings*, v. 112, pp. 663-672, Material Research Society,

Pittsburgh, PennsylvaniaChen Y, DW Engel, BP McGrail, and KS Lessor. 1995. *AREST-CT V1.0 Software Verification*. PNL-10692, Pacific Northwest Laboratory, Richland, Washington.

Chen Y, BP McGrail, and DW Engel. 1997. "Source-term analysis for Hanford low-activity tank waste using the reaction-transport code AREST-CT." In: *Scientific Basis for Nuclear Waste Management XX*, Pittsburgh, Pennsylvania.

Chryssikos, GD, EI Kamitsos, AP Patsis, MS Bitsis, and MA Karakassides. (1990). "The Devitrification of Lithium Metaborate: Polymorphism and Glass Formation." Journal of Non-Crystalline Solids, Vol. 126, No. 1-2, pp. 42-51.

Cunnane JC, JK Bates, and CR Bradley. 1994a. *High-level Borosilicate Waste Glass: A Compendium of Corrosion Characteristics*, vol. 1. DOE-EM-0177, U.S. Department of Energy, Office of Waste Management, Springfield, Virginia.

Cunnane JC, JK Bates, CR Bradley. 1994b. *High-Level Waste Borosilicate Glass: A Compendium of Corrosion Characteristics*, vol. 2. DOE-EM-0177, U.S. Department of Energy, Office of Waste Management, Springfield, Virginia.

Daveler SA and TJ Wolery. 1992. *EQPT, A Data File Preprocessor for the EQ3/6 Software Package: User's Guide and Related Documentation (Version 7.0)*. UCRL-MA-110662 PT II, Lawrence Livermore National Laboratory, Livermore, California.

Devreux F, P Barboux, M Filoche, and B Sapoval. 2001. "A simplified model for glass dissolution in water." *J. Mater. Sci.* 36:1331-1341.

Devreux F, A Ledieu, P Barboux, and Y Minet. 2004. "Leaching of borosilicate glasses. II. Model and Monte-Carlo simulations." *J. Non-Cryst. Solids* 343:13-25.

Devreux F, C Cailleteau, and P Barboux. 2010. "Evidence for a Threshold in the Biosolubility of Aluminosilicate Vitreous Fibers." *Journal of Material Science* 45:1154-1159.

Doremus RH. 1975. "Interdiffusion of hydrogen and alkali ions in a glass surface." *Journal Non-Crystalline Solids* 19:137-144.

Du L-S and JF Stebbins. 2003. "Solid-State NMR study of metastable immiscibility in alkali borosilicate glasses." *J. Non-Cryst. Solids* 315:239-255.

Ebert, WL, NL Dietz, MA Lewis, PL Johnson, and BS Tani. 2001. *Long-Term and Accelerated Testing of Hanford Low-Activity Waste Glasses Through Fiscal Year.* Letter Report, Argonne National Laboratory, Chicago, Illinois.

Egan, JM and KT Mueller. 2000. "Detection and identification of Corrosion Products of Sodium Aluminoborosilicate Glasses by ^{23}Na MQMAS and ^{1}H → ^{23}Na CPMAS NMR." *Journal of Physical Chemistry B* 104:9589-9586.

Fang YL, GT Yeh, and WD Burgos. 2003. "A general paradigm to model reaction-based biogeochemical processes in batch systems." *Water Resources Research* 39(4):1083.

Flintoff JF and AB Harker. 1985. "Detailed Processes of Surface Layer Formation in Borosilicate Waste Glass Dissolution." *Material Research Society Symposium Proceedings*, v. 44, pp. 147-154, Material Research Society, Pittsburgh, Pennsylvania.

Friedman I and W Long. 1976. "Hydration Rate of Obsidian." *Science* 191:347-352.

Freedman VL and MD White. 2007. *STOMP Software Test Plan*. PNNL-SA-54022, Pacific Northwest National Laboratory, Richland, Washington.

Frugier, P, S Gin, JE Lartigue, and E Deloule. 2006. "SON68 Glass Dissolution Kinetics at High Reaction Progress: Mechanisms Accounting for the Residual Alteration Rate." in Scientific Basis for Nuclear Waste Management XXIX, edited by P. Van Isheghem, Mater. Res. Soc. Symp. Proc. 932, Warrendale, PA, paper 9.

Furukawa, T. and WB White. (1981). "Raman Spectroscopic Investigation of Sodium Borosilicate Glass Structure." Journal of Material Science, Vol. 16, No. 10, pp. 2689 – 2700.

Godon, N, JH Thomassin, JC Touray, and E Vernaz. 1988. "Experimental alteration of R7T7 Nuclear Model Glass in solutions with Different salinities (90 C, 1 bar): Implications for the selection of Geological Repositories." *Journal of Material Science* 23:126-134.

Grambow B. 1985. "A General Rate Equation For Nuclear Waste Glass Corrosion." In: *Material Research Symposium Proceedings* 44:15-27.

Haaker R, G Malow, and P Offerman. 1985. "The Effects of phase Formation on Glass

Leaching." *Material Research Society Symposium Proceedings*, v. 44, pp. 121-128, Material Research Society, Pittsburgh, Pennsylvania.

Hench LL, DE Clark, and AB Harker. 1986. "Nuclear waste solids." *Journal of Materials Science* 21:1457-1478.

Houser CA and CG Pantano. 1985a. "Application of XPS and Nuclear Technique to Study of Gel Layers formed under different Redox Conditions on Leached Glasses." *Material Research Society Symposium Proceedings*, v. 44, pp. 63-71, Material Research Society, Pittsburgh, Pennsylvania.

Houser CA and CG Pantano. 1985b. "Early Stages of Film formation during the Leaching of Radioactive Waste Glasses." *Material Research Society Symposium Proceedings*, v. 44, pp. 203-211, Material Research Society, Pittsburgh, Pennsylvania.

Hoshen J and R Kopelman. 1976. "Percolation and cluster distribution. I. Cluster multiple labeling technique and critical concentration algorithm." *Phys. Rev. B* 14:3438-3445.

Hrma PR, DS Kim, JD Vienna, J Matyas, DE Smith, MJ Schweiger, and JD Yeager. 2005. *Testing of Large-Scale ICV Glasses with Hanford LAW Simulant* . PNNL-15107, Pacific Northwest National Laboratory, Richland, WA.

Icenhower JP, S Samson, A Luttge and BP McGrail. 2004. "Towards a consistent rate law: glass corrosion kinetics near saturation." In: *Energy, Waste, and the Environment: A Geochemical Perspective*. R Giere and P Stille (eds.), Geological Society of London. 236:579-594.

Icenhower JP, BP McGrail, WJ Shaw, EM Pierce, P Nachimuthu, DK Shuh, EA Rodriguez, and JL Steele. 2008. "Experimentally determined dissolutio kinetics of Na-rich borosilicate glass at far from equilibrium conditions: Implications for Transition State Theory." *Geochim. Cosmochim. Acta* 72:2767-2788.

Inagaki, Y, H. Furuya, K. Idemitsu and T. Arima. 1998. "Review of Waste Glass Corrosion and Associated Radionuclide Release as a Part of Safety assessment of Entire Disposal System." *Progress in Nuclear Energy* 32:501-508.

Inagaki, Y, H., K. Idemitsu, T. Arima, T. Maeda, H. Ogawa and F. Itonaga. 2002. "Alteration-Phase Formation and associated Cesium Release during Alteration of R7T7 Waste Glass." *Material Research Society Symposium Proceedings*, v. 713, pp. JJ11.55.1 – JJ11.55.8, Material Research Society, Pittsburgh, Pennsylvania

Jantzen CM, DI Kaplan, NE Bibler, DK Peeler and MJ Plodinec. 2008. "Performance of a buried radioactive high level waste (HLW) glass after 24 years." *Journal of Nuclear Materials* 378:244-256.

Jegou C, S Gin, and F Larche. 2000. "Alteration kinetics of a simplified nuclear glass in an aqueous medium: effects of solution chemistry and of protective gel properties on diminishing the alteration rate." *Journal of Nuclear Materials* 280:216-229.

Jercinovic MJ, SA Kaser, RC Ewing, and W. Lutze. 1990. "Comparison of Surface Layers formed on Synthetic Basalt". *Material Research Society Symposium Proceedings*, v. 176, pp. 355-362, Material Research Society, Pittsburgh, Pennsylvania.

Jollivet P, F Angeli, C Cailleteau, F Devreux, P Frugier, and S Gin. 2008. "Investigation of gel porosity clogging during glass leaching." *Journal of Non-Crystalline Solids* 354:4952-4958.

Konijnendijk, WL and JM Stevels. (1977). "The Structure of Borosilicate Glasses Studied by Raman Scattering." *Journal of Non-Crystalline Solids*, 20(2): 193-224.

Ledieu A, F Devreux, and P Barboux. 2004a. "Monte Carlo simulations of borosilicate glass corrosion: predictions for morphology and kinetics." *J. Non-Cryst. Solids* 345&346:715-719.

Ledieu A, F Devreux, P Barboux, L Sicard, and O Spalla. 2004b. "Leaching of borosilicate glasses. I. Experiments." *J. Non-Cryst. Solids* 343:3-12.

Ledieu A, F Devreux, P Barboux, and Y Minet. 2006. "Contribution of Monte Carlo modeling to understanding the alteration of nuclear glasses by water." *Nucl. Sci. Eng*. 153:285-300.

Lenoir, M, A Grandjean, Y Linard, B Cochain, and DR Neuville. (2008). "The Influence of Si,B Substitution and of the Nature of Network-Modifying Cations on the Properties and Structure of Borosilicate Glasses and Melts." Chemical Geology, Vol. 256, pp. 316-325.

Leturcq G, G Berger, T Advocat, and E Vernaz. 1999. "Initial and long-term dissolution rates of aluminosilicate glasses enriched with Ti, Zr and Nd." *Chem. Geol.* 160:39-62.

Lobanova M, L Maurer, P Barboux, F Devreux, and Y Minet. 2001. "Monte Carlo modelling of glass dissolution: Comparison with experiments." *Mater. Res. Soc. Symp. Proc.* 663:237-245.

Lodding, A, EU Engstrom, BK Zoitos, DE Clark, and GG Wicks. 1992. Element Depth Profiling of Nuclear Waste Glasses after Two-Years Burial in a Salt Geology. *Journal of American Ceramic Society* 75:2702-2706.

Lutze, W, G Malow, H Rabe, and TJ Headley. 1983. "Surface Layer Formation on a Nuclear Waste Glass." *Material Research Society Symposium Proceedings*, v. 15, pp. 37-45, Material Research Society, Pittsburgh, Pennsylvania.

Manara, A, F Lanza, G Ceccone, G Della Mea, and G Salvagno. 1985. In *Scientific Basis for Nuclear Waste Management VIII: Material Research Society Symposium Proceedings*, pp. 85. Eds CM Jantzen, JA Stone, and RC Ewing. Material Research Society, Pittsburgh, Pennsylvania.

Mann FM, KC Burgard, WR Root, RJ Puigh, SH Finfrock, R Khaleel, DH Bacon, EJ Freeman, BP McGrail, SK Wurstner, and PE Lamont. 2001. *Hanford Immobilized Low-Activity Waste Performance Assessment: 2001 Version*. DOE/ORP-2000-24 Rev. 0, Department of Energy, Office of River Protection, Richland, Washington.

Mattigod S. V., R. D. Orr, R. J. Serne D. E. McCready, V. L. LeGore , J. S. Young and K. E. Parker. 2003. "Radionuclide Incorporation in Secondary Crystalline Minerals Resulting from Chemical Weathering of Selected Waste Glasses: Progress Report: Task kd.5b." PNNL-14319, Pacific Northwest National Laboratory, Richland, Washington.

Mattigod S.V., R.J. Serne, B.P. McGrail and V.L. LeGore. 2002. "Radionuclide Incorporation in Secondary Crystalline Minerals from Chemical Weathering of Waste Glasses." *Scientific Basis for Nuclear Waste Management XX*, B.P. McGrail and G. Cragliano (eds.), v. 713, pp. 597- 604, Material Research Society, Pittsburgh, Pennsylvania.

Mazer JJ, JK Bates, CM Stevenson, and CR Bradley. 1992. "Obsidians and Tektites: Natural Analogues for Water Diffusion in Nuclear Waste Glasses." *Materials Research Society Symposia Proceedings* 257:513-520.

McGrail BP, CW Lindenmeier, PF Martin, and GW Gee. 1996. "The Pressurized Unsaturated Flow (PUF) Test: A New Method for Engineered-Barrier Materials Evaluation." In: *Environmental Issues and Waste Management Technologies in the Ceramic and Nuclear Industries II*. V Jain, DK Peeler, Eds. *The American Ceramic Society*. Westerville, Ohio, 1996; Vol. 72, pp 317-329.

McGrail BP, WL Ebert, AJ Bakel and DK Peeler. 1997. "Measurement of kinetic rate law parameters on a Na-Ca-Al borosilicate glass for low-activity waste." *Journal of Nuclear Materials* 249(2-3):175-189.

McGrail BP, DH Bacon, WL Ebert and KP Saripalli. 1998. *A Strategy to Conduct an Analysis of the Long-Term Performance of Low-Activity Waste Glass in a Shallow Subsurface Disposal System at Hanford*. PNNL-11834, Pacific Northwest National Laboratory, Richland, Washington.

McGrail BP, PF Martin, CW Lindenmeier, and HT Schaef. 1999a. "Application of the Pressurized Unsaturated Flow (PUF) Test for Accelerated Ageing of Waste Forms." *In Ageing Studies and Lifetime Extension of Materials, Proceedings of the International Conference on Ageing Studies & Lifetime Extension of Materials*, ed. Leslie G Mallinson, pp. 313 – 320. Kluwer Academic/Plenum Publishers, Oxford, U.K.

McGrail BP, CW Lindenmeier, and PF Martin. 1999b. In: "Characterization of Pore Structure and Hydraulic Property Alteration in Pressurized Unsaturated Flow Tests." *Material Research Symposium Proceedings: Scientific Basis for Nuclear Waste Management*, Warrendale, Pennsylvania, 1999; DJ Wronkiewicz, JH Lee, Eds., *Material Research Society*: Warrendale, Pennsylvania, 1999; pp 421-428.

McGrail BP, PF Martin, HT Schaef, CW Lindenmeier, and AT Owen. 2000. "Glass/Ceramic Interactions in The Can-in-Canister Configuration for Disposal of Excess Weapons Plutonium." In: *Material Research Symposium Proceedings Scientific Basis for Nuclear Waste; Management XXIII*, 2000; RW Smith and DW Shoesmith, Eds. *Material Research Society,* pp 345-352.

McGrail BP, DH Bacon, JP Icenhower, FM Mann, RJ Puigh, HT Schaef, and SV Mattigod. 2001a. "Near-field performance assessment for a low-activity waste glass disposal system: laboratory testing to modeling results." *Journal of Nuclear Materials* 298:95-111.

McGrail BP, JP Icenhower, PF Martin, HT Schaef, MJ O'Hara, EA Rodriguez, and JL Steele. 2001b. *Waste Form Release Data Package for the 2001 Immobilized Low-Activity Waste Performance Assessment*. PNNL-13043, Rev. 2, Pacific Northwest National Laboratory, Richland, Washington.

McGrail BP, DH Bacon, RJ Serne, and EM Pierce. 2003. *A Strategy to Assess Performance of Selected Low-Activity Waste Forms in an Integrated Disposal Facility*. PNNL-14362, Pacific Northwest National Laboratory, Richland, Washington.

Murakami T, RC Ewing, and BC Bunker. 1985. "Analytical Electron Microscopy of Leached Layers on synthetic Basalt Glass." *Material Research Society Symposium Proceedings*, v. 112, pp. 737-747, Material Research Society, Pittsburgh, Pennsylvania.

Murakami T, T Banba, MJ Jercinovic, and RC Ewing. 1989. "Formation and Evolution of Alteration Layers on Borosilicate and Basalt Glasses: Initial Stage." *Material Research Society Symposium Proceedings*, v. 127, pp. 65- 72, Material Research Society, Pittsburgh, Pennsylvania.

Mysen, BO, LW Finger, D Virgo, and FA Seifert. (1982). "Curve-Fitting of Raman Spectra of Silicate Glasses." American Mineralogist, Vol. 67, pp. 686 – 695.

Nagy KL. 2001. "Dissolution and Precipitation Kinetics of Sheet Silicates." In: *Silicate Mineral Dissolution*. *Mineralogical Society of America* 173-233, Washington, D.C.

Nagy KL and AC Lasaga. 1993. "Letter: Simultaneous precipitation kinetics of kaolinite and gibbsite at 80°C and pH 3." *Geochimica et Cosmochimica Acta* 57:4329-4335.

Nichols WE and MD White. 2007a. *Project Management Plan for Subsurface Transport Over Multiple Phases (STOMP) Software Maintenance and Development*. PNNL-SA-54024, Pacific Northwest National Laboratory, Richland, Washington.

Nichols WE and MD White. 2007b. *Software Design Description For Subsurface Transport Over Multiple Phases (STOMP) Software*. PNNL-SA-54078, Pacific Northwest National Laboratory, Richland, Washington.

Oelkers EH. 2001. "General kinetic description of multioxide silicate mineral and glass dissolution. *Geochim.*" *Cosmochim. Acta* 65:3703-3719.

Oostrom M, DH Meck, and MD White. 2003. *STOMP. Subsurface Transport Over Multiple Phases. An Introductory Short Course*. PNNL-14440, Pacific Northwest National Laboratory, Richland, Washington.

Parkinson, BG, D Holland, ME Smith, C Larson, J Doerr, M Affatigato, SA Feller, AP Howes, and CR Scales. (2008). "Quantitative Measurement of Q^3 species in Silicate and Borosilicate Glasses Using Raman Spectroscopy." Journal of Non-Crystalline Solids, Vol. 354, No. 17, pp. 1936 - 1942.

Petit, JC, JC Dran, L Trotignon, JM Casabonne, A Paccagnella, and G. Della Mea. 1989. "Mechanisms of Heavy Element retention in Hydrated Layers formed on Leached Silicate Glasses." *Material Research Society Symposium Proceedings*, v. 127, pp. 33-40, Material Research Society, Pittsburgh, Pennsylvania.

Pierce EM, BP McGrail, EA Rodriguez, HT Schaef, KP Saripalli, RJ Serne, KM Krupka, PF Martin, SR Baum, KN Geiszler, LR Reed, and WJ Shaw. 2004a. *Waste Form Release Data Package for the 2005 Integrated Disposal Facility Performance Assessment*. PNNL-14805, Pacific Northwest National Laboratory, Richland, Washington.

Pierce EM, BP McGrail, EA Rodriguez, DM Wellman, LR Reed, DH Bacon, HT Schaef, and SR Baum. 2004b. *Laboratory Testing of Bulk Vitrified Low-Activity Waste Form to Support the 2005 Integrated Disposal Facility Performance Assessment*. PNNL-15126, Pacific Northwest National Laboratory, Richland, Washington.

Pierce EM, JP Icenhower, RJ Serne, and J Catalano. 2005. "Experimental determination of UO_2(cr) dissolution kinetics: Effects of solution saturation state and pH." *Journal of Nuclear Materials* 345:206-218.

Pierce EM, BP McGrail, J Marra, PF Martin, BW Arey, and KN Geiszler. 2007. "Accelerated Weathering of a High-Level and Pu-bearing Lanthanide Borosilicate Waste Glass in a Can-in-Canister Configuration." *Applied Geochemistry* 22:1841-1859.

Pierce EM, EL Richards, AM Davis, LR Reed and EA Rodriguez. 2008a. "Aluminoborosilicate waste glass dissolution under alkaline conditions at 40°C: Implications for a chemical affinity-based rate equation." *Environmental Chemistry* 5:1-13.

Pierce EM, EA Rodriguez, LJ Calligan, WJ Shaw, and BP McGrail. 2008b. "An experimental study of the dissolution rates of simulated aluminoborosilicate waste glasses as a function of pH and temperature under dilute conditions." *Applied Geochemistry* 23:2559-2573.

Pierce EM, LR Reed, WJ Shaw, BP McGrail, JP Icenhower, CF Windisch, EA Cordova, and J Broady. 2010. "Experimental determination of the effect of the ratio of B/Al on glass dissolution along the nepheline ($NaAlSiO_4$) - Malinkoite ($NaBSiO_4$) join." *Geochim. Cosmochim. Acta* 74:2634-2654.

Pierce, EM and DH Bacon. 2009. "Combined Experimental and Computational Approach to Predict the Glass-Water Reaction." *Nuclear Technology*,

Pierce, EM, BP McGrail, MM Valenta, and DM Strachan. 2006. "The Accelerated Weathering of a Radioactive Low-Activity Waste Glass Under Hydraulically Unsaturated Conditions: Experimental Results From a Pressurized Unsaturated Flow Test." *Nuclear Technology* **155**:149-165.

Puigh RJ. 1999. *Disposal Facility Data for the Hanford Immobilized Low-Activity Tank Waste*. HNF-4950, Rev. 0, Flour Federal Services, Richland, Washington.

Small JS, PN Humphrey, TL Johnstone, R Plant, MG Randall and DP Trivedi. 2000. "Results of an Aqueous Source Term Model for a Radiological Risk Assessment of the Drigg LLW Site, UK." In: *Scientific Basis for Nuclear Waste Management XXIII*, *Materials Research Society*, Boston, Massachusetts.

Takagi, I., T. Sasaki, K. Asahara, T. Kawasaki, T. Ishidera, and H. Moriyama. 2004. Simulated Waste glass Corrosion in Humic Acid Solution using Rutherford Backscattering Spectrometry. *Journal of Nuclear Science and Technology* 41:837-842.

Tan, J., S. Zhao, W. Wang, G. Davies, and X. Mo. (2004). "The Effect of Cooling Rate on the Structure of Sodium Silicate Glass." Material Science and Engineering B 106(3): 295 – 299.

Vienna, JD, PR Hrma, A Jiricka, DE Smith, TH Lorier, IA Reamer, and RL Schulz. 2001. *Hanford Immobilized LAW Product Acceptance Testing: Tanks Focus Area Results*. PNNL-13744, Pacific Northwest National Laboratory, Richland, WA.

Van Iseghem P, M Aetsens, K Lemmens, S Gin, D Deneele, B Grambow, BP McGrail, DM Strachan, G Wicks, and T McMenamin. 2004. "GLAMOR--A critical evaluation of the dissolution mechanisms of high-level waste glasses in conditions of relevance for geological disposal." In: *Euradwaste '04: Radioactive Waste Management : Community Policy and Research Initiatives : Proceedings of the Sixth European Commission Conference on the Management and Disposal of Radioactive Waste*. C Davies (ed). Luxembourg, March 29-31, 2004. Directorate-General for Research, European Commission, Luxembourg.

Vernaz E, S Gin, C Jegou, and I Ribet. 2001. "Present understanding of R7T7 glass alteration kinetics and their impact on long-term behavior modeling." *Journal of Nuclear Materials* 298:27-36.

Ward AL, MD White, EJ Freeman, and ZF Zhang. 2005. *STOMP Subsurface Transport Over Multiple Phases Version 1.0 Addendum: Sparse Vegetation Evapotranspiration Model for the Water-Air-Energy Operational Mode*. PNNL-15465, Pacific Northwest National Laboratory, Richland, Washington.

Werme LO, IK Bjorner, G Bart, HU Zwicky, B Grambow, W Lutze, RC Ewing and C Magrabi. 1990. "Chemical corrosion of highly radioactive borosilicate nuclear waste glass under simulated repository conditions." *Journal of Materials Research* 5(5):1130-1146.

White MD and M Oostrom. 2000. *STOMP: Subsurface Transport Over Multiple Phases Version 2.0 Theory Guide*. PNNL-12030 UC-2010, Pacific Northwest National Laboratory, Richland, Washington.

White MD and BP McGrail. 2005. *STOMP, Subsurface Transport Over Multiple Phases, Version 1.0, Addendum: ECKEChem, Equilibrium-Conservation-Kinetic Equation Chemistry and Reactive Transport*. PNNL-15482, Pacific Northwest National Laboratory, Richland, Washington.

White MD and M Oostrom. 2006. *STOMP: Subsurface Transport Over Multiple Phases, Version 4.0, User's Guide*. PNNL-15782, Pacific Northwest National Laboratory, Richland, Washington.

White MD and VL Freedman. 2007. *STOMP Software Configuration Management Plan*. PNNL-SA-54023, Pacific Northwest National Laboratory, Richland, Washington.

Wolery TJ and SA Daveler. 1992. *EQ6, A Computer Program for Reaction Path Modeling of Aqueous Geochemical Systems: Theoretical Manual, User's Guide and Related Documentation*. UCRL-MA-110662 PT IV, Lawrence Livermore National Laboratory, Livermore, California.

Wolery TW and RL Jarek. 2003. *Software User's Manual, EQ3/6, Version 8.0*. 10813-UM-8.0-00, Sandia National Laboratories, Albuquerque, New Mexico.

Wronkiewicz, D J, LM Wang, JK Bates, and BS Tani. 1993. "Effects of Radiation Exposure on Glass Alteration in a Steam Environment." *Material Research Society Symposium Proceedings*, v. 294, pp. 183-190, Material Research Society, Pittsburgh, Pennsylvania.

Xiao Y and AC Lasaga. 1994. "*Ab initio* quantum mechanical studies of the kinetics and mechanisms of silicate dissolution: H^+ (H_3O^+) catalysis." *Geochim. Cosmochim. Acta* 58:5379-5400.

Zhang ZF, VL Freedman, and MD White. 2007. *Requirements for STOMP Subsurface Transport Over Multiple Phases*. PNNL-SA-54079, Pacific Northwest National Laboratory, Richland, Washington.

Appendix A: Additional Raman Spectra

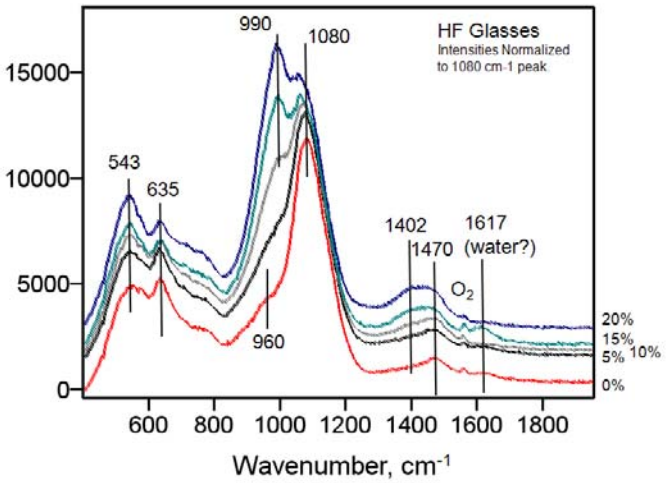

Figure A.1. Raman Spectra of unreacted Hf-series glasses

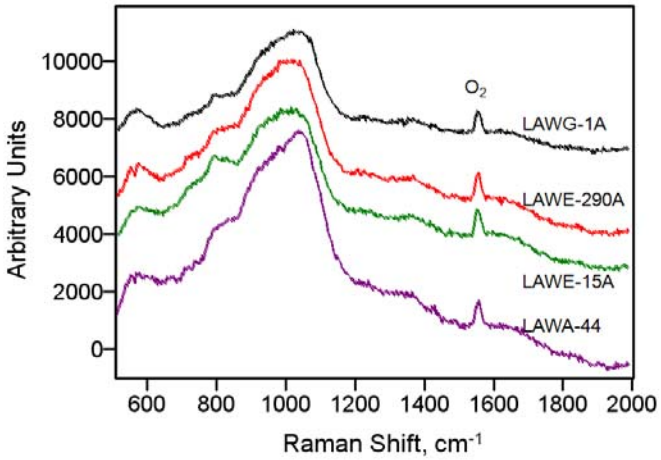

Figure A.2. Raman Spectra of unreacted ILAW glasses, LAWA44, LAWE-1A, LAWE-95A, and LAWE-290A.

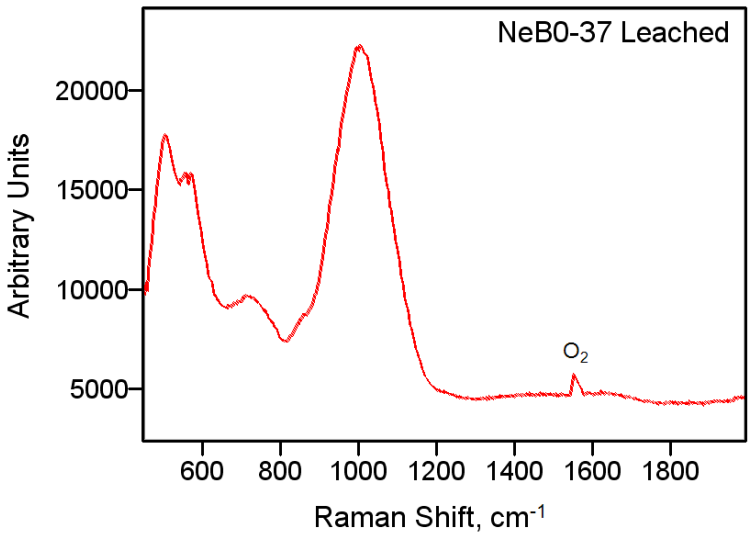

Figure A.3. Raman Spectra of reacted NeB0 glass.

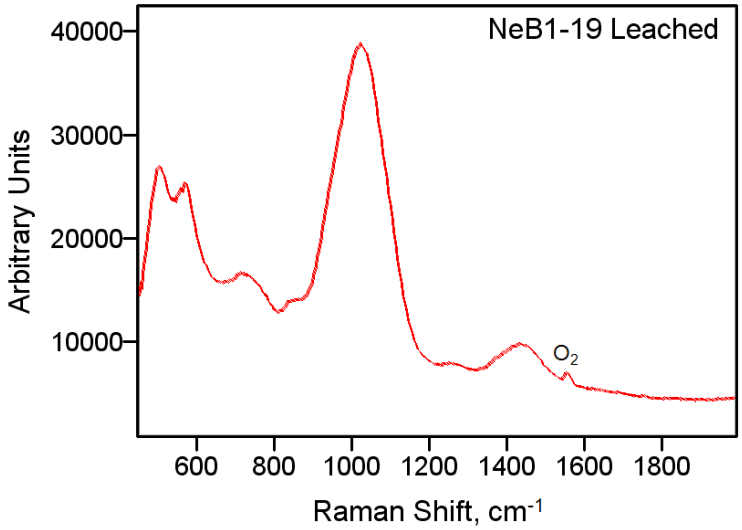

Figure A.4. Raman Spectra of reacted NeB1 glass.

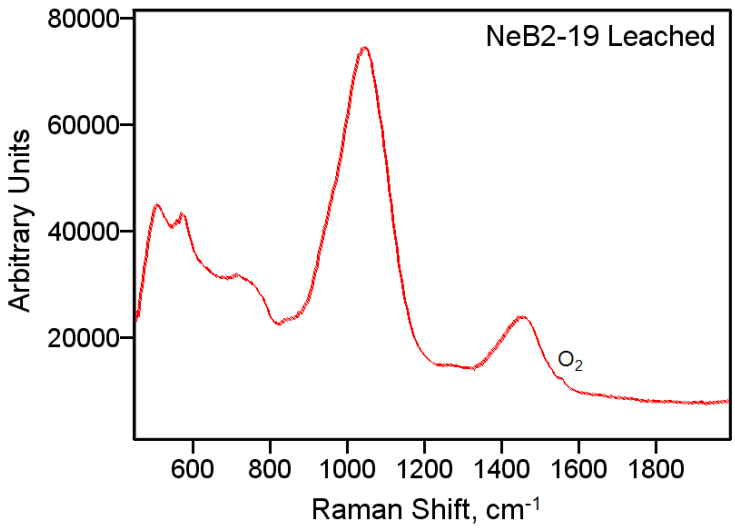

Figure A.5. Raman Spectra of reacted NeB2 glass.

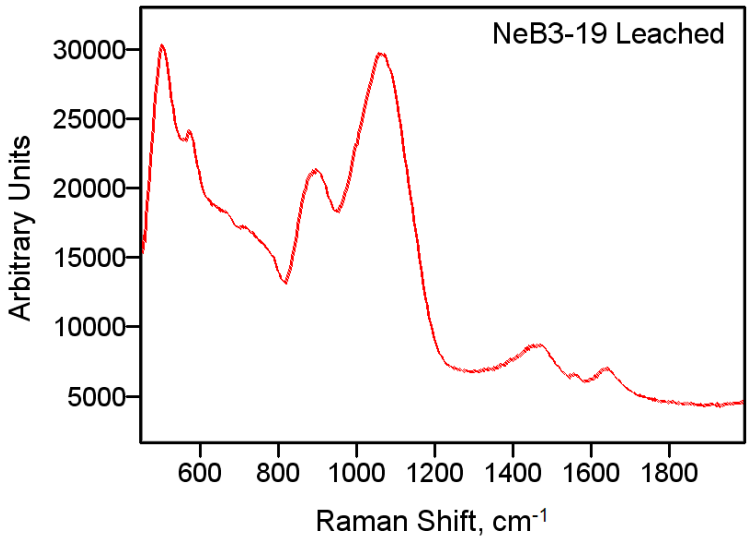

Figure A.6. Raman Spectra of reacted NeB3 glass.

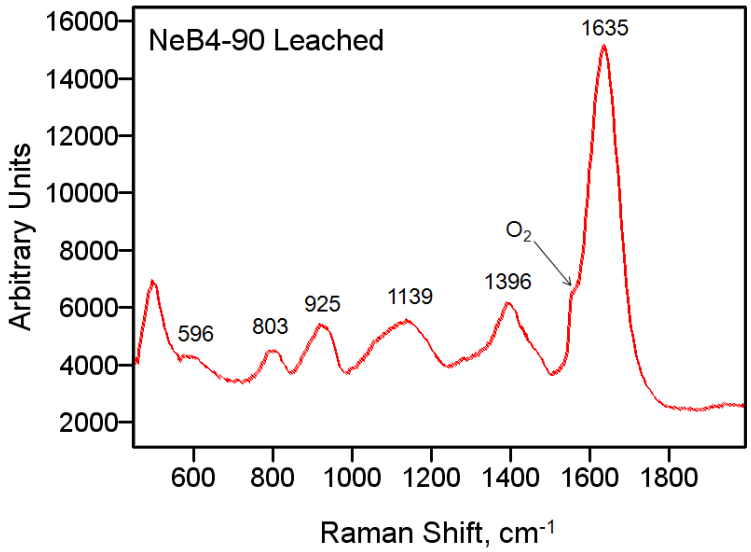

Figure A.7. Raman Spectra of reacted NeB4 glass.

Distribution

No of Copies

EXTERNAL

Kristin A. Colosi	B1-55
Thomas H. May	B1-55
Maxwell Melvin	B1-55
Terry Sams	B1-55
William G Ramsey	B1-55
Billie M. Mauss	H6-60

No. of Copies

INTERNAL

10 Pacific Northwest National Laboratory

E. M. Pierce (2)	K3-62
D. H. Bacon	K9-33
CF Windisch	K2-01
SD Burton	K8-98
S.V. Mattigod	K3-62
RJ Serne	K6-81
J Westsik	K7-15
KJ Cantrell	K6-81
MM Valenta	K6-81

Pacific Northwest
NATIONAL LABORATORY

U.S. DEPARTMENT OF
ENERGY

902 Battelle Boulevard
P.O. Box 999
Richland, WA 99352
1-888-375-PNNL (7665)
www.pnl.gov